Summer 6-22-2010

Ultrasound Transient Shear Wave Elasticity Imaging for Tendon Tissue

Pengfei Song
University of Nebraska at Lincoln, psong@huskers.unl.edu

ULTRASOUND TRANSIENT SHEAR WAVE ELASTICITY IMAGING FOR TENDON TISSUE

by

Pengfei Song

A THESIS

Presented to the Faculty of
The Graduate College at the University of Nebraska
In Partial Fulfillment of Requirements
For the Degree of Master of Science

Major: Agricultural and Biological Systems Engineering

Under the Supervision of Professor Gregory R. Bashford

Lincoln, Nebraska
June, 2010

ULTRASOUND TRANSIENT SHEAR WAVE ELASTICITY IMAGING FOR TENDON TISSUE

Pengfei Song, M.S.

University of Nebraska, 2010

Advisor: Gregory R. Bashford

Degeneration of tendon tissue is a common cause of tendon dysfunction with the symptoms of repeated episodes of pain and palpable increase of tendon thickness. Tendon mechanical properties are directly related to its physiological composition and the structural organization of the interior collagen fibers which could be altered by tendon degeneration due to overuse or injury. Thus, measuring mechanical properties of tendon tissue may represent a quantitative measurement of pain, reduced function, and tissue health. Ultrasound elasticity imaging has been developed in the last two decades and has proved to be a promising tool for tissue elasticity imaging. To date, however, well established protocols of tendinopathy elasticity imaging for diagnosing tendon degeneration in early stages or late stages do not exist. This thesis describes the re-creation of one dynamic ultrasound elasticity imaging method and the development of an ultrasound transient shear wave elasticity imaging platform for tendon and other musculoskeletal tissue imaging. An experimental mechanical stage with proper supporting systems and accurate translating stages was designed and made. A variety of high-quality tissue-mimicking phantoms were made to simulate homogeneous and heterogeneous soft tissues as well as tendon tissues. A series of data acquisition and data processing programs

were developed to collect the displacement data from the phantom and calculate the shear modulus and Young's modulus of the target. The imaging platform was found to be capable of conducting comparative measurements of the elastic parameters of the phantoms and quantitatively mapping elasticity onto ultrasound B-Mode images. This suggests the system has great potential for not only benefiting individuals with tendinopathy with an earlier detection, intervention and better rehabilitation, but also for providing a medical tool for quantification of musculoskeletal tissue dysfunction in other regions of the body such as the shoulder, elbow and knee.

ACKNOWLEDGMENTS

I would like to thank my family for their consistent support to my two years' study and life in the United States. I would like to thank Scott Minchow for his help in designing and machining the custom experiment equipments and setups; Drs. Jeyamkondan Subbiah, Yixiang Xu and Curtis Weller for their phantom making and food elasticity expertise; Krishnamoorthy Pitchai and Robert Weber for their help in measuring the material elasticity using the texture analysis machine and the Instron machine; Dr. Shigao Chen for his instructions of phantom making and general questions on ultrasound elastography; Dr. Dennis Burson for his help in getting fresh bovine tendons; Dr. Eileen Hebets and Jason Stafstrom for their guide in using their laser vibrometer; Dr. Kornelia Kulig for her expertise on pathology of tendinopathy; Bonita Delhay for her help in experiment supplies; and Drs. Michael Hoffman and Shadi Othman for serving on my graduate committee. Most importantly, I would like to thank my adviser, Dr. Greg Bashford, for his guidance and encouragement to complete this project, and for his warmhearted care which makes Nebraska the feeling of home.

TABLE OF CONTENTS

- **Abstract** ii
- **Acknowledgments** iv
- **Table of Contents** v
- **List of Figures and Tables** vii
- **Chapter 1: Introduction** 1
  - Clinical Relevance 1
  - Long Term Goal 3
  - Objectives 3
- **Chapter 2: Theory** 5
  - Literature Review 5
  - Wave Propagation Theories 7
  - Green's Function 11
  - Diffraction Effects 12
  - Spline-based Displacement Estimation Algorithm 15
- **Chapter 3: Feasibility Experiments** 18
  - Introduction 18
  - Materials 18
    - Tissue-mimicking Phantoms 18
    - Mechanical Platform 21
    - LabVIEW Program 23
  - Methods 24
    - Green's Function Simulation 24
    - Acoustic Properties Measurement 28
    - Phantom Elasticity Measurement 32
    - Grape-olive Phantom 41
    - Bi-layer Phantom 42
  - Results and Discussion 44

- Green's Function Simulation 44
- Acoustic Properties Measurement 45
- Phantom Elasticity Measurement 47
- Grape-olive Phantom 53
- Bi-layer Phantom 58

❖ **Chapter 4: Bovine Tendon Experiments** 60

- Introduction 60
- Theory 60
- Methods 61
- Results and Discussion 65

❖ **Chapter 5: Summary and Suggested Future Work** 70

- Summary 70
- Suggested Future Work 71

❖ **References** 73

❖ **Appendices** 77

LIST OF FIGURES AND TABLES

❖ Figures

- Figure 1. Behavior of Elements of the Medium During Wave Propagation. 8
- Figure 2. Isoamplitude and Gray Level Image of the Displacement Amplitudes. 12
- Figure 3. Shear-wave Velocity and Vibration Frequency. 14
- Figure 4. Shear-wave Velocity and the Size of Vibrator. 15
- Figure 5. Amplitude Curves of Two Consecutive A-lines with Displacement 16
- Figure 6. Mechanical Stage..... 22
- Figure 7. Specially Designed Acrylic Plastic Plate..... 22
- Figure 8. LabVIEW Program Front Panel. 23
- Figure 9. 3D Mesh Plot of the Displacement Field. 25
- Figure 10. Seismic Plot of the Displacement Field..... 25
- Figure 11. Phase Plot from the Hilbert Transform of Each Depth Layer..... 27
- Figure 12. Experiment Set-up for Acoustic Properties Measurement. 28
- Figure 13. The Signal of Acoustic Properties Measurement. 30
- Figure 14. Experiment Set-up for Instron 5566 Elasticity Test. 33
- Figure 15. Experiment Set-up for the Imaging System. 35
- Figure 16. The Phantom and Set-ups for the Vibrator and Transducer. 35
- Figure 17. The Flowchart of Data Processing..... 38
- Figure 18. Seismic Plot of the Displacement Field..... 40
- Figure 19. Grape-olive Phantom..... 42

- Figure 20. Bi-layer Phantom. 43
- Figure 21. Phase-depth Plot at the Selected Time Point. 45
- Figure 22. Stress over Strain Curves from Instron Machine. 48
- Figure 23. Quasi-linear Part of the Stress over Strain Curve. 48
- Figure 24. Procedures of Measuring Phantom Elasticity Using Ultrasound. 51
- Figure 25. Grape Test in Grape-olive Phantom.. 55
- Figure 26. Hollow Olive Test in Grape-olive Phantom. 56
- Figure 27. Stuffed Olive Test in Grape-olive Phantom. 57
- Figure 28. Bi-layer Phantom Test. 59
- Figure 29. Bovine Achilles Tendon Preparation and Bovine Phantom Making. .. 62
- Figure 30. Ultrasound B-mode Images of Bovine Tendon and Human Tendon... 63
- Figure 31. Create 2D Elasticity Image. 64
- Figure 32. Phase versus Depth Plot of the Bovine Tendon Phantom. 66
- Figure 33. Shear-modulus Mapping Image by 2-point Linear Fitting 68
- Figure 34. Shear-modulus Mapping Image by 10-point Linear Fitting. 69

❖ **Tables**

- Table 1. Phantom Thickness Measurements..…….....51
- Table 2. Elasticity Measurements Using Instron Test and Ultrasound Test……54

CHAPTER 1: INTRODUCTION

Clinical Relevance

Degeneration of tendon tissue is a common cause of tendon dysfunction with symptoms of repeated episodes of pain and palpable increase of tendon thickness (Kulig and Bashford, personal communication, 2009). Achilles tendinopathy has been reported as one of the most common tendon tissue pathologies and affects millions of people in the U.S. today, including 60 million overweight individuals with a 5.9% lifetime cumulative incidence and 30 – 50% of athletes with tendon overuse injuries (Scott and Ashe, 2006; CDC website; Kulig and Bashford, personal communication, 2009). Clinically, tendinopathy in early stages is asymptomatic and is usually undiagnosed until significant tendon pain and loss of function appears, which can lead to severe tendon tissue impairment and even disability (Kulig and Bashford, personal communication, 2009). However, if early diagnosis and rehabilitative interventions were achievable, better treatment of tendinopathy could be accomplished with less disability, suffering, and expense (Kulig and Bashford, personal communication, 2009).

Currently, traditional medical imaging modalities such as magnetic resonance imaging (MRI) and ultrasound are widely used as non-invasive diagnosing tools for tendinopathy. While MRI has the capability of prognosing tendon rupture with evidence of tendinopathy in early stages (McQueen et al., 1995), the expense of MRI tends to keep physicians and patients from utilization until advanced symptoms show up. On the other hand, because of the low expenses compared to MRI, ultrasound imaging provides easier access to

physicians and patients and is more commonly used for tendinopathy diagnosis. However, only late stages of tendon pathology can be disclosed by ultrasound, because the resolution of ultrasound does not permit examining the tissue at a microscopic level and tendinopathy in the early stages is asymptomatic at the level of resolution of ultrasound (Kulig and Bashford, personal communication, 2009). Additionally, the degree of pathology is not yet measurable by ultrasound, and to our knowledge no protocols of diagnosing tendon degeneration at an early stage (predisposed to tendon rupture) have been established yet (Kulig and Bashford, personal communication, 2009).

Tendon mechanical properties may be altered by tendinopathy in early stages, which might be measured and detected by use of non-invasive elasticity imaging modalities. It has been shown that the mechanical properties of tendons are directly related to their physiological composition and the structural organization of the interior collagen fibers (Latash and Zatsiorsky, 1993; Silver et al., 2003). During tendinopathy, the mechanical strength of tendon tissue is compromised because of the breakdown of type I collagen and its cross-linkages accompanied by the proliferation of type III collagen (Kulig and Bashford, personal communication, 2009). Although numerous ultrasound elasticity imaging techniques have been developed during the last two decades (Greenleaf et al., 2003), to date there are not well established protocols of tendinopathy elasticity imaging for diagnosing tendon degeneration in early stages or late stages (Kulig and Bashford, personal communication, 2009). Therefore, developing such a clinically useful elasticity imaging platform could not only benefit tendinopathic individuals with an earlier detection,

intervention and better rehabilitation, but also provide a potential medical tool for quantifying musculoskeletal tissue dysfunction in other regions of the body such as the shoulder, elbow and knee (Kulig and Bashford, personal communication, 2009).

Long Term Goal

The long term goal of this research is to create an ultrasound elasticity imaging system which can quantitatively measure the Young's modulus of musculoskeletal tissues such as tendon, and accurately discriminate tissue degeneration areas (e.g., tendinopathy areas) from normal areas in early stages. The ultrasound transient shear wave elasticity imaging methodology will be adopted and re-created in this system, with a 1D ultrasound elasticity probe designed by mounting a small single element transducer onto a vibrator. This system will have the ability to collect *in vivo* shear wave displacement data from human musculoskeletal tissues and create a 2D elasticity map of the Regions of Interest (ROIs) through post data processing. The elasticity map will contain the local Young's modulus information of each kernel within the ROI and accurately depict degenerated tissue area by assigning Young's modulus to graduated color values. This system will be used to help physicians better diagnose musculoskeletal tissue degeneration in early stages and track tendon recovery status during rehabilitation training.

Objectives

While the long term goal is introduced above, steps are currently being made to overcome many practical hurdles towards *in vivo* measurement of the tendon tissue Young's modulus. The major hurdles include determining the proper experimental set-ups

for tissue elasticity imaging, designing data processing algorithms to accurately measure the shear-wave speed, and designing methods for quantitative elasticity mapping. The objectives of this thesis are to remove these hurdles and test the feasibility of using ultrasound transient shear wave elasticity imaging on quantitative measurement of the musculoskeletal tissue stiffness. The objectives include:

- Re-create an ultrasound transient shear wave elasticity imaging platform for tendon tissue elasticity imaging.
- Use simulation to provide a verification displacement field, and verify the proposed shear-wave velocity measurement method.
- Test the elasticity imaging platform with real materials (phantoms).
- Test the proposed measurement technique on bovine tendon tissue.

CHAPTER 2: THEORY

Literature Review

The main organization of interior tendon structure is in the form of parallel aligned collagen fibers along the direction of tensile force (Telford and Bridgman, 1995). This unique tissue organization can be disturbed by an excessive magnitude of loading and lead to the development of tendinopathy (Bleakney et al., 2002). The disorganization of collagen bundles within tendon tissue can be visualized in ultrasound B-Mode images by presenting the characteristics of lack of parallel striations and localized regions of hypoechogenicity (Bashford et al., 2008).

Quantification of the structural organization of Achilles tendon through ultrasound imaging and pattern recognition methods was demonstrated to be an exceptional tool for diagnosing tendinopathy (Bashford et al., 2008; Song et al., 2009). However, this method is largely dependent on the size and structure of the training database and the appearance of obvious tendinopathic characteristics in the image. A dynamic ultrasound-image sequence processing technique proved to be more sensitive than a static image processing method (Ofer et al., 2004). However, a detailed model for explaining the tendon motion properties such as viscoelasticity needs to be developed. Neither of these two methods led to measurement of intrinsic tissue properties related to collagen disorganization, which may lead to recognition of pathologic tendon degenerations.

Ultrasound elastography is increasingly being used to characterize *in vivo* musculoskeletal mechanics. The term “elastography” was created by Ophir who first used

external compression methods to create strain images under static conditions (Ophir et al., 1991; Greenleaf et al., 2003). For musculoskeletal mechanics measurement, a common approach is to track the relative motion between ultrasound B-Mode images with the muscle in relaxed and contracted states, and then estimate elastic parameters such as average strain in the tendon and muscle by use of various speckle tracking algorithms (Farron et al., 2000; Maganaris and Paul, 2000a; Maganaris, 2002; Maganaris and Paul, 2000b; Kurokawa et al., 2003). Tissue stress and stiffness can also be estimated by correlating measured strain with applied muscle contraction (Ito et al., 1998; Levinson et al., 1995). While estimating the overall elastic parameters of tissue mechanics, the static ultrasound elastography method cannot measure localized elasticity values *in vivo*. Additionally, an external or internal force has to be applied onto the tissue in order to gain deformation information, which can be painful and risky for patients with tendinopathy in an advanced stage.

Dynamic ultrasound elastography methods commonly steer externally-generated mechanical waves through the target area so that elastic parameters of the tissue can be estimated by correlating wave equations with tissue viscoelasticity (Greenleaf et al., 2003). A representative of the dynamic method was created by Catheline et al. in 1999a, where the displacement field inside a semi-infinite and homogenous phantom excited by low frequency vibrations was studied. The resulting technique was termed as “transient elastography” (Catheline et al., 1999a). This methodology was shown to be a promising tool for creating quantitative viscoelasticity maps of human soft tissues *in vivo* (Muller et

al., 2009; Bercoff et al., 2004). By introducing shear waves into tissue medium, this method can conveniently convert measured local shear-wave speed into local shear modulus of the tissue. To date, however, this method has not been used on tendinopathy or other musculoskeletal tissue pathology diagnosis yet. Therefore in this project, we introduce an ultrasound transient elastography technique for tendon tissue elasticity measurement. In the future, we expect to develop the technique into a clinically useful tool for diagnosis of tendinopathy and other degeneration of musculoskeletal tissues.

Wave Propagation Theories

Compression and shear waves are generated when a pulse is applied on a semi-infinite, isotropic and homogeneous solid (Gennisson et al., 2003). "Elastography is based largely on the shear stiffness of tissues and the relatively large variations in shear stiffness with disease. This means that in elastographic applications, we must deal with the fact that tissue particle displacements (and velocities) have two parts: one associated with a simple rotation without change in volume and the other that involves compression of the tissues but is irrotational" (Carstensen et al., 2008).

Plane, longitudinal, compressional wave (Changing elementary volume and density)

Plane, transverse, shear wave (Constant elementary volume and density)

Figure 1. Re-created from Carstensen et al., 2008. "Behavior of elements of the medium during propagation of idealized, plane, infinite, longitudinal, compressional and transverse shear waves" (Carstensen et al., 2008).

As shown in the right part of Fig. 1 (Carstensen et al., 2008), under transverse excitation, the outer layer is displaced tangentially, dragging along a layer of tissue below it. Since it is the shear modulus that is involved in the propagation process, this wave is called a shear wave and has a speed of (Graff, 1975)

$$C_s = \sqrt{\frac{\mu}{\rho}}, \qquad (1)$$

where ρ (kg/m^3) is the density of the medium and μ (Pa) is the shear stiffness. In this thesis, we assume that viscosity does not significantly affect the shear-wave speed, thus we neglect it in the shear-wave speed calculation. During this process, the elementary cube is sheared and rotated parallel to the surface of the medium without changes of volume.

As shown in the left part of Fig. 1 (Carstensen et al., 2008), under a uniform, normal harmonic stress to the surface of a medium, the elementary cube is flattened and stretched along the direction of wave propagation as the disturbance passes it. Because the volume of the elementary cube changes during the process, the bulk stiffness is involved. The

generated wave is called a compressional wave and it propagates into the medium at a speed of (Graff, 1975)

$$C_p = \sqrt{\frac{k+\frac{4}{3}\mu}{\rho}}, \qquad (2)$$

where *k* (Pa) is the bulk stiffness of the medium. "The change in shape of the cube explains the involvement of the shear modulus in the propagation of the compressional disturbance" (Carstensen et al., 2008).

Carstensen et al. also clarified the terminology for compressional waves and shear waves because of confusion in the literature (Carstensen et al., 2008). According to Carstensen's definition (Carstensen et al., 2008), "the wave whose velocity depends only on the shear stiffness of the medium is primarily one in which the volume of the element of the medium does not change – the divergence of the displacement is zero. It could be both transverse and longitudinal. And we shall refer here to waves of the first kind ([*Eqn. (1)*]), which are controlled by the shear stiffness of the medium only, as shear waves. The velocity of the second kind of wave ([*Eqn. (2)*]) depends on both shear and bulk stiffness. It is usually longitudinal, but shear waves can also be longitudinal. It involves compression but it also involves shear strain. And we shall call these waves, whose speed of propagation involves the bulk stiffness, compressional waves" (Carstensen et al., 2008).

Typical wave speeds in soft tissues are, respectively, C_P = 1500 ms^{-1} and Cs = 5 ms^{-1}. The common parameter used to describe soft tissues elasticity is Young's modulus *E* (Gennisson et al., 2003),

$$E = \frac{\mu(3\lambda+2\mu)}{\lambda+\mu}, \quad (3)$$

where λ is the Lamé coefficient. In soft media λ is 10^6 times bigger than μ, thus a good approximation of *E* is (Gennisson et al., 2003)

$$E \cong 3\mu. \quad (4)$$

Finally, the Young's modulus as a function of the shear-wave speed is given as

$$E = 3\rho C_s^2. \quad (5)$$

Emphasizing the contrast between compressional and shear-wave speeds in soft tissue, Carstensen notes: "When a semi-infinite, isotropic and homogeneous medium is excited by a single cycle or pulse, the compressional wave (fast wave) and the shear wave (slow wave) are almost instantly separated in space. Because the displacement field associated with the compressional wave has essentially uniform phase throughout the field-of-view, only the shear wave is of interest of quantitative stiffness measurements" (Carstensen et al., 2008). Oestreicher's analytical solution (Oestreicher, 1951) for the displacement field includes contributions to the particle displacement from both compressional and shear waves, and it indicates that the shear wave along the axis of oscillation is entirely longitudinal (Oestreicher, 1951). However, it is the shear modulus of the medium that controls the shear-wave velocity (C_S) no matter the wave propagation is longitudinal or transverse (Carstensen et al., 2008). As long as the shear wave could be generated and its propagation speed could be measured, the shear modulus could be accurately estimated by use of Eqn. (1) (Carstensen et al., 2008).

Green's Function

A Green's function for a transient excitation of a point force applied on a semi-infinite solid with free boundary conditions has been calculated by Gakenheimer and Miklowitz (Gakenheimer and Miklowitz, 1969). Appendix A presents the derivation of an approximate expression for the Green's function by Catheline et al. (Catheline et al., 1999b). Meanwhile, Catheline et al. confirmed the displacement field generated by a point source in an agar-gelatin phantom with the prediction by the Green's function (Catheline et al., 1999b). The polarity of the piston point source indicates that a piston point source is a monopolar source for the compressional wave and a dipolar source for the shear wave (Scruby and Drain, 1990). Thus, for the compressional wave, almost the same energy is sent in all directions; while for the shear wave, the point source is not omnidirectional but presents a lobe along the diagonal of the phantom (Catheline et al., 1999a), as shown in Fig. 2 (Catheline et al., 1999a).

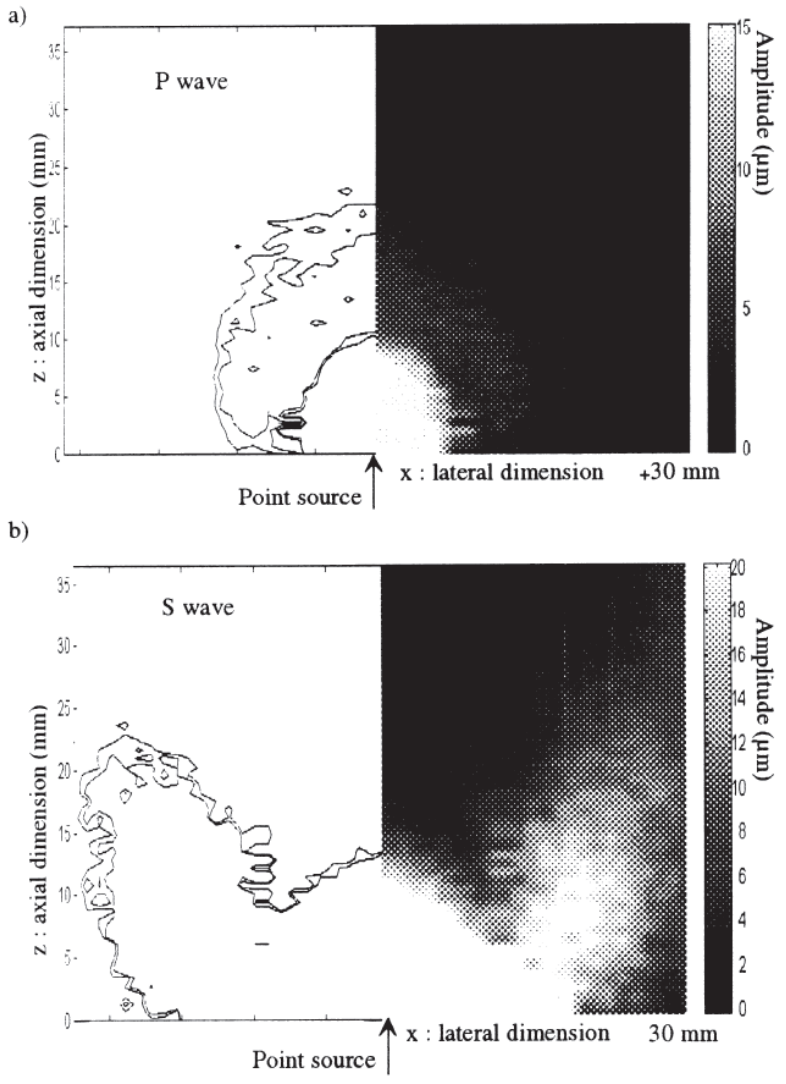

Figure 2. Reprinted from Catheline et al., 1999a. "Isoamplitude ([*top*]) and gray level image ([*bottom*]) of the displacement amplitudes of a compressional and shear wave generated by a point source in an agar-gelatin phantom" (Catheline et al., 1999a).

Diffraction Effects

Diffraction effects in transient elastography are caused by a vibrator piston with non-negligible dimension (diameter). "Usually, the size of the vibrator pistons generating shear waves from the surface ranges from 1 to 3 cm. For a shear wave with velocity of 3m/s, the shear wave length is 150 mm at 20 Hz and 10 mm at 300 Hz. Thus, the size of the piston

is not negligible compared to the wavelength and the Fresnel zone (near field) can lie at a depth of 50 cm. Consequently, the diffraction effects should be taken into account in formulation of shear-wave velocity" (Catheline et al., 1999b).

Based on diffraction effects, Sandrin et al. found that if there are displacements induced by the shear wave on the axis vibrator-transducer, they must be purely longitudinal, although the shear waves are strictly transverse in the far field (Sandrin et al., 2002). This discovery is well consistent with the theory proposed by Carstensen mentioned above (Carstensen et al., 2008), and it provides the foundation of ultrasound transient elastography.

Also based on diffraction effects, Catheline et al. revised the classical theory of the shear-wave speed (Catheline et al., 1999b) in the viscoelastic medium (also called Voigt's body) introduced by Pollard in 1977 (Pollard, 1977):

$$C_s = \sqrt{\frac{2\left(\mu_1^2+\omega^2\mu_2^2\right)}{\rho\left(\mu_1+\sqrt{\left(\mu_1^2+\omega^2\mu_2^2\right)}\right)}}, \tag{6}$$

where ω (rad/s) is the center angular frequency, μ_1, μ_2 are the Lamé coefficients. When taking diffraction effects into account, Catheline et al. proposed a revised version of the shear-wave velocity equation in a Voigt's body equation as (Catheline et al., 1999b):

$$C^*(\omega) = \frac{\omega}{Re\left\{k+\frac{\partial}{\partial z}\left(atan\left[\frac{sin\left(kz\left(\sqrt{1+\frac{a^2}{z^2}}-1\right)\right)}{cos\left(kz\left(\sqrt{1+\frac{a^2}{z^2}}-1\right)\right)-\sqrt{1+\frac{a^2}{z^2}}}\right]\right)\right\}}, \tag{7}$$

where k is defined in Voigt's body (Oestrecher, 1951) as $k = \sqrt{\frac{\rho\omega^2}{\mu_1+i\omega\mu_2}}$, z (mm) is the depth, a (mm) is the aperture size (vibrator piston diameter). Fig. 3 (Catheline et al., 1999b)

shows the relationship between shear wave frequency and shear-wave speed with diffraction effects. Fig. 4 (Catheline et al., 1999b) shows the relationship between shear-wave velocity and the aperture size.

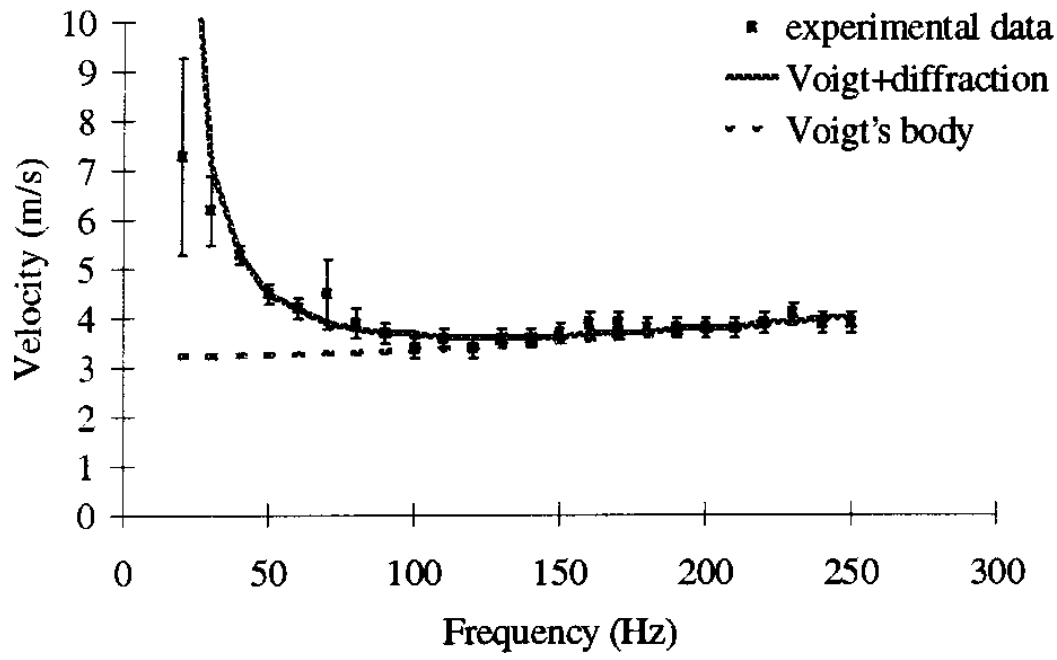

Figure 3. Reprinted from Catheline et al., 1999b. "Velocity of the low-frequency shear wave in an agar-gelatin phantom. Experimental data compared to velocity in a Voigt's body, [*Eqn. (6)*], and to velocity in a Voigt's body modified by diffraction, [*Eqn. (7)*]" (Catheline et al., 1999b).

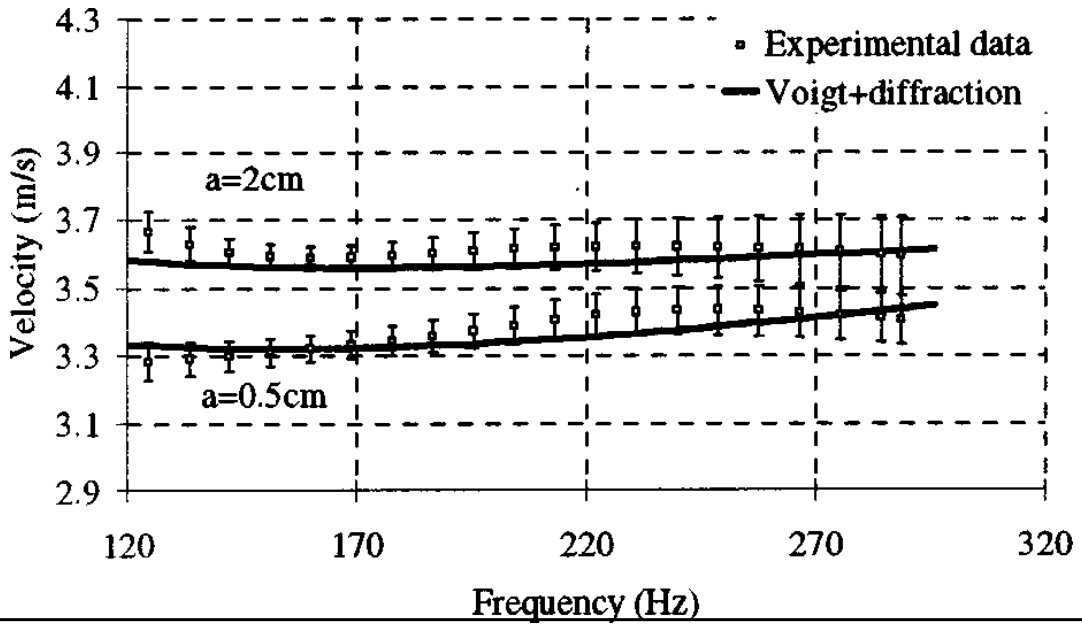

Figure 4. Reprinted from Catheline et al., 1999b. "The apparent shear-wave velocity is modifed by the size of the vibrator. Experimental and theoretical values ([*Eqn. (7)*]) are compared for a radius of 0.5 cm and 2 cm" (Catheline et al., 1999b).

Figs. 3 and 4 indicate that when frequency decreases or vibrator aperture size increases, the measured shear-wave velocity will increase because of the diffraction effects (Catheline et al., 1999b). This phenomenon could induce significant measurement biases as shown in later chapters.

Spline-based Displacement Estimation Algorithm

"When a motionless biological medium is illuminated by ultrasonic pulses, the acoustic speckle from the same zone of soft tissues remains the same as long as the scatterers do not move. When low frequency vibrations propagate inside the medium, they induce a low frequency motion of the scatterers that can be detected and measured by correlating successive A-scans" (Catheline et al., 1999b). For example, Fig. 5 shows the

A-scan amplitude curve from two consecutive lines while low frequency vibrations were generated by a vibrator (Brüel & Kjær, type 4810) with a piston vibrator (7mm in radius). The axial displacement could be calculated by performing cross-correlation between the two consecutive A-line signals and calculating the correlation coefficients (r) (Bohs and Trahey, 1991):

$$r = \frac{\sum_i \sum_j (A_i - \bar{A})(B_j - \bar{B})}{\sqrt{\sum_i (A_i - \bar{A})^2 \sum_j (B_j - \bar{B})^2}}, \quad (8)$$

where A and B are the target signal and the reference signal respectively, the position of the maximum of r is considered the best match and the "Lag" as shown in Fig. 5 could be then obtained.

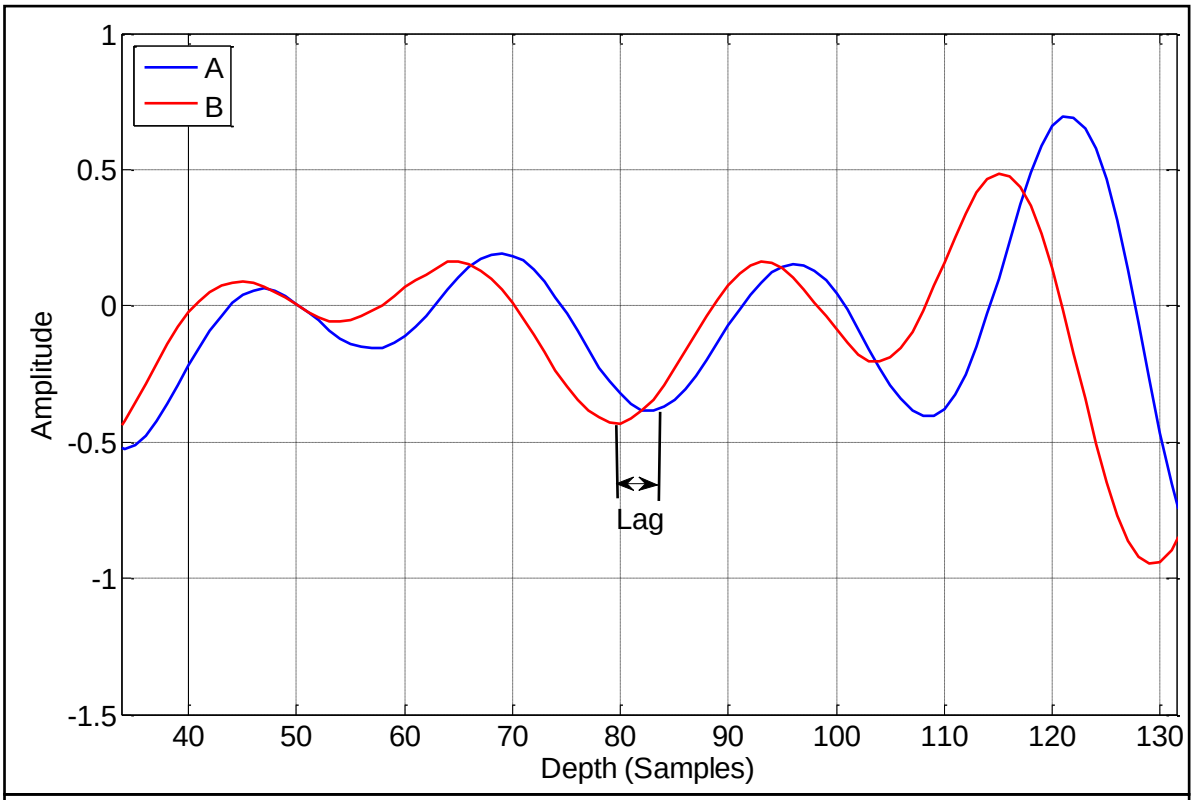

Figure 5. Amplitude curves of two consecutive A-lines collected with low frequency vibrations generated by a mini-shaker. The displacement (lag) between two lines can be estimated by cross correlation method.

The ultrasound signal digitizer used in this thesis has a stable sampling frequency of 100 MHz. Given the sound speed of 1540 m/s, each sample of the echo signal represents about 7.7 μm axial distance, which means that the minimum axial displacement that can be detected is approximately 7.7 μm. However, the displacement excited by the shear wave ranges from 0.1 to 6 μm. So the current sampling interval cannot accurately estimate the displacement and will result in estimator bias and variance.

Viola and Walker proposed a sub-sampling algorithm based on spline interpolation for continuous time-delay estimation in 2005 (Viola and Walker, 2005). By interpolation, the sampling interval could be significantly decreased so that tiny displacements around 0.1 μm can also be detected. The sum squared differences (SSD) algorithm was used and was shown to be less computationally expensive than cross correlation algorithm while achieving higher performance in terms of jitter and bias over a broad range of conditions (Viola and Walker, 2005). The detailed spline-based algorithm is presented in Appendix B.

CHAPTER 3: FEASIBILITY EXPERIMENTS

Introduction

Before implementing the transient elastography technique onto tendons for elasticity imaging, a series of feasibility experiments were conducted to verify the capability of the technique using theories and methods introduced by Catheline et al. (Catheline et al., 1999b). Both the simulation and practical experiments were re-created according to the literature. Also, an Instron machine was used to obtain verification data of the phantom elasticity. In order to test the feasibility of the proposed technique on heterogeneous materials like tendon, a grape-olive phantom and a bi-layer phantom were made and tested. The following sections detail how practical experimental problems were resolved and discuss the measurement results.

Materials

Tissue-mimicking Phantoms

Tissue-mimicking phantoms are commonly used in medical ultrasound related research. The phantoms should have a comparable attenuation coefficient and speed of sound propagation as soft tissues (Madsen et al., 1998). The ultrasound attenuation coefficient, if measured in dB, is nearly proportional to the ultrasound frequency, and the ultrasonic speed on average is 1540 m/s (Madsen et al., 1998). The recommended attenuation coefficient use in phantom materials range from 0.3 – 0.7 dB cm^{-1} MHz^{-1} (AIUM Technical Standards Committee 1990; American Institute of Ultrasound in Medicine 1992). Typically, solid phantoms made by gelatin powder and water, which have

been used for many years by ultrasound researchers, provide both the desirable attenuation coefficient and sound speed. Thus, we chose a gelatin phantom in this project.

Scatterers need to be added into the gelatin phantom to provide the recommended backscatter coefficient which would mimic the internal structure of soft tissues and generate speckle patterns in ultrasound images. A variety of ultrasound phantoms with different scattering materials have been introduced and used in ultrasound research for different purposes. Some examples of materials used include, agar with suspended graphite, agar-gelatin phantom, polyurethane foam, water with glass beads, cornstarch/flour-gelatin phantom, and magnesium silicate gels (Brude and Adler, 1995). In this project, agar-gelatin and cornstarch-gelatin phantoms were used at first to simulate the echogenicity of parenchymal tissue; however, they typically take two hours to construct and require constant stirring of the solutions to keep the scatterers suspended. Also, long heating time of the gelatin solution may increase the stiffness of the gel and influence the tissue-mimicking effect (Xu, personal communication, 2010).

Bude and Adler proposed a method of producing an easily made and low-cost tissue-mimicking phantom with psyllium hydrophilic mucilloid fiber (which is found in sugar-free Metamucil®) as the scatterers and gelatin as the medium (Bude and Adler, 1995). "This phantom does not require intermittent stirring during cooling until congealing of the mixture occurs, which could significantly reduce the time cost while keeping comparative performance of acoustic qualities as the other phantoms" (Bude and Adler, 1995). The detailed process of making the gelatin-Metamucil phantom (Chen, personal

communication, 2010) is described in Appendix B.

Similar to starch gelatinization, the gelatin granules are insoluble in cold water, and when heated in a water suspension, the granule begins to swell tangentially at a certain critical temperature (around 35 – 40 ºC) (Pomeranz, 1985). During cooling and congealing, the linear gelatin molecules "zipper" together wherever they can so that the elastic network of a gel can be generated (Pomeranz, 1985). "When refrigerated, the gel could be preserved for a long time because of the promoted retrogradation by cold storage; however, if not refrigerated, it may result in syneresis (extraction of a liquid from a gel) of a watery fluid from the gel which is literally pushed out of the swollen granule by the gradual association of the gelatin molecules" (Pomeranz, 1985). When this happens, the elasticity of the gelatin phantom can be significantly changed versus time (Pomeranz, 1985). Therefore, whenever a comparison between two elasticity measurements of the phantom needs to be conducted, the measurements must be taken within 60 minutes of each other so that changes of phantom elasticity are negligible.

The stiffness of the phantom can be adjusted by changing the amount of gelatin powder used. The amount of Metamucil powder can be adjusted to achieve the recommended scattering coefficient without generating sedimentation at the phantom bottom. The acoustic properties can be measured experimentally as shown in the next section. The elasticity properties can be measured using the Instron machine as the verification data for the transient elastography measurement results.

Mechanical Platform

The entire mechanical stage for the experiment is shown in Fig. 6 and Fig. 7. Two supports (Support #1 and Support #2) with translating tracks were designed and made so that both the phantom loaded acrylic plastic plate (about 3 lb.) and the vibrator (about 1 lb.) could be moved up and down freely and measurably. A bar-type hole (3 in. by 1 in.) was made in the middle of the plastic plate so that the 1D single element ultrasound transducer could touch the lower surface of the phantom. Both the vibrator and the ultrasound transducer were mounted on the stage with an accurate hex-direction translating control. The vibrator piston and the ultrasound transducer surface can be calibrated to be in the same vertical axis before experiments. Then the translating stage can accurately and simultaneously move the vibrator and transducer coaxially in order to create 2D elasticity images.

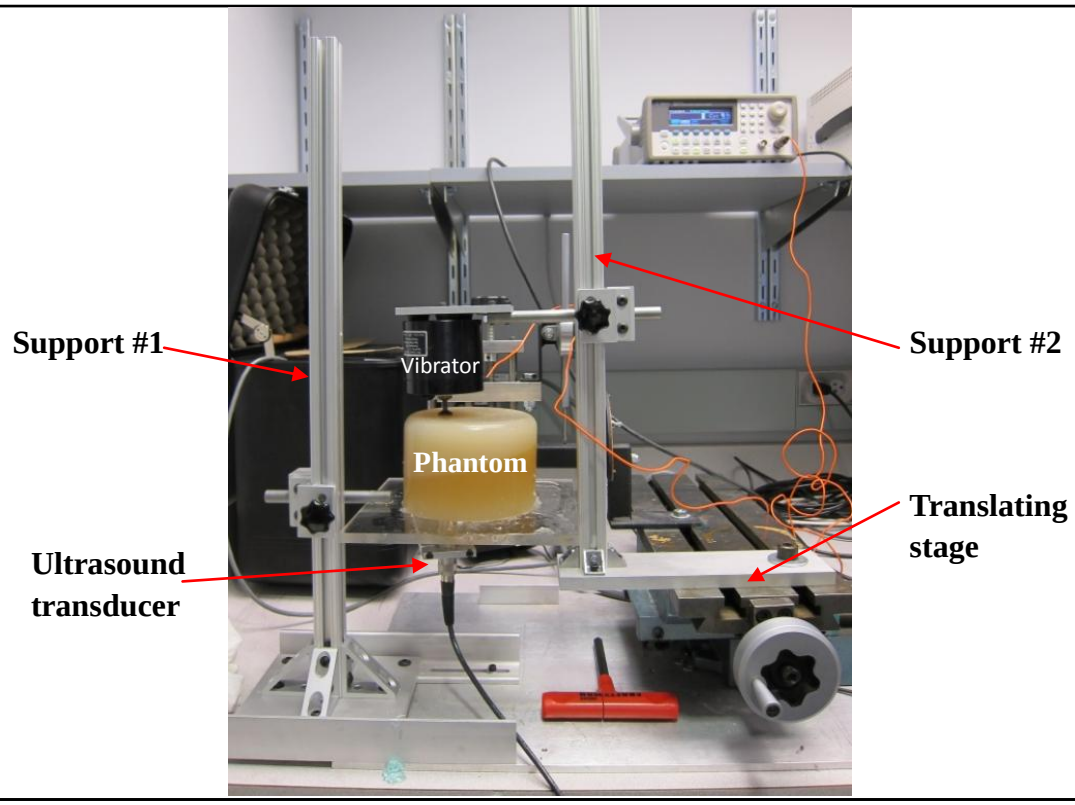

Figure 6. Mechanical platform for ultrasound transient shear wave elasticity imaging.

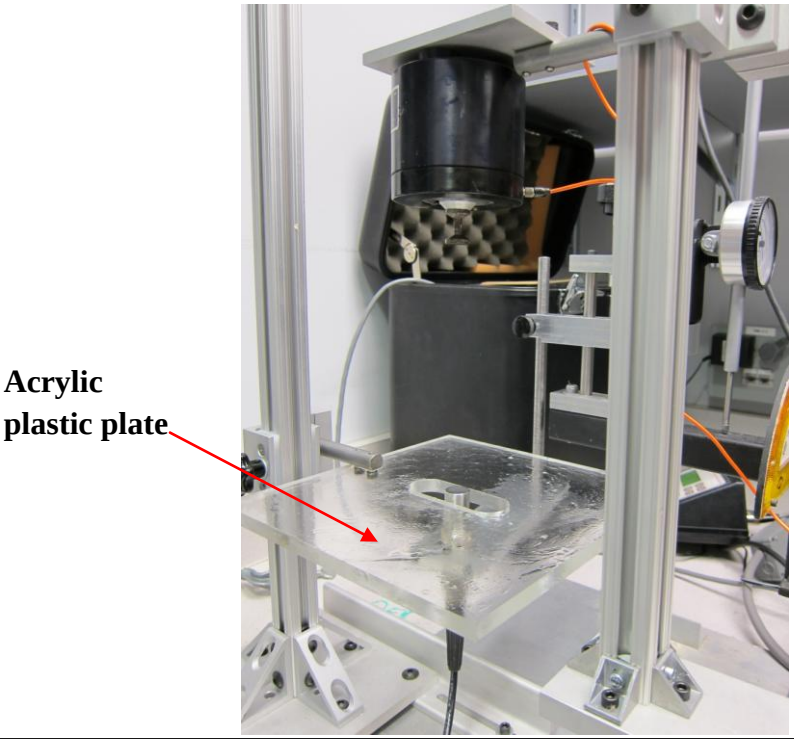

Figure 7. Specially designed acrylic plastic plate for phantom loading and ultrasound transducer imaging.

LabVIEW Program

A LabVIEW (National Instruments, Austin, TX) program was created by Dr. Greg Bashford and revised by the author to synchronize and manipulate the ultrasound transducer pulser, the data acquisition board, the digitizer and the digital counter (connected to the function generator for the vibrator). The program front panel is as shown in Fig. 8, and the "G-code" (graphical block diagrams of the program structure) are in Appendix E. The program accesses the digitizer memory and fetches the selected frame of echo signals for the user. The user can adjust the trigger delay in order to collect the correct depth range of the signal, and can also adjust the desirable number of time ensembles and number of depth samples. Acquired data can be saved in binary format and loaded into Matlab (Mathworks, Natick, MA) for further processing.

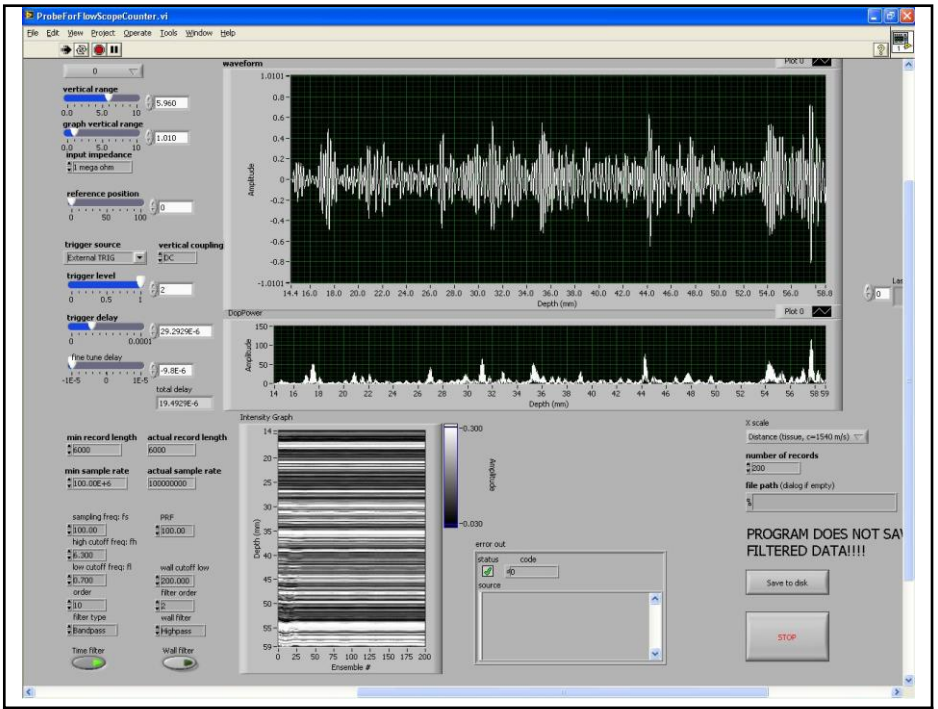

Figure 8. LabVIEW program front panel.

Methods

Green's Function Simulation

As mentioned in Chapter 2, a Green's function precisely predicts the displacement field generated by a Heaviside time dependence of a point force in the near field. The practical displacements that we measured were calculated from successive ultrasound A-lines, which are introduced in details in the following sections. Thus, in order to adapt the Green's function to our experiments, the time derivative of the Green's function is calculated as shown in Appendix A (Catheline et al., 1999b) to obtain a delta excitation.

The simulation code was composed and executed in Matlab. The full program is shown in Appendix D, part (b). The inputs of the simulation include total simulation time, phantom density, shear modulus of the phantom, phantom depth, vibration signal, vibration starting time, compressional wave and shear wave velocities. A typical simulated axial displacement field of an elastic solid generated by a 150 Hz damped sinusoid source vibration in 3D mesh plot is shown in Fig. 9. Fig. 10 shows the seismic plot of the displacement field, where displacements at each layer are plotted versus time independently.

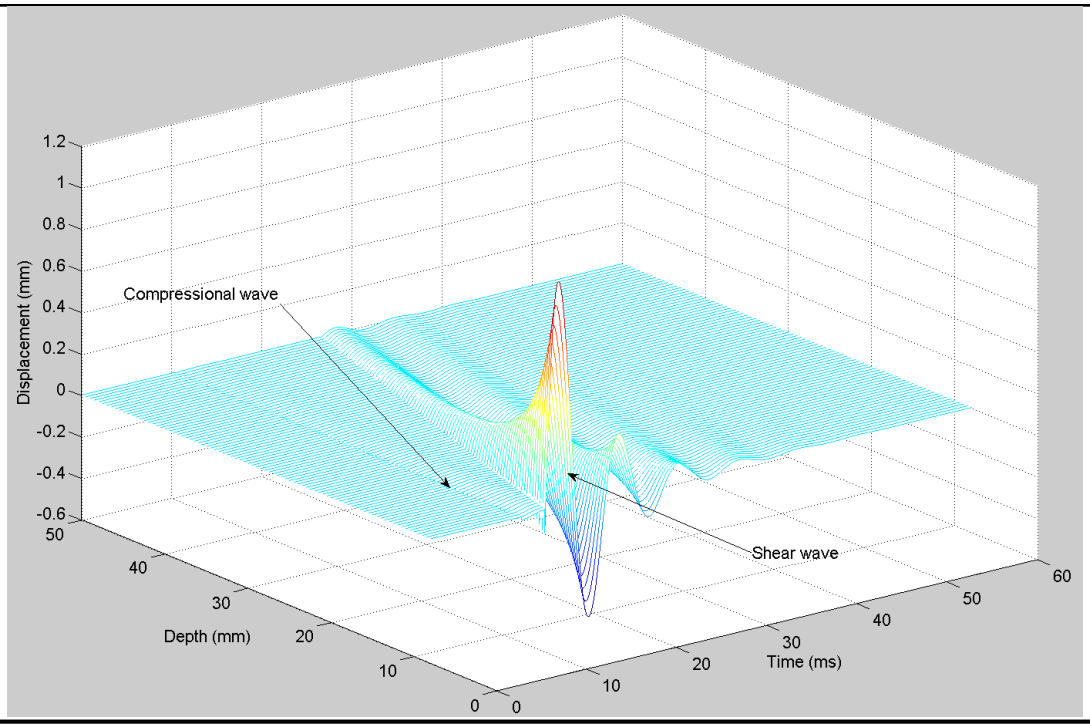

Figure 9. 3D mesh plot of the displacement field, with visible compressional wave and shear wave.

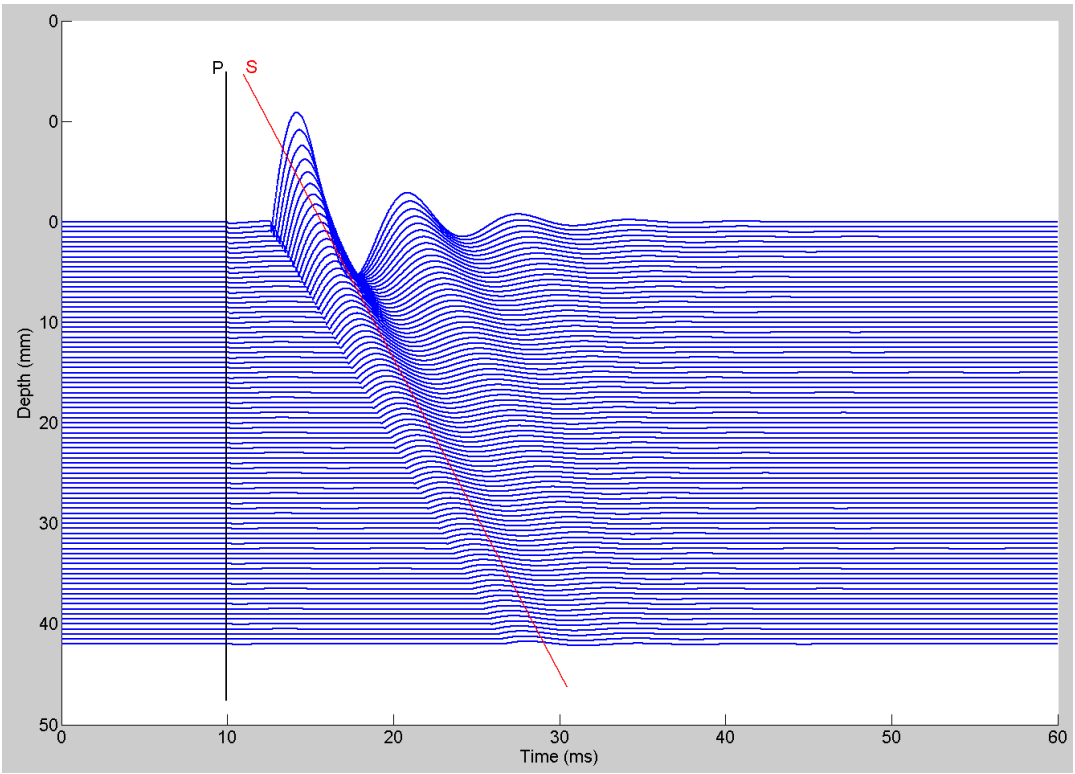

Figure 10. Seismic plot of the displacement field. P: compressional wave. S: Shear wave.

The simulated solid was a semi-infinite elastic isotropic soft tissue with shear modulus of 10 KPa. From the simulation we can see that both the compressional wave (P) and the shear wave (S) are visible in the displacement field. The compressional wave, which was propagating at about 1500 m/s, was immediately generated after the point source vibrating vertically to the solid surface. After the compressional wave, the shear wave was generated and also started to propagate from the surface of the solid to the deep side. Because the shear-wave velocity, which can be theoretically calculated using Eqn. (1), is much smaller than the compressional wave velocity, an obvious propagation delay is observed in the displacement field. This delay can be used to estimate the phase velocity of the shear wave. Also, we see that the shear wave amplitude attenuates quickly as the depth increases, which well matches the mechanical wave propagation theory. Meanwhile, as the major energy carrier of the vibration, the shear wave amplitude dominates, which is characteristic of a soft biological medium (Catheline et al., 1999a).

In order to test the simulation accuracy, an inverse-calculation experiment was conducted to calculate the shear modulus from the simulated displacement field, which was used to compare with the simulation input of the solid's shear modulus (10 Kpa).

The shear wave phase velocity can be calculated by performing spectral analysis of the displacement at each depth. Since all the displacements in different depth layers are under the same time frame, the phase information of each displacement can be extracted with the Hilbert transform performed on each depth layer, as shown in Fig. 11. The phase map can be matched exactly to the displacement field, and the phase fluctuations caused by both the

compressional wave and the shear wave can be seen. Since the vibration source is a damped sinusoid signal and the actual vibration is only in the first cycle, only the phase along the latest starting time point at the greatest depth was plotted to calculate the phase gradient along with depth ($\frac{\partial \varphi}{\partial z}$), as shown by the black solid line in Fig. 11. The shear-wave velocity (C_s) is given by (Catheline et al., 1999)

$$C_s = \omega \left(\frac{\partial \varphi}{\partial z}\right)^{-1}, \tag{9}$$

where ω (rad/sec) is the center angular frequency of the vibration.

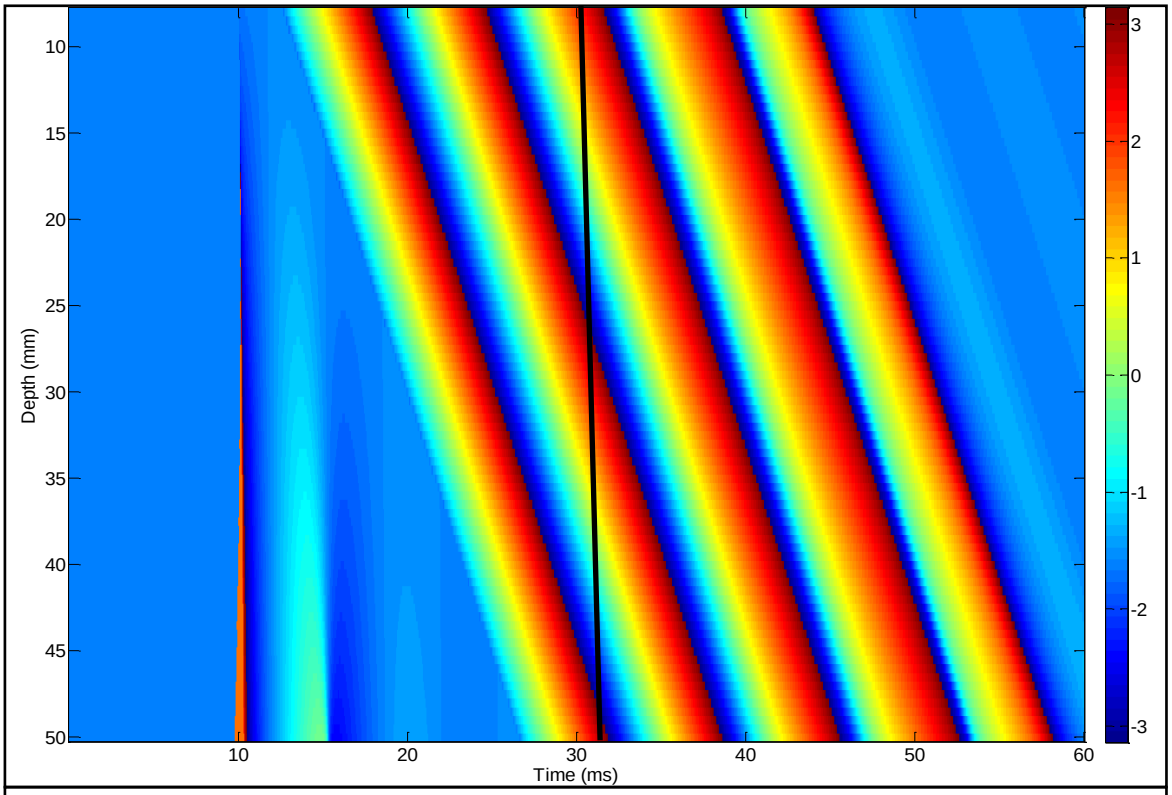

Figure 11. Phase plot from the Hilbert transform of each depth layer. The colorbar is with the unit of radians. Phases along the black solid line were plotted.

Acoustic Properties Measurement

Selfridge (Selfridge, 1985) proposed a classical method of measuring acoustic velocity, impedance, and attenuation of materials using a gimbal jig in a large water tank. In these studies, a simplified experiment set-up was used to estimate the acoustic properties of the tissue-mimicking phantom, as shown in Fig. 12. A sound damping rubber with serrated surface was put beneath the phantom to damp the penetrating ultrasound signal, so that only a negligible amount of ultrasound signal is reflected by the beaker bottom and a clear echo signal of the lower surface of the phantom can be obtained.

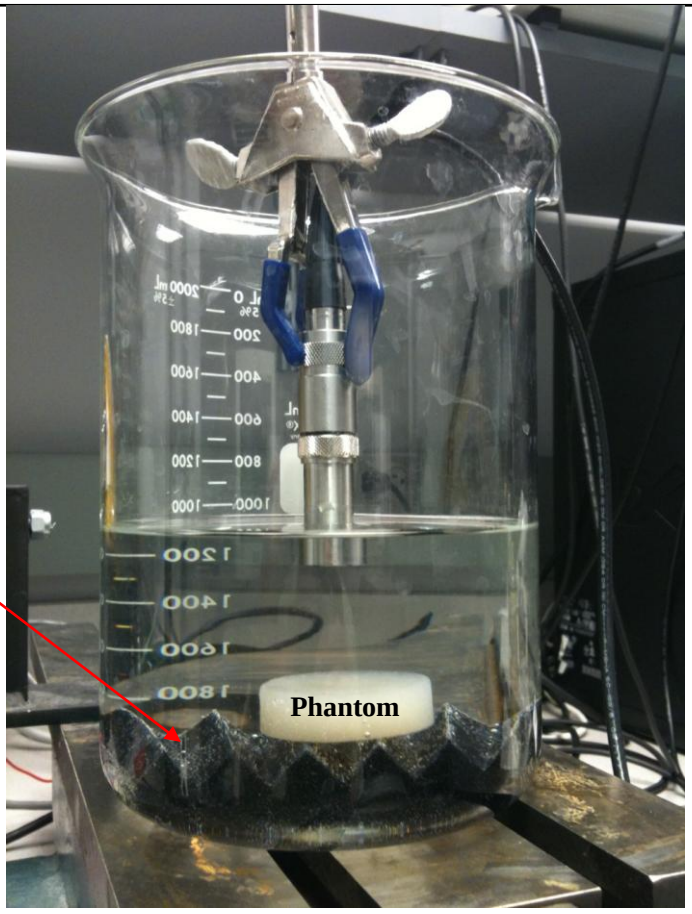

Figure 12. Experiment set-up for acoustic properties measurement.

A typical measured echo signal is shown in Fig. 13. The relative position between the transducer surface and phantom surface was carefully adjusted until echo amplitudes are maximized. Two reflection peaks different amplitudes are observed, with the greater peak (with amplitude of A_1) corresponding to the reflected ultrasound signal from the upper surface of the phantom and the smaller peak (with amplitude of A_2) corresponding to the lower surface. The time delay between the two surfaces, Δt, can be estimated by the equation,

$$\Delta t = \frac{N}{f_s}, \tag{10}$$

where N is the number of depth samples between the two surface reflections, and f_s is the sampling frequency of the ultrasound signal digitizer. The actual distance, d, between the two surfaces (the thickness of the phantom) could be carefully measured using a micrometer in the water, since the thickness measured in air may be less than that measured in water due to buoyancy. Considering the time delay is caused by a round-trip travel of the ultrasound through the phantom, the sound speed in the phantom (c) can be calculated as,

$$c = \frac{2d}{\Delta t}. \tag{11}$$

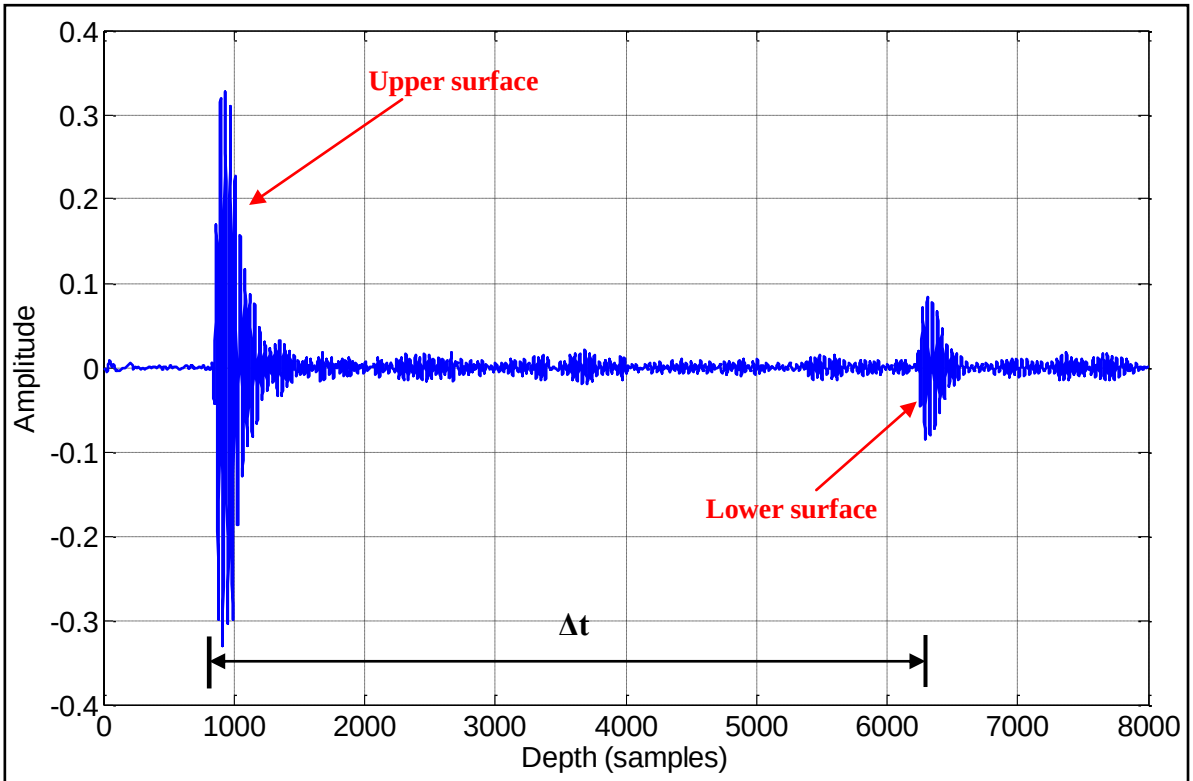

Figure 13. The signal of acoustic properties measurement.

Knowing the sound speed in the phantom, we can calculate the acoustic impedance (sound pressure over the particle velocity) of the phantom by (Selfridge, 1955):

$$Z_p = \rho c, \tag{12}$$

where ρ is the phantom density and Z_p is the acoustic impedance of the phantom. The reflection coefficient (R) of the phantom upper surface can then be estimated (Selfridge, 1985):

$$R = \frac{Z_p - Z_w}{Z_p + Z_w}, \tag{13}$$

where Z_w is the acoustic impedance of water. Along with reflection by the upper interface, some of the ultrasound energy continues transmitting into the phantom. The transmission coefficient (T_1) is given by (Selfridge, 1985)

$$T_1 = \frac{2Z_p}{Z_p+Z_w} = 1 + R. \quad (14)$$

When arriving at the lower surface of the phantom, a portion of ultrasound signal penetrates through the interface and is almost completely attenuated by the damping rubber. The remaining energy in the signal is reflected back by the interface with a reflection coefficient of $-R$ (Selfridge, 1985). When this portion of ultrasound signal arrives at the upper interface of the phantom, part of the signal is reflected towards the bottom of the phantom, and the rest continues transmitting through the interface towards the ultrasound transducer. The transmission coefficient here (T_2), is given by (Selfridge, 1985)

$$T_2 = \frac{2Z_w}{Z_p+Z_w}. \quad (15)$$

Assuming no ultrasound signal loss in the phantom, the ratio between A_1 and A_2 should be (Selfridge, 1985)

$$calculated\ \frac{A_2}{A_1} = T_1 \times T_2 = 1 - R^2. \quad (16)$$

To actually obtain the loss (dB/cm) in the phantom, we compare the measured ratio of A_1 and A_2 to the above calculated ratio as (Selfridge, 1985)

$$Loss\ in\ dB/cm = \frac{20log\left(\frac{calculated\ \frac{A_2}{A_1}}{measured\ \frac{A_2}{A_1}}\right)}{(2d)}. \quad (17)$$

Phantom Elasticity Measurement

Two methods of measuring the phantom elasticity were conducted in this project. One is the proposed ultrasound transient shear wave imaging method, and the other is the Instron machine (Instron 5566 Materials Testing Machine, Instron Corp., Canton, Massachusetts) test method.

The Instron test is a common method of measuring elasticity (Young's modulus) of the material, as shown in Fig. 14. In this project, an Instron 5566 machine was used to measure the Young's modulus of the phantom. Ten phantom samples in total were made for an Instron test, five of which ("Phantom #1") have a 5% gelatin concentration and the others ("Phantom #2") have a 10% concentration. The machine was calibrated first and then the pressing plate was carefully adjusted to touch the surface of the phantom. The software of the machine directly provides the user with raw data of the whole process, including force (F (N)) and deformation (Δl (mm)). With careful measurement of the phantom surface diameter (d (m)) and initial height (l (mm)), the Young's modulus of the phantom is given by (Stroshine and Hamann, 1994)

$$E = \frac{F/(\frac{\pi d^2}{4})}{\Delta l/l} = \frac{4Fl}{\pi d^2 \Delta l}. \quad (18)$$

The shear modulus is given by Eqn. (4).

Figure 14. Experiment set-up for Instron 5566 elasticity test.

The ultrasound transient shear wave elasticity imaging method was also used to measure the same groups of phantoms' elasticity. The experiment set-ups are shown in Fig. 15 and Fig. 16. A single element focused ultrasound transducer (Panametrics, type A382S, center frequency = 3.5 MHz, diameter = 0.5'', F/# = 1.5'') was positioned on the lower surface of the testing phantom, while a vibrator (Brüel & Kjær, type 4810) with a circular piston (7 mm radius) was positioned on the upper surface of the phantom. The vibration type, frequency and amplitude of the vibrator are all controlled by the function generator, and the piston of the vibrator is always vibrating perpendicularly to the surface of the phantom. The ultrasound transducer is controlled by the pulser (Panametrics, model

500PR), by which the transducer's pulse repetition frequency (PRF), damping factor, pulse height and receiving gain can be adjusted. Meanwhile, the pulser's transmitting PRF is also detected and shown on an oscilloscope (Tektronix, model TDS 3032B) in order to obtain the optimal frequency. The pulser triggers the digitizer and data acquisition system (National Instruments, NI PXI-8331) and sends received echo signals to the system. The digitizer (National Instruments, NI PXI-5122) is triggered by the pulser and the data acquisition system samples the digitized signal with a sampling frequency of 100 MHz. Because of the limited size of the data acquisition system memory, only the latest received and sampled signals are stored in memory. The user can use the LabVIEW program introduced above to fetch data from memory by clicking the "SAVE TO DISK" button on the interface. Simultaneously, the LabVIEW program also controls a digital counter (National Instruments, BNC 2120) which triggers the function generator externally. The controlled digital counter only sends out 1 to 2 triggering signals per second to the function generator, so that the vibrator will only vibrate once or twice per second. This provides the system with enough time to collect the entire physical process of the compressional wave and shear wave propagation, while preventing the next period of vibration process from overlapping.

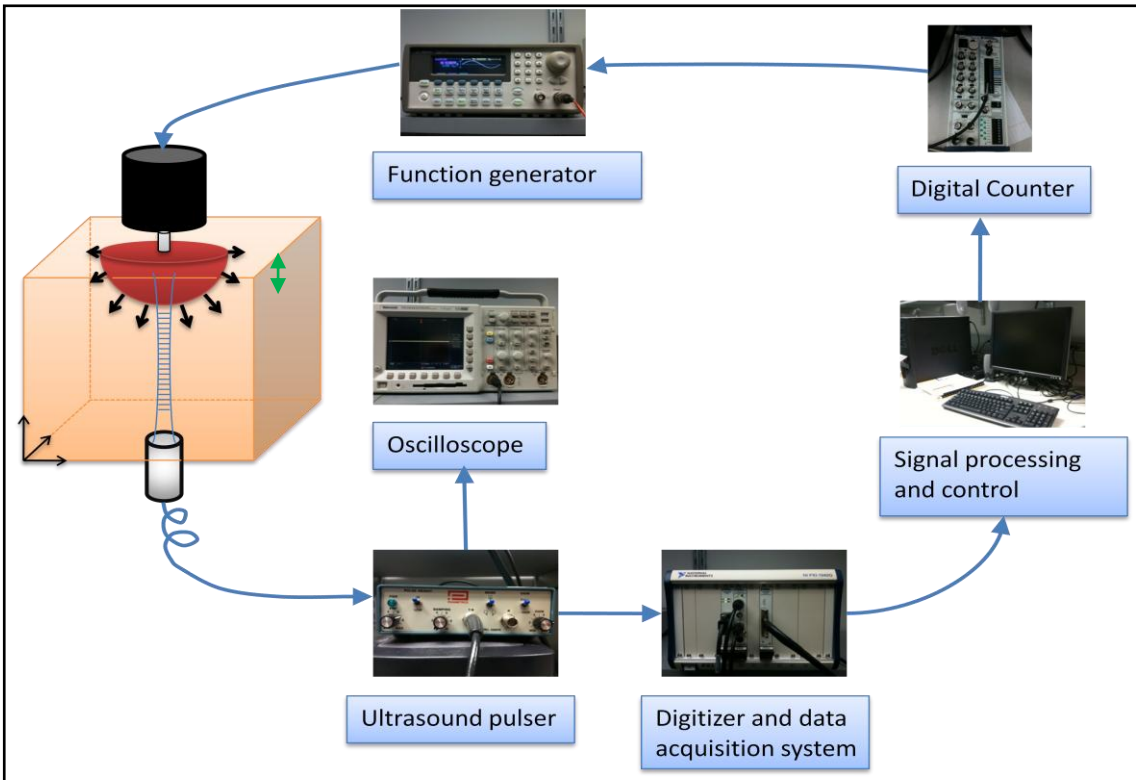

Figure 15. Experiment set-up for the ultrasound transient shear wave elasticity imaging system.

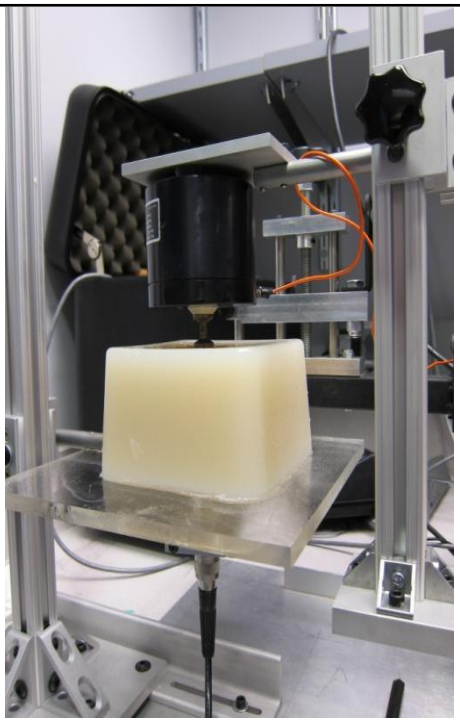

Figure 16. The cubic (11 × 11 × 7 cm) gelatin-Metamucil phantom and the set-ups for the vibrator and ultrasound transducer.

In order to compare with the phantom elasticity results measured by the Instron machine, the same group of gelatin-Metamucil phantom was also tested using the ultrasound transient shear wave elasticity imaging method introduced above. One 5% gelatin-Metamucil phantom and one 10% gelatin-Metamucil phantom were made at the same time with the samples tested with the Instron machine. Both of the phantoms have dimensions of 11 × 11 × 7 cm, so that the phantom depth is much greater than the piston diameter, and the phantom volume provides enough space for shear wave dissipation. Then, as long as diffraction effects and dissipation can be ignored, the measured phase velocity at the center frequency is equal to the shear velocity (Dutt et al., 1996). Experiments were conducted about 12 hours after phantom construction. The time between the Instron machine test and the ultrasound test was one hour. Therefore the elasticity changes versus time between the two testing methods were negligible.

The vibrator was set to generate a sinusoid with 50 Hz frequency. The choice of 50 Hz vibration frequency is a trade-off between enhanced diffraction effects caused by a lower frequency and increased attenuation of the shear wave caused by higher frequency (Sandrin et al., 2002). In practice trials, it was shown that 50 Hz is the optimal frequency that could be used in our experimental set-ups, especially for the proposed phantom with 7 cm in depth.

The PRF of the transducer was set to be 1.5 KHz. Theoretically, the greater the PRF, the better the time resolution, and the better potential tracking of the axial displacement of the phantom. However, in practice experiments, we noticed that a large PRF causes a

severe interference between transmitting energy from one pulse and reflected energy from a previous pulse, which can result in a poor or even wrong tracing of the displacement. By carefully adjusting the PRF and comparing the actual experimental effect, we finally chose 1.5 KHz to be the optimal PRF for our experiment. The loss of time resolution can be compensated for later using an interpolation technique, as shown below.

After collecting the echo signal containing vibration data, a series of signal processing programs were written in Matlab (Appendix D) to measure the displacement field and the shear-wave velocity. The framework of the entire processing procedure is shown in the flowchart in Fig. 17.

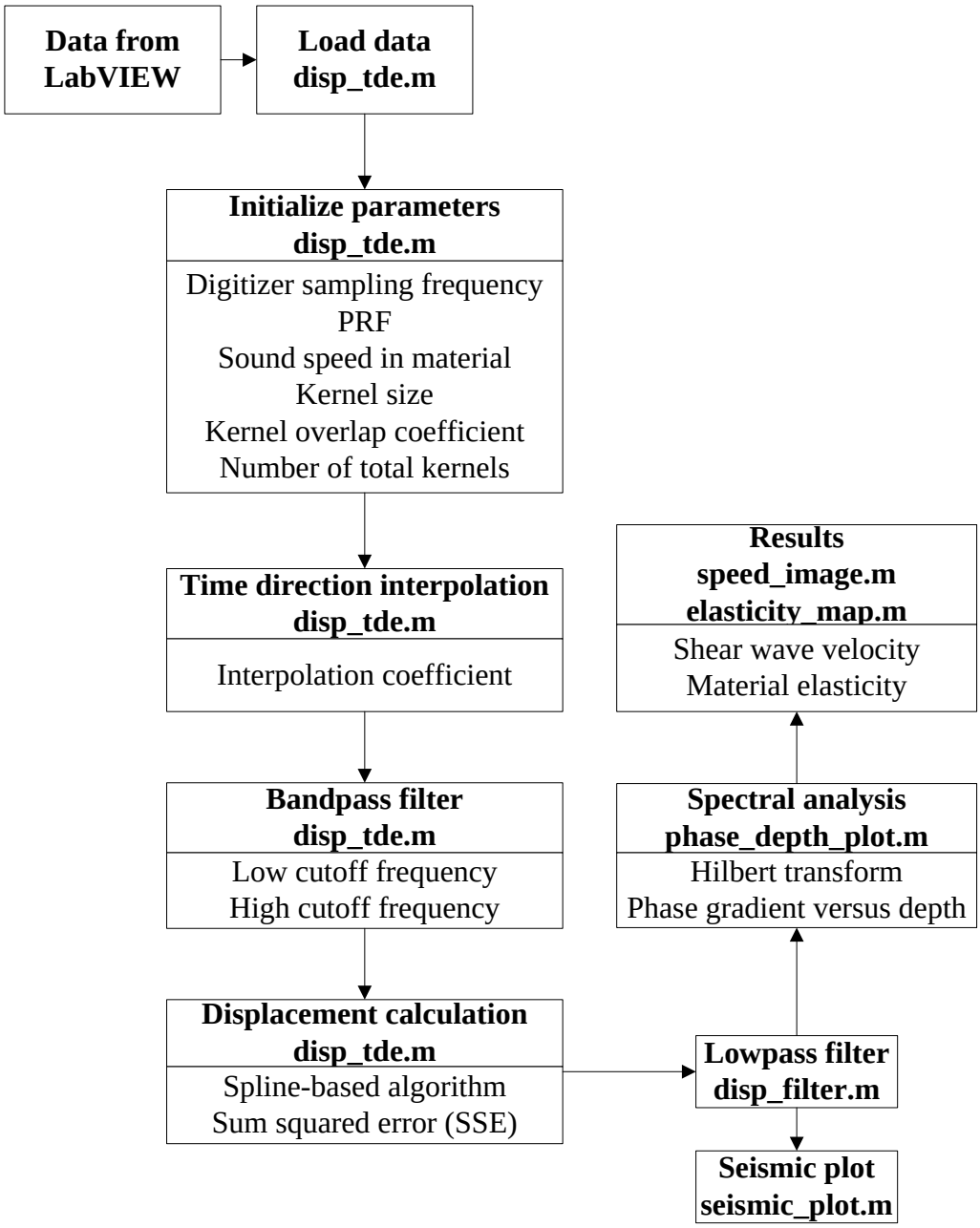

Figure 17. The flowchart of signal processing for displacement calculation and shear-wave velocity estimation. The names of the corresponding Matlab programs (.m file) are given in the flowchart. The Matlab programs are in Appendix D.

The Matlab code loads the data first and initializes all input parameters. For better time resolution, a lowpass filter interpolation method (Matlab: *interp*) is used in the time direction to achieve a five-fold sampling rate as the original one. For instance, for an original PRF of 1.5 KHz, the interpolated data will be sampled at 7.5 KHz. After interpolation, the data is input into a bandpass filter to remove noise in each A-line which are out of the transducer frequency range. For the transducer with 3.5 MHz center frequency, usually a bandpass filter with a 1 MHz low cutoff frequency and a 6 MHz high cutoff frequency would be appropriate. Afterwards, each A-line is divided into a certain number of overlapping kernels with the kernel size approximately equal to a 1 mm layer (about 133 samples) inside the material. Typically a 50% overlap is chosen for the tradeoff between depth resolution and computational cost. The spline-based algorithm and the Sum Squared Error (SSE) algorithm then process each kernel along the time direction, saving the displacement raw data. The raw data is then filtered with a low pass filter (usually with the cutoff frequency equal to the center frequency of the vibration) to remove the false peaks and jitter errors. The final displacement field is shown in Fig. 18.

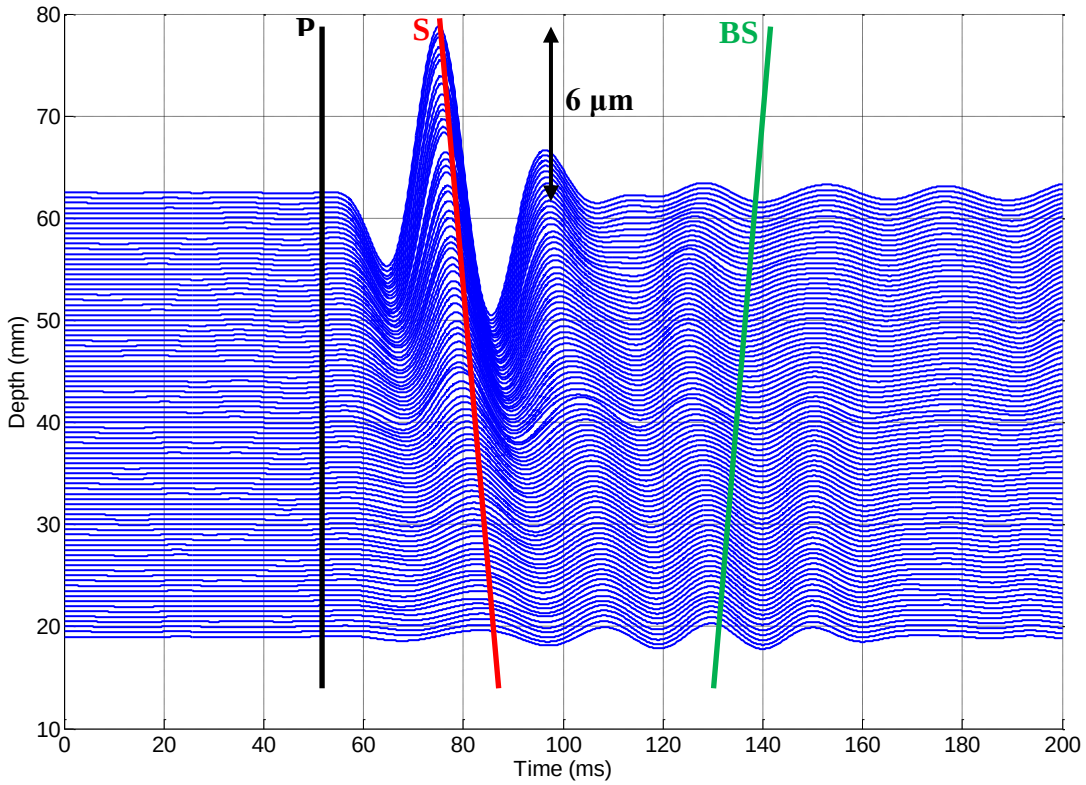

(a)

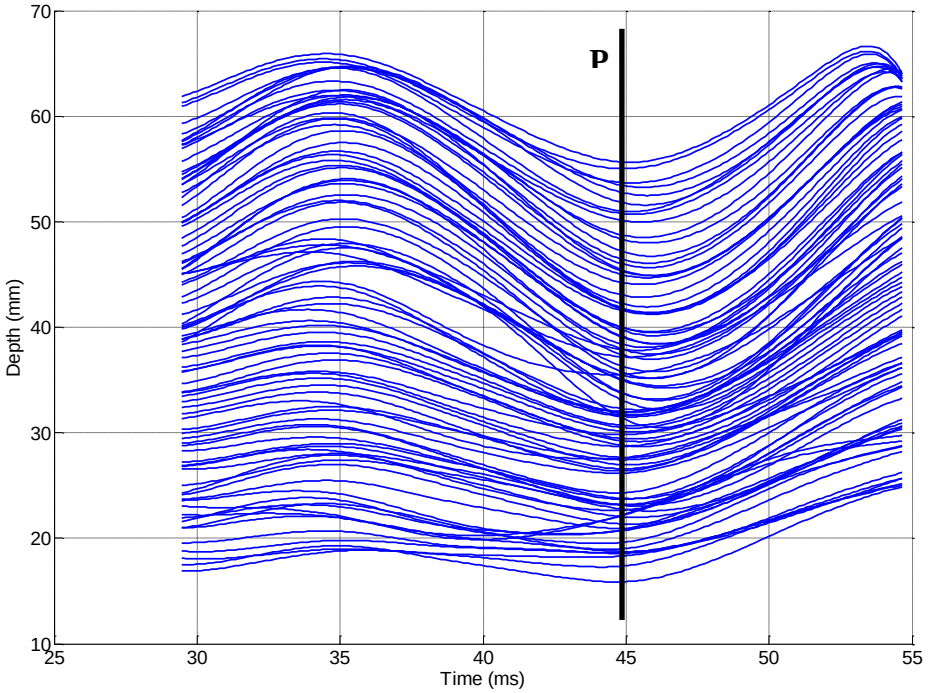

(b)

Figure 18. (a): displacement field generated by the vibrator, with visible compressional wave (P), shear wave (S) and reflected shear wave (BS). (b): Zoomed view of the compressional wave (P).

Compared with the simulated displacement field in Fig. 10, we can see that both the compressional wave (P) and shear wave (S) can be observed with similar shape and time relativity as in the simulation. However, because the actual phantom size is not infinite and the phantom bottom is touching the plastic plate and is not boundary free, we also observe a "back" shear wave (BS) which is generated when the shear wave reaches the opposite side of the phantom and reflects from the transducer back to the vibrator. In the spectral analysis part, only the displacements generated by the shear wave (S) are used since this area best represents the practical axial displacement generated by the transient shear wave.

Both of the 5% and the 10% gelatin-Metamucil phantoms were tested using the above experiment strategies. The results were further compared with the Instron test results.

Grape-olive Phantom

A grape-olive phantom was made to test the feasibility of using ultrasound transient shear wave imaging onto heterogeneous materials. The same gelatin-Metamucil phantom was used as the medium for holding the grape and the olives. One seedless grape, one horseshoe shaped hollow olive with a hole in the middle and a stuffed olive with pimento (cherry pepper) in the middle were put into the phantom, as shown in Fig. 19. The first layer of gel was poured into the box and allowed to congeal until it could support the weight of the grape and olives. Then a second layer of gel was poured in until it just covered the grape and olives, which are then trapped by this layer after congealing. Finally, the container was filled with the gel solution and put into the refrigerator.

Figure 19. Grape-olive phantom with one seedless grape, one pimento-stuffed olive and one hollow olive with a hole in the middle.

Bi-layer Phantom

A bi-layer phantom with 5% gelatin concentration in one layer and 10% concentration in the other was made to further test the heterogeneous material measurement feasibility and create an elasticity mapping image. The bi-layer phantom was made as in Fig. 20 with the same procedures as in Appendix C. The upper layer consists of 5% gelatin, and was poured onto the congealed 10 % gelatin layer with a tilted surface. The phantom is comparable in size to the homogeneous one introduced above, so the theory introduced above is still applicable. The vibrator and the transducer were moved coaxially by the translating stage and stopped every 2 mm to take vibration data. In total, 27 sets of data

were taken, corresponding to a lateral dimension of 54 mm.

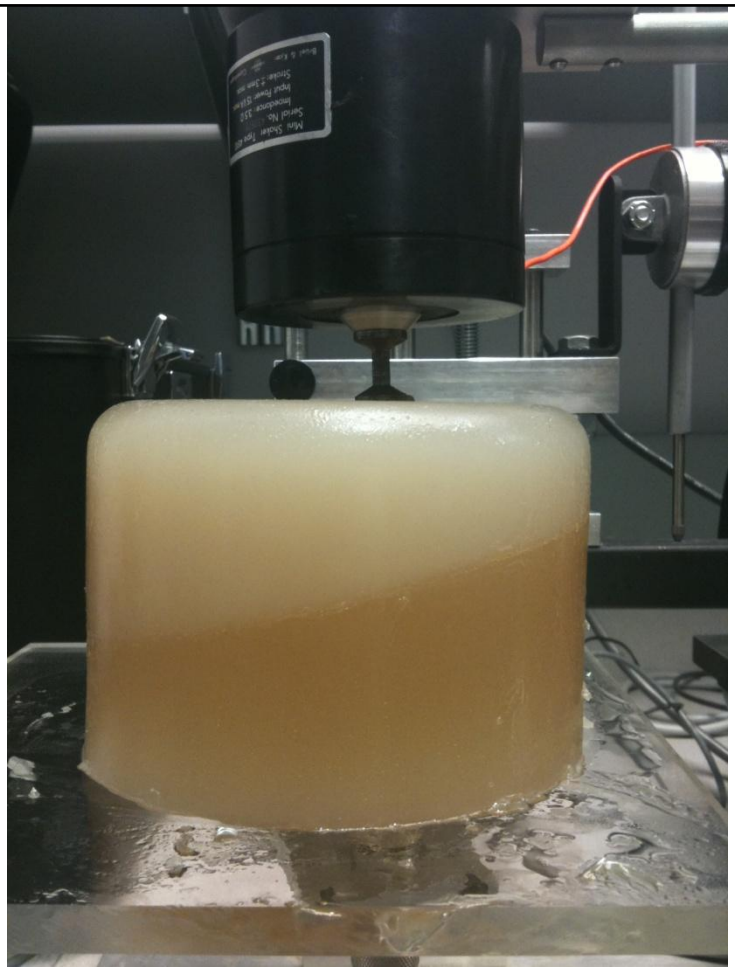

Figure 20. Bi-layer phantom with 5% gelatin phantom as the upper layer and 10 % gelatin phantom as the lower layer. The interface between the two layer was made tilted.

Results and Discussion

Green's Function Simulation

The phase along the sampled time point in Fig. 11 is plotted in Fig. 21. A linear fitting was performed and the phase gradient ($\partial\varphi/\partial z$) was estimated by the slope of the fitting line, which is 0.306 rad/mm. If this value is substituted into Eqn. (9) with a center frequency of 150 Hz, the resulting shear-wave velocity is 3.08 m/s. Given the simulated material shear modulus of 10 KPa, the simulated shear-wave velocity is given by Eqn. (1) and equal to 3.02 m/s with a density of 1100 Kg/m^3. The relative error between the inverse-calculation measurement and the simulated value is 1.99%.

Theoretically, the inversely measured shear-wave speed should be equal to the simulated speed. However, because the phantom is assumed to be incompressible and the Poison ratio is assumed to be 0.5, the simulation input compressional wave speed is an approximate value instead of a true calculated value from the infinite bulk modulus. This may result in biases in the inverse measurement since the compressional wave speed is involved in the simulation functions. However, as the relative error is small, the simulation and the inverse measurement technique indicate that the proposed shear-wave speed estimation method is feasible and accurate.

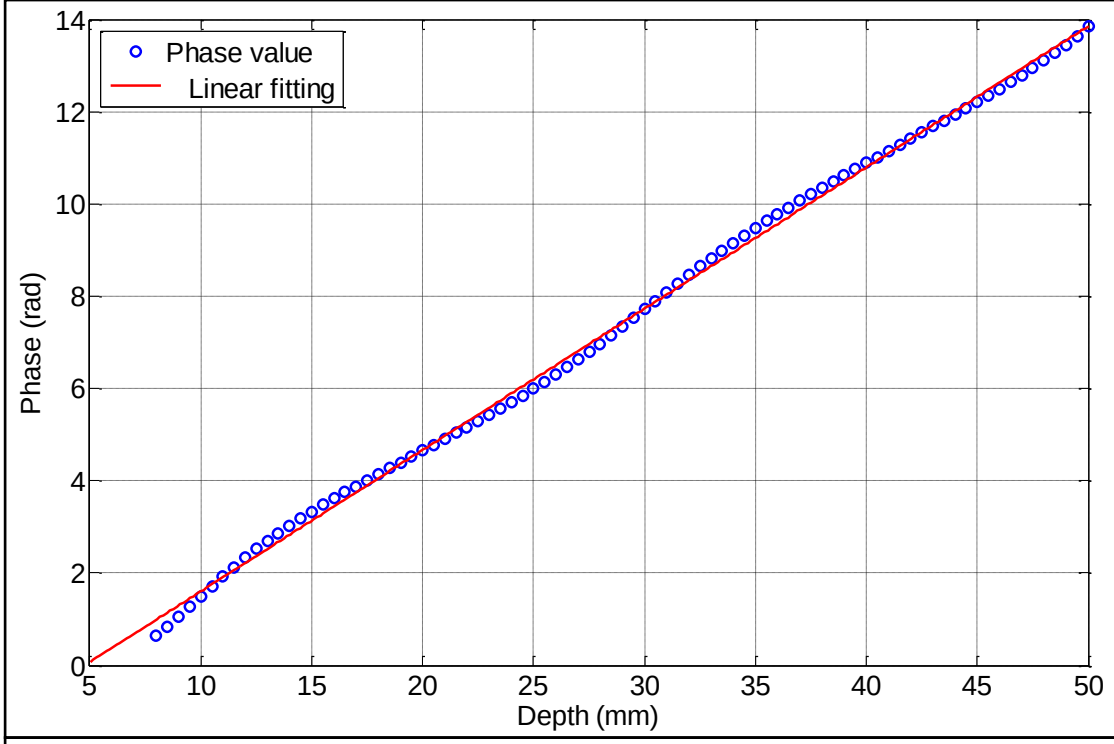

Figure 21. Phase-depth plot at the selected time point from Fig. 11.

Acoustic Properties Measurement

A cylinder shaped 5% gelatin phantom was made to measure the ultrasound speed. The thickness of the phantom was carefully measured ten times to get an average and standard deviation value, as shown in Table 1. The time delay between the two reflections as shown in Fig. 13 is 53.90 μs, and the sound speed given by Eqn. (11) is 1539 ± 15.02 m/s. The density of the phantom was measured in a graduated beaker with known mass, resulting in a value of 1.04 g/cm^3. Then the acoustic impedance of the phantom given by Eqn. (12) is 1.6 MRayls (kg/s·m^2 ×10^6). The acoustic impedance of water is 1.5 MRayls (Selfridge, 1985), so the reflection coefficient given by Eqn. (13) is 0.033. Then the calculated ratio of A_2 to A_1 given by Eqn. (16) is 0.9989. The measured ratio of A_2 to A_1 is 0.2648, and the loss

of amplitude in the phantom given by Eqn. (17) is 1.390 dB/cm. Given the 3.5 MHz center frequency ultrasound transducer, the loss is 0.40 dB cm^{-1} MHz^{-1}, which is well within a standard attenuation coefficient of 0.3 – 0.7 dB cm^{-1} MHz^{-1}.

Measurement #	**Thickness (mm)**	**Measurement #**	**Thickness (mm)**
1	41.46	6	41.55
2	41.28	7	41.28
3	42.25	8	41.00
4	42.01	9	41.10
5	41.13	10	41.62
Avg*	**41.47**	**Std***	**0.4048**

*Avg is short for average and Std is short for standard deviation here after.

Table 1. Phantom thickness measurements.

The measured acoustic properties indicate that the gelatin-Metamucil phantom can be constructed to possess attenuation and speed of propagation values characteristic of soft tissues. The measured sound speed in this phantom is very close to the average sound speed of 1540 m/s in soft tissues. For the grape, olive, tendon and 10% gelatin phantom, the measured depth biases can be negligible because of the limited object size. For example, given the ultrasound speed of 1540 ± 50 m/s, the measured depth of the grape, olive and tendon would vary about ±0.45 mm; for the 10% gelatin phantom in the bi-layer phantom, the measured depth would vary about ±1.3 mm. Therefore, we used 1540 m/s for all the depth calculations hereinafter.

Phantom Elasticity Measurement

The stress over strain curves of the Instron test are plotted in Fig. 22. It can be seen that the elasticity curves are nonlinear and the deformation involved with shear wave propagation is small, so that only the initial quasi-linear parts were selected for the Young's modulus calculation, as shown in Fig. 23. A linear fit was performed for each curve from 0 to 0.2 strain and the results are in Table 2.

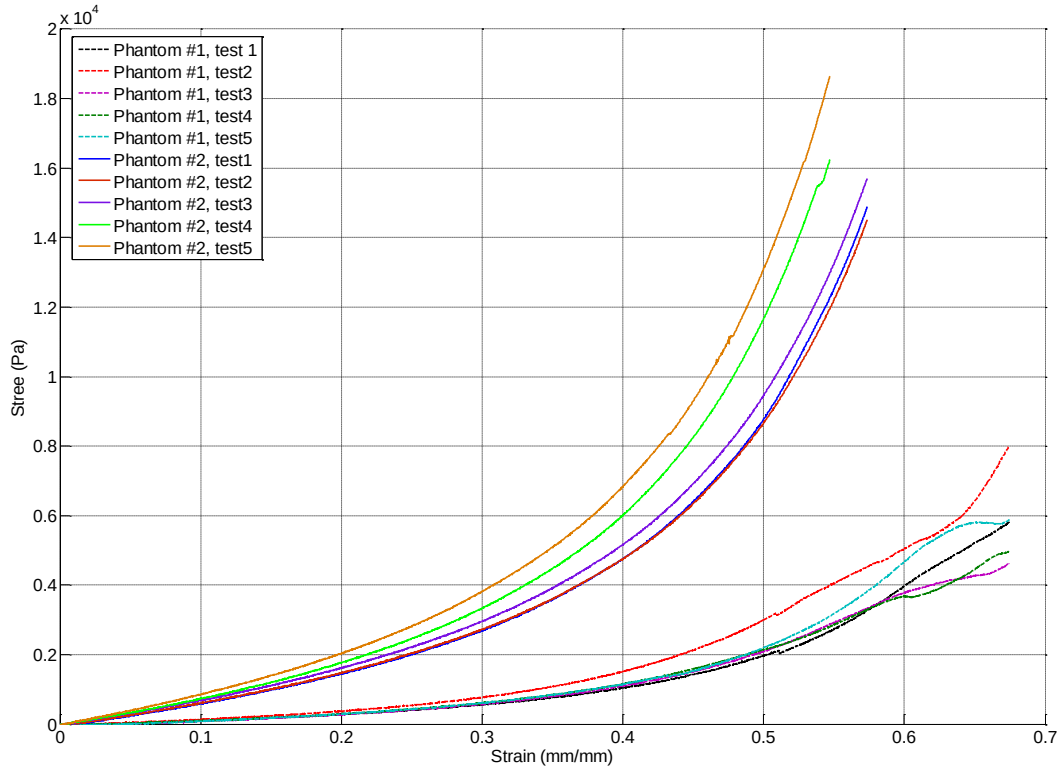

Figure 22. Stress over strain curves for all the samples of Phantom #1 and Phantom #2 from Instron machine.

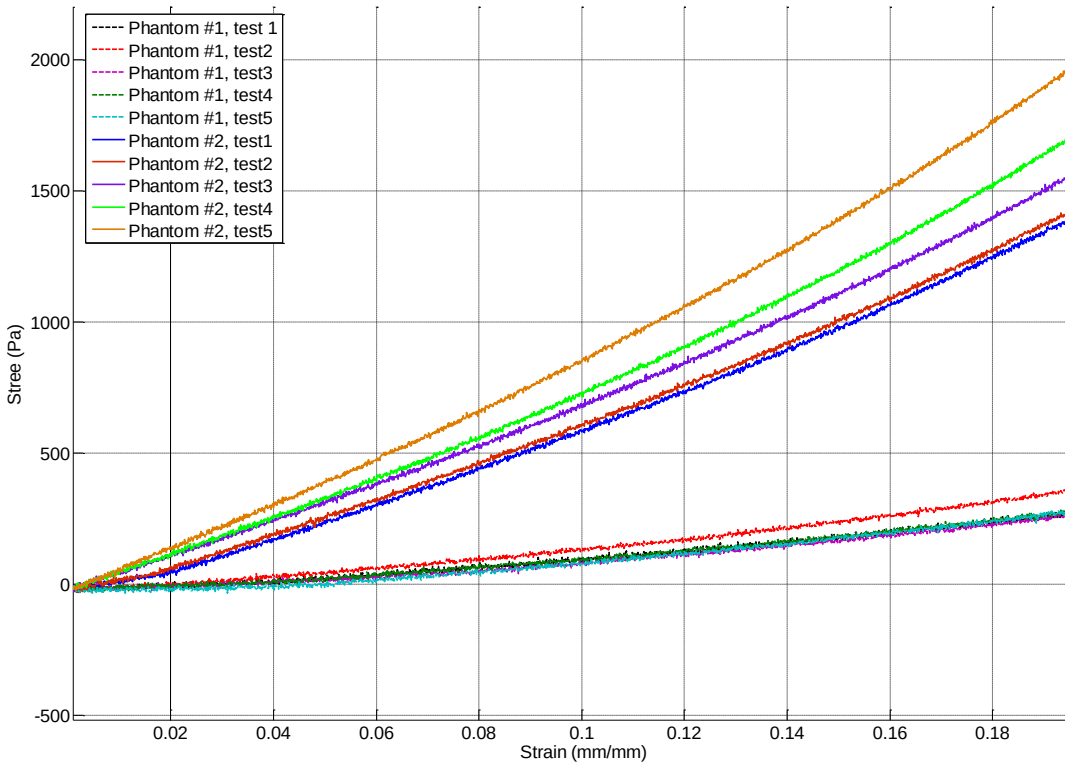

Figure 23. Quasi-linear part of the stress over strain curve, from 0 strain to 0.2 strain.

Instron test			
Phantom #1 (5% gelatin)		**Phantom #2 (10% gelatin)**	
Index	***E (Pa)**	**Index**	**E (Pa)**
Test1	1688	Test1	7544
Test2	2184	Test2	7650
Test3	1691	Test3	8179
Test4	1768	Test4	8796
Test5	1851	Test5	10140
Avg ± Std	**1836 ± 205.4**	**Avg ± Std**	**8462 ± 1061**

Ultrasound test					
Phantom #1 (5% gelatin)			**Phantom #2 (10% gelatin)**		
Index	***V (m/s)**	**E (Pa)**	**Index**	**V (m/s)**	**E (Pa)**
Test1	0.847	2240	Test1	1.75	10600
Test2	0.829	2150	Test2	1.73	10300
Test3	0.868	2350	Test3	1.73	10400
Test4	0.755	1780	Test4	1.74	10500
Test5	0.770	1850	Test5	1.66	9510
Avg ± Std	**0.814 ± 0.0491**	**2070 ± 222**	**Avg ± Std**	**1.72 ± 0.0356**	**10300 ± 435**

*E stands for Young's modulus and V stands for shear-wave velocity.

Table 2. Elasticity measurements using Instron test and ultrasound test.

The same spectral analysis method as in the simulation section was used for shear-wave velocity and Young's modulus measurements. A Hilbert transform was performed for each depth layer of the displacement field and the phase versus depth plot was selected by carefully picking the time point in shear wave (B) area. Fig. 24 shows a typical procedure of the ultrasound test, including a seismic plot of the displacement field, a phase map and a phase-depth plot. The measured Young's modulus is shown in Table 2.

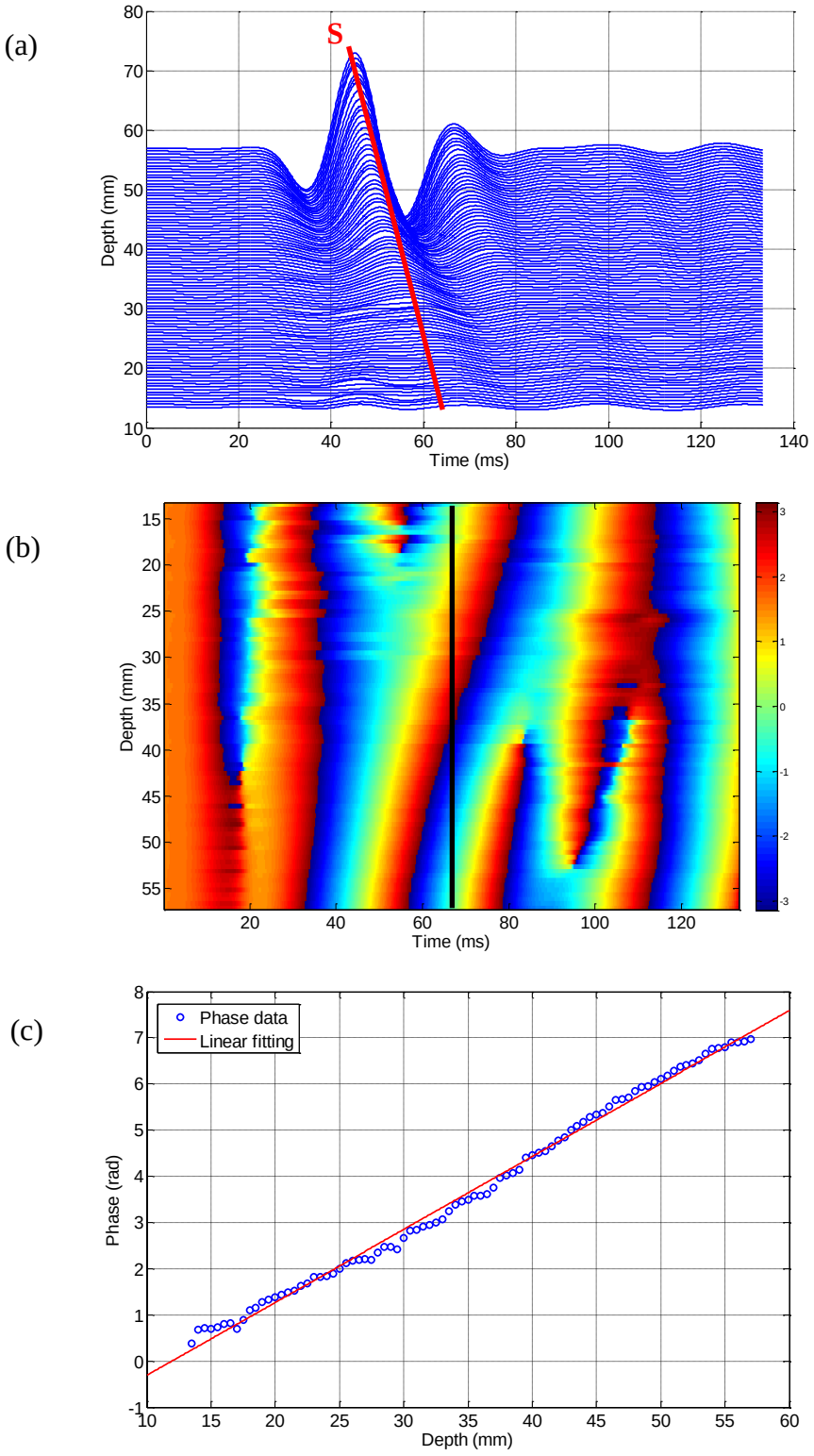

Figure 24. Procedures of measuring phantom elasticity using ultrasound. (a): displacement field; (b) phase map from spectral analysis; (c) phase-depth plot for shear-wave velocity calculation.

Both of the two measurement methods have biases during the measurement, and the main reasons resulting in these biases are summarized as below:

1. The Instron 5566 machine (with maximum capacity of 10 KN) is relatively "large" to the tested phantoms, i.e., the machine is designed to measure moduli on much stiffer samples. So testing the relatively soft phantoms with this machine may result in biases of the force measurement.
2. The manual measurement of the phantom surface area and phantom initial height can result in biases in the measurement.
3. In order to test the normal elasticity of the proposed phantom, all ten phantom samples were made without refrigeration. The five samples of Phantom #1 were very soft and more difficult to be removed from the mode, and there were a small amount of ruptures caused by handling five soft samples.
4. Measured shear-wave speed at low excitation frequencies can be greater than the actual speed because of diffraction effects as introduced in Chapter 2. We used a 50 Hz vibration frequency for this experiment, which is at the lower end of normal excitation frequencies for this experimental method. So as can be seen from the results, the ultrasound measurements are all greater than the Instron measurements.

Although ultrasound tests did not produce equivalent values of Young's modulus as the Instron tests, it is more important to see that the ratio of the values is similar. In the Instron test results, the Young's Modulus of Phantom #2 is about 4.6 times that of Phantom #1; and in the ultrasound test results, this ratio is about 5, and the ratio of the shear-wave speed is

about 2.1, which is the square root of the shear modulus according to Eqn. (1). Therefore, we feel confident about the ultrasound shear wave elasticity measurements because they can estimate the relative hardness of the material as verified by the Instron tests. Although the ultrasound tests may not produce elasticity measurements comparable to literature values or Instron tests, it can estimate the correct comparative elasticity when all the materials are tested by use of the ultrasound method.

Grape-olive Phantom

Figs. 25, 26 and 27 show the measurement results for the grape-olive phantom. First, B-mode images were formed to better understand the phase map. The image is oriented such that the vibrator is set on the top and the transducer is set on the bottom. An obvious change of shear-wave speed is seen for all three cases. A linear fit was performed on the data from the normal phantom and the grape/olive phantom separately. The shear-wave speeds in grape, hollow olive, and stuffed olive were measured to be 75.5 m/s, 31.9 m/s, and 44.9 m/s respectively. We assume that the phantom is locally homogeneous and purely elastic ($\lambda >> \mu$), so shear-wave speeds can still be converted to Young's modulus in this phantom. If we assume the grape, hollow olive and stuffed olive have the same density of 2.5 g/cm^3 (wiki.answer.com), then the Young's modulus of grape is 42.8 MPa, the hollow olive is 7.64 MPa, and the stuffed olive is 15.1 MPa. Thus, the grape is the stiffest among the three objects, the stuffed olive is softer, and the hollow olive is the softest. By hand palpation, we can feel that grape is more elastic and stiffer than both of the olives. Interestingly, we can observe a small change of shear-wave speed in the cavity area of the

hollow olive. This is because the gel solution entered into the cavity during phantom making. The value of the shear-wave speed in the cavity is about 8.16 m/s (corresponding to a Young's modulus of 0.210 MPa), which is greater than the speed in the normal phantom below the olive (about 3 m/s). This is caused by the limited size of the olive cavity and the heterogeneous medium. For the stuffed olive, the pimento in the middle has similar elasticity as the surrounding olive, so no obvious shear-wave speed change was observed in this case. For all three cases, it was seen that the phase in the phantom above the objects seems more random. The main reason for the poor tracking of vibration displacement in this area is that the ultrasound signal was significantly attenuated at the object boundaries where the acoustic impedance changes. In practice, the echo signal amplitude in this area is much smaller than the signal on the other side of the object, which can result in low signal-to-noise ratio (SNR) echo signal and poor displacement estimation.

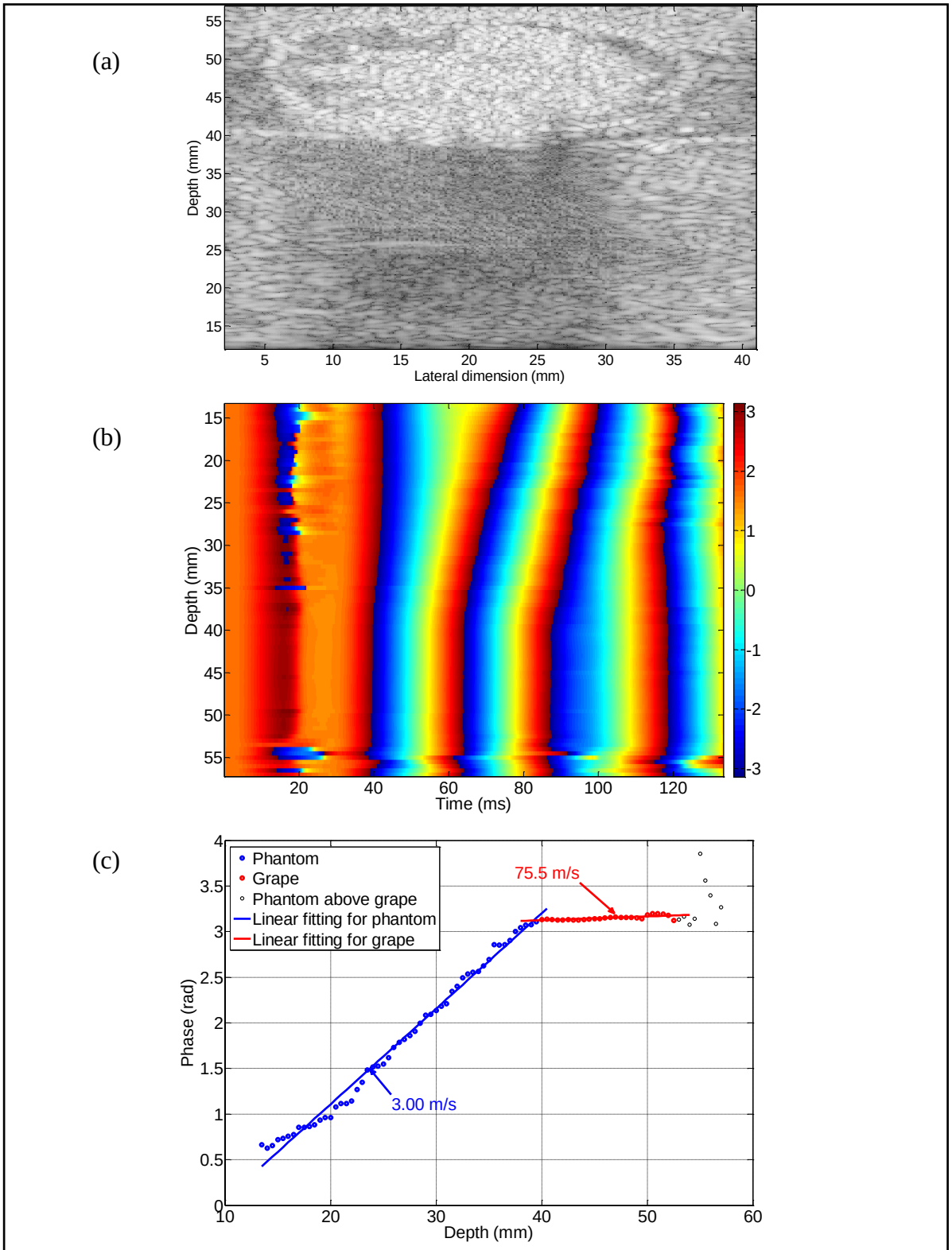

Figure 25. Grape test in grape-olive phantom. (a) B-mode image; (b) phase map, the colorbar is with the unit of radians; (c) phase-depth plot and shear-wave velocity measurement.

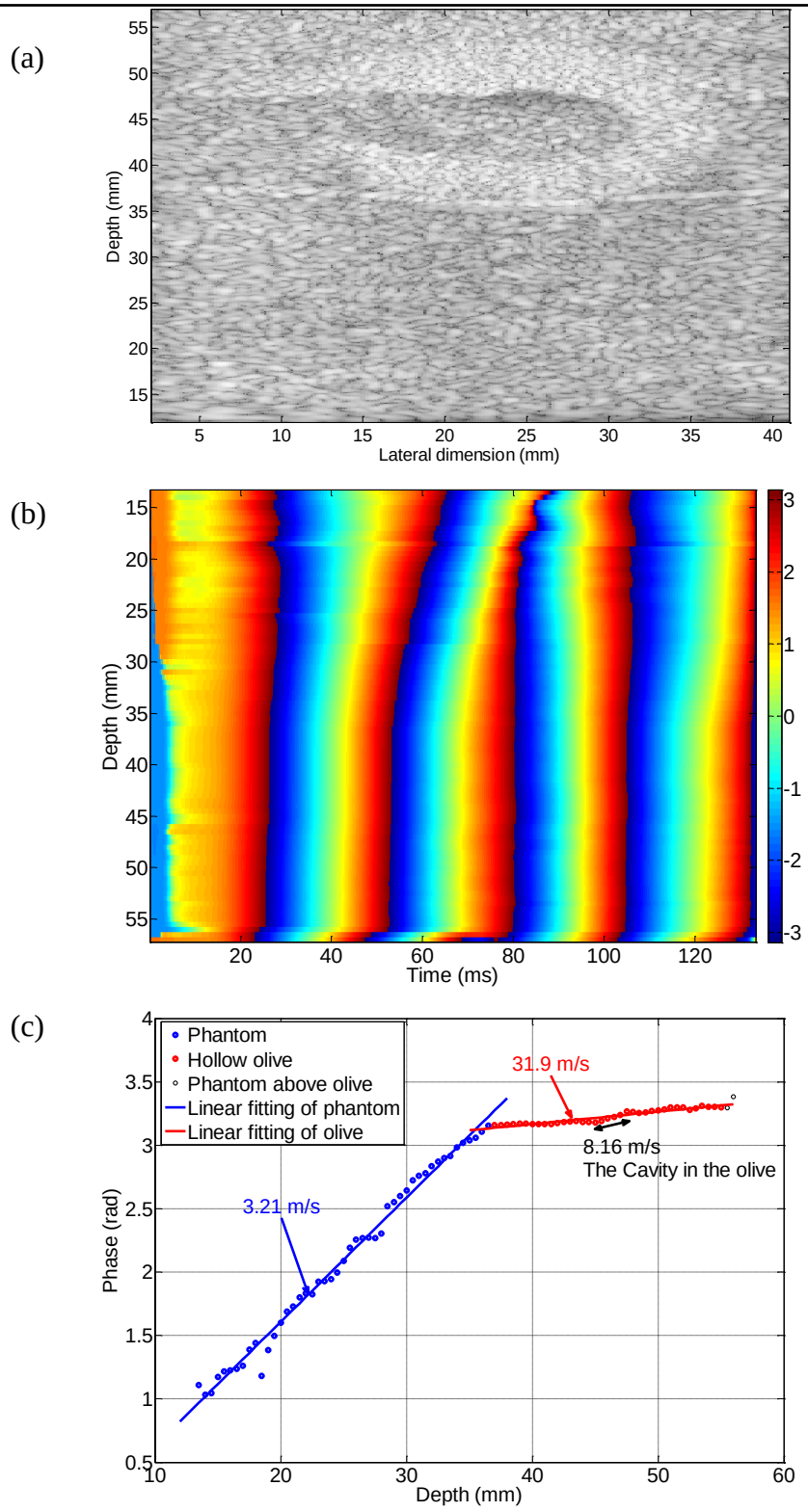

Figure 26. Hollow olive test in grape-olive phantom. (a) B-mode image; (b) phase map, the colorbar is with the unit of radians; (c) phase-depth plot and shear-wave velocity measurement.

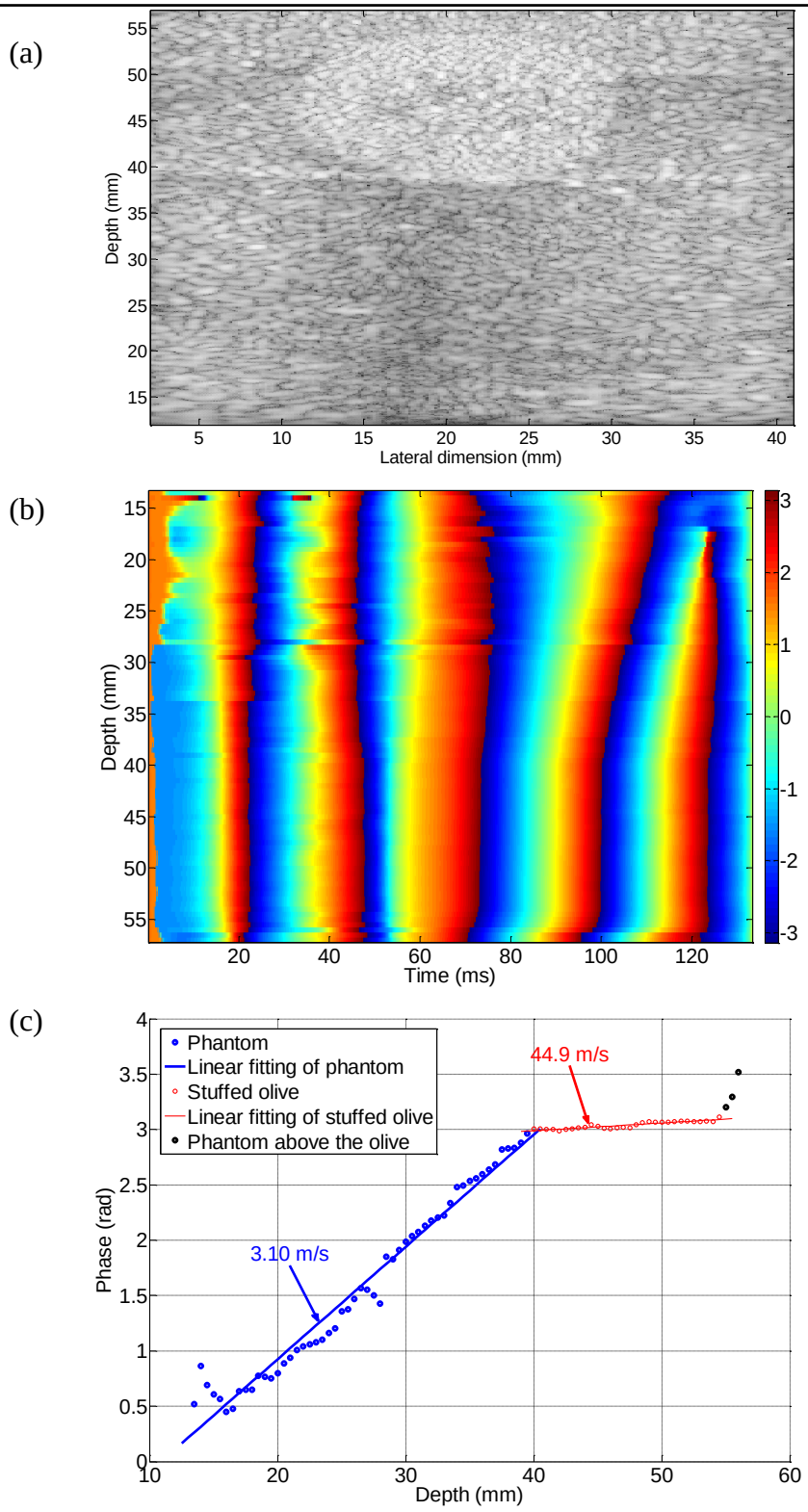

Figure 27. Stuffed olive test in grape-olive phantom. (a) B-mode image; (b) phase map, the colorbar is with the unit of radians; (c) phase-depth plot and shear-wave velocity measurement.

Bi-layer Phantom

Fig. 28 shows the B-mode image of the bi-layer phantom and the shear-wave speed image of this area. We can tell the boundary between the upper layer (5% gelatin phantom) and lower layer (10% gelatin phantom) in the B-mode image because of the acoustic impedance change. It is seen that the speckle pattern in both layers looks nearly identical. In the speed image, however, we can see obvious changes of shear-wave speed in the two layers and the boundary between the two speed areas corresponds well to the actual boundary in the B-mode image. The speed in the lower layer is greater than the speed in the upper layer, which means the lower layer phantom is stiffer than the upper layer phantom. This result agrees closely with the actual bi-layer structure. In addition, the shear-wave speed in lower layer (6 m/s on average) is approximately twice the speed in the upper layer (3 m/s on average), and the Young's modulus of lower layer (110 KPa on average) is around 4 times the modulus of upper layer (28 KPa on average). This is consistent with the elasticity relationship between the 5% and 10% phantom measured in Instron and ultrasound tests. Note that the bi-layer phantom was measured about 10 minutes after being taken out of the refrigerator, so the Young's moduli of both layers are greater than those measured by Instron machine and ultrasound tests in room temperature (the lower the temperature, the stiffer the phantom).

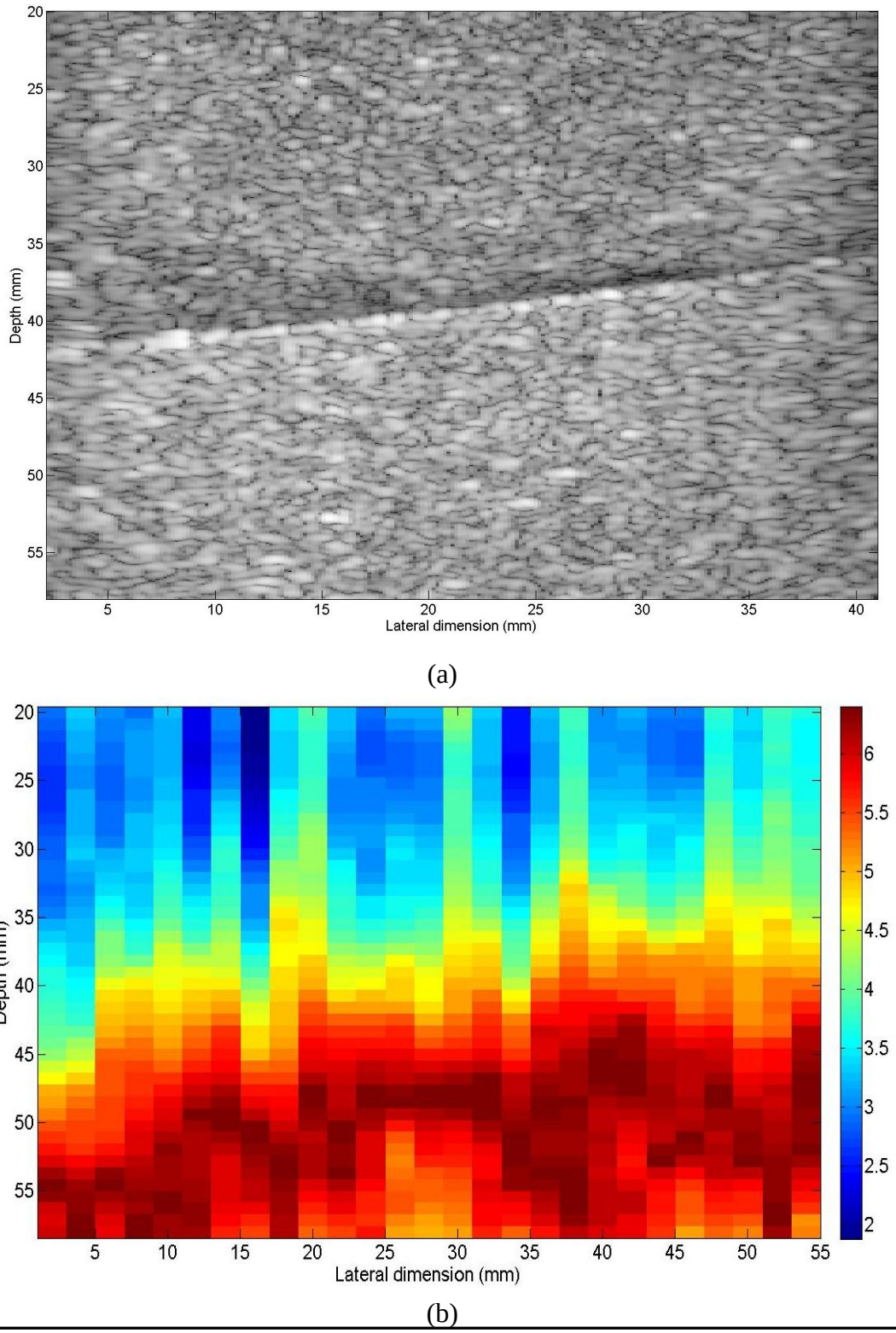

Figure 28. Bi-layer phantom test. (a) B-mode image: note that the speckle pattern in both layers is nearly identical; (b) Shear-wave speed image of the bi-layer phantom, the color bar is with the unit of m/s: note that stiffness in both layers is significantly different.

CHAPTER 4: BOVINE TENDON EXPERIMENTS

Introduction

In the feasibility experiments, ultrasound transient shear wave elasticity imaging shows potential of conducting comparative measurements of the Young's Modulus of a homogeneous phantom and indicating correct relative elasticity measurement of a heterogeneous material. Next, this method was performed on bovine tendon tissue to see the potential of this technique on tendon elasticity imaging in actual mammalian tissue. The purpose is to create an elastic mapping image which properly distinguishes the tendon from the normal gelatin phantom. The following sections introduce the details of making a tendon phantom and creating a speed image of the tendon.

Theory

The pathologic tendon presents a spatially random distribution of fibers oriented in the same direction as the tensile force (Bashford et al., 2008). This unique structure indicates the existence of a symmetry axis along the fibers (Gennisson et al., 2003). It has been shown (Zimmer and Cost, 1970) that this kind of symmetry corresponds to a hexagonal system (transverse isotropy) (Gennisson et al., 2003). The shear wave generated by the vibration piston source used in this project is assumed to be isotropic and symmetric in all directions. For the locally homogeneous material, e.g., the grape, olive and bi-layer phantom, the shear-wave speed correctly correlates to the shear modulus of the material in all directions; hence the correct shear modulus could be accurately estimated. However, for tendon tissue with significant shear modulus differences along and across the fiber, the

unpolarized shear wave propagates differently along the directions corresponding to the two different shear moduli. Thus, the measured shear modulus will be a combination of the along-fiber shear modulus and across-fiber shear modulus. Additionally, tendon tissue cannot be assumed to be incompressible (Poisson ratio = 0.5), so the Young's modulus can no longer be conveniently converted from shear modulus by multiplying by three. To summarize, the shear modulus measured in this tendon using the proposed method is the combination of the different shear moduli of the tendon; and the Young's modulus cannot be calculated as was done in the feasibility experiment.

Methods

Bovine Achilles tendons have a similar anatomical structure as the human Achilles tendon, being composed of collagen bundles aligned in the direction of tensile force. They are easier to acquire than human Achilles tendons. Therefore, we used bovine Achilles tendon to mimic human tendon in order to test the feasibility of proposed imaging method. Fresh bovine Achilles tendons were provided by J F O'Neill & Packing Co, Omaha, NE. Irrelevant muscles and membranes were excised and the main Achilles tendon was picked out as shown in Fig. 29. The cylinder shaped bovine tendon is about 10 cm long and 1.5 cm thick. The same procedures as in making the grape-olive phantom were used to make the bovine tendon phantom. The bovine tendon was placed in the middle of the phantom and closer to the side where the vibrator touches. Ultrasound B-mode images (Fig. 30) show the similar anatomical structure of bovine tendon and the human tendon, and show the reference area where the elasticity image will be mapped on.

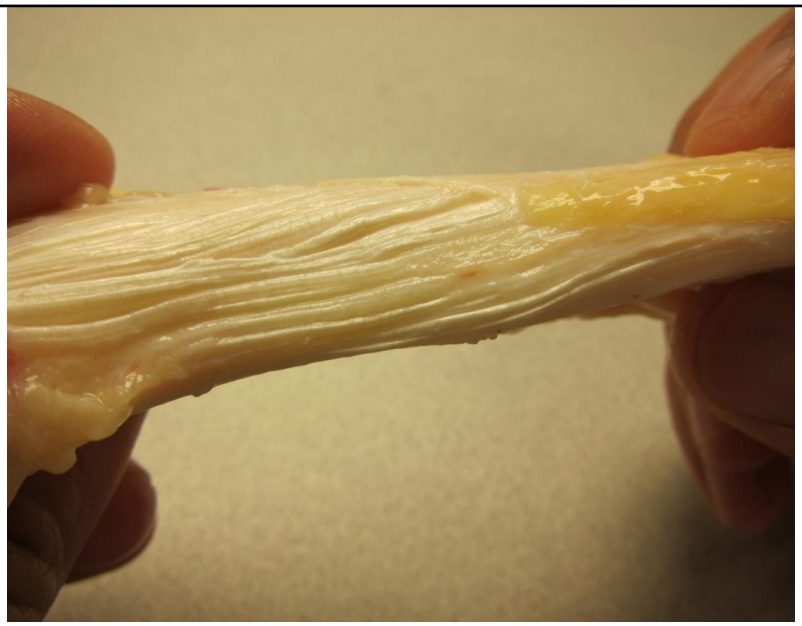

(a)

(b)

Figure 29. Bovine Achilles tendon preparation and bovine phantom making.

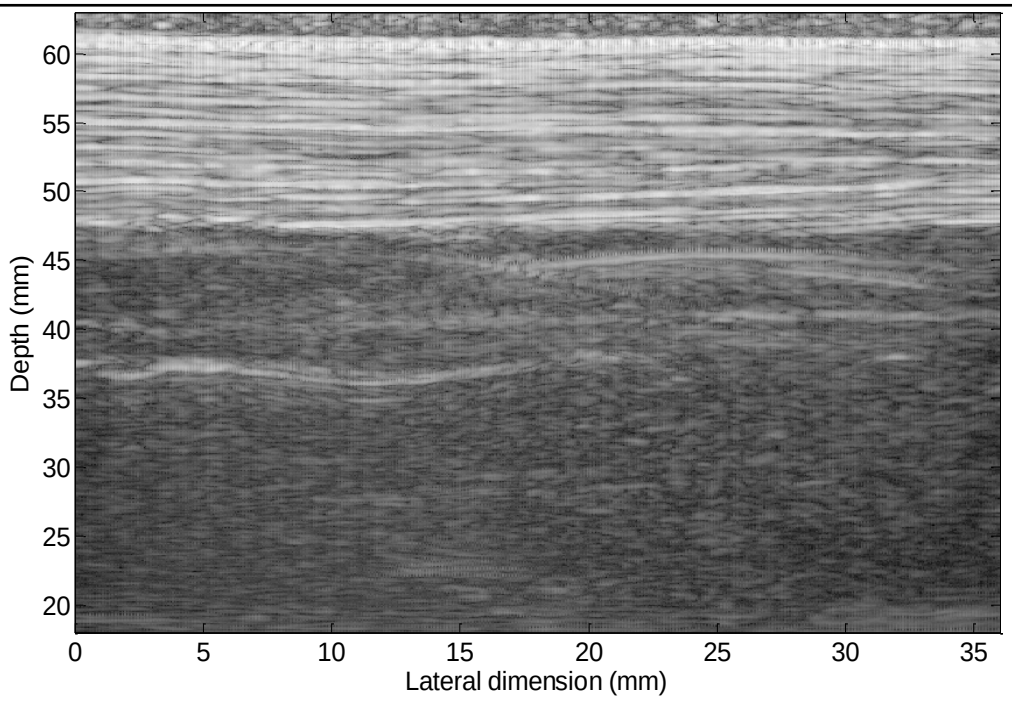

(a)

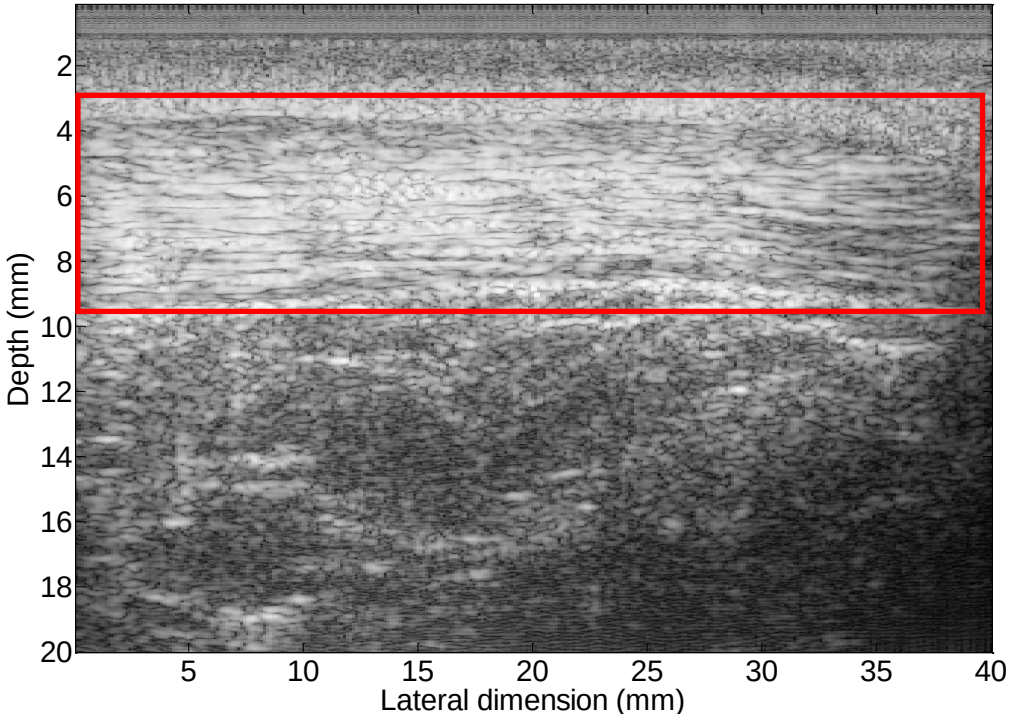

(b)

Figure 30. Ultrasound B-mode images of bovine Achilles tendon and human Achilles tendon. (a) bovine Achilles tendon; (b) human Achilles tendon with the tendon area in the red rectangular.

The same experimental set-up and procedures of creating the displacement field and measuring the shear-wave velocity as introduced in Chapter 3 were used here. In total, 17 sets of displacement data were taken 2 mm distance apart from each other (Fig. 31), with a total lateral acquisition dimension of 32 mm. The vibration was set to generate a 50 Hz sinusoid wave. The PRF was 1.5 KHz, with five times upsampling used in the displacement estimation algorithm.

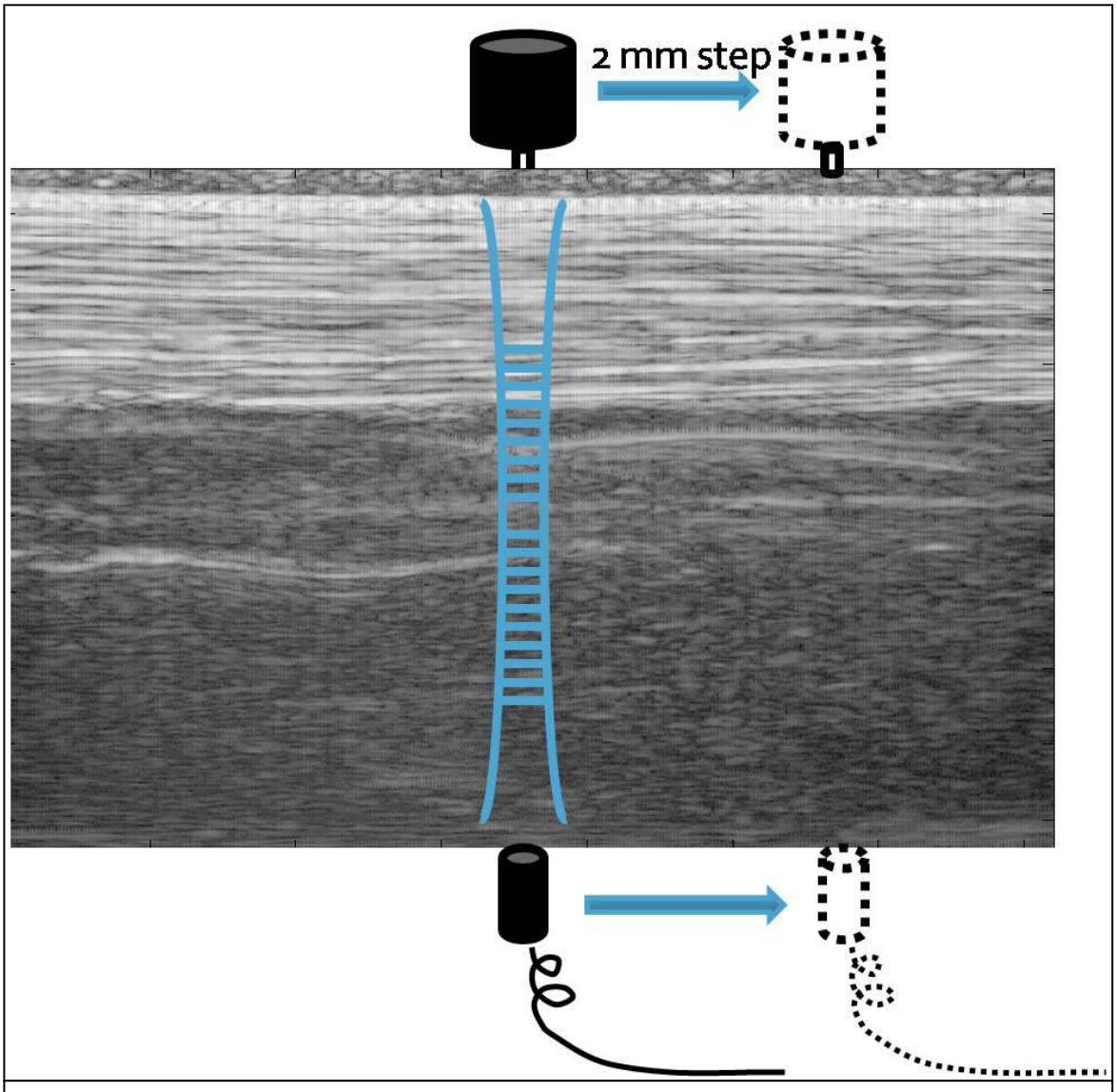

Figure 31. The transducer and vibrator moves coaxially with a 2mm step to create a 2D elasticity image of the phantom.

The local shear-wave velocity was estimated by taking linear fits at a local portion of the phase-depth gradient. Because the actual resolution of the elasticity map is 2 mm in the lateral dimension and 0.5 mm in the axial dimension while the B-mode image is much higher resolution in both dimensions, an interpolation was performed onto the elasticity image in order for better mapping. All elasticity mappings for tendon tissues use shear modulus instead of Young's modulus.

Results and Discussion

For each of the 17 displacement fields, spectral analysis was performed to estimate the phase gradient and then the shear-wave speed. One typical phase versus depth plot is as shown in Fig. 32. Similar to the grape-olive case, obvious phase speed changes can be seen in the tendon area, while the phase in the phantom area above the tendon was disorganized because of the attenuation loss of the echo signal. The shear wave change is about the same dimension as the tendon thickness and located at the same depth as shown in the B-mode image, which shows the correct positioning of the tendon. The shear-wave speed estimated from linear fitting is 7.97 m/s in the gelatin phantom (corresponding to a shear modulus of 66 KPa) and 79.4 m/s in the tendon tissue. The density of the tendon is found to be 1.06 g/cm^3 in the literature, so the calculated shear modulus of the tendon tissue is 6.67 MPa. Because the phantom was congealed and stored in the refrigerator to keep the tendon fresh, the measured phantom shear-wave speed is relatively greater than the previous value (refrigerated phantom is much stiffer than the normal phantom). As explained in the Theory section, the measured shear modulus of tendon here is actually a combination of the

shear moduli in all directions. Even so, the measured shear modulus clearly indicates the difference between the stiffness of a gelatin-phantom and a bovine Achilles tendon tissue.

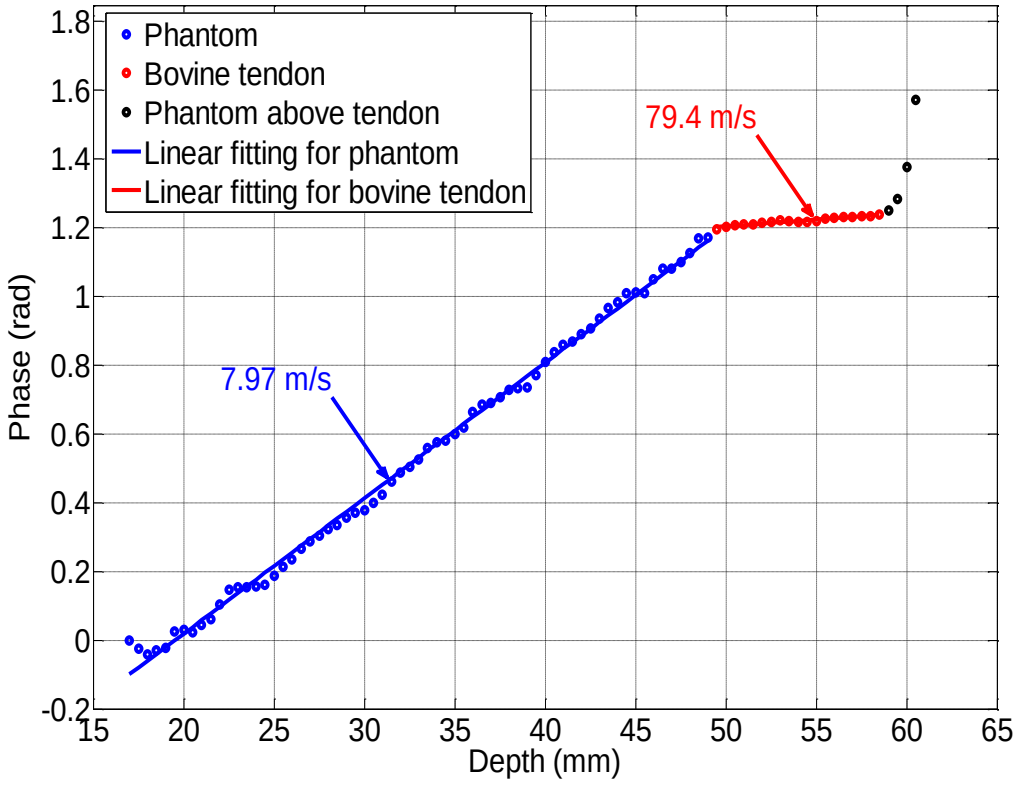

Figure 32. Phase versus depth plot of the bovine tendon phantom.

Fig. 33 shows the final shear-modulus mapping image (2-point linear fitting) and the original B-mode image. We can see that the shear modulus significantly changes in the tendon area, which corresponds to an increment of the tissue elasticity in the tendon. Compared to the normal shear modulus mapping of the gelatin phantom, the shear moduli within the tendon area present greater heterogeneity and poorer resolution of shear modulus distribution. One important reason resulting in the poor measurement resolution of tendon shear modulus is the limited axial dimension of the tendon. The number of phase

samples in Fig. 32 chosen to calculate the local shear-wave speed is a trade-off between axial image resolution and speed measurement accuracy. For instance, if 10 points were selected to calculate the phase gradient, more accurate speed estimates are obtained because a linear fitting of 10 points is more accurate than a linear fit of 2 points. However, the axial length covered by the samples required to estimate speed increases, leading to a loss of data at the interface between tendon and phantom, as shown in Fig. 34. If a 2-point step size is chosen, there will be much higher measurement resolution but the speed estimate will be poorer because the 2-point linear fitting can result in large biases, as shown in Fig. 33 (b).

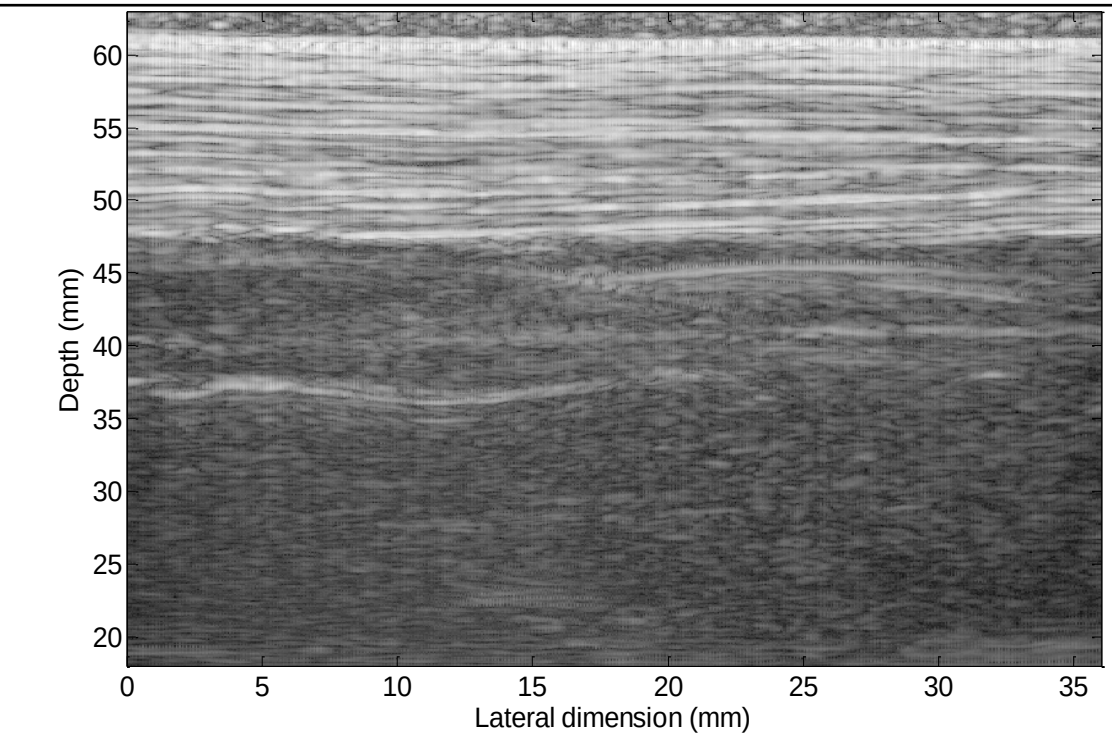

(a)

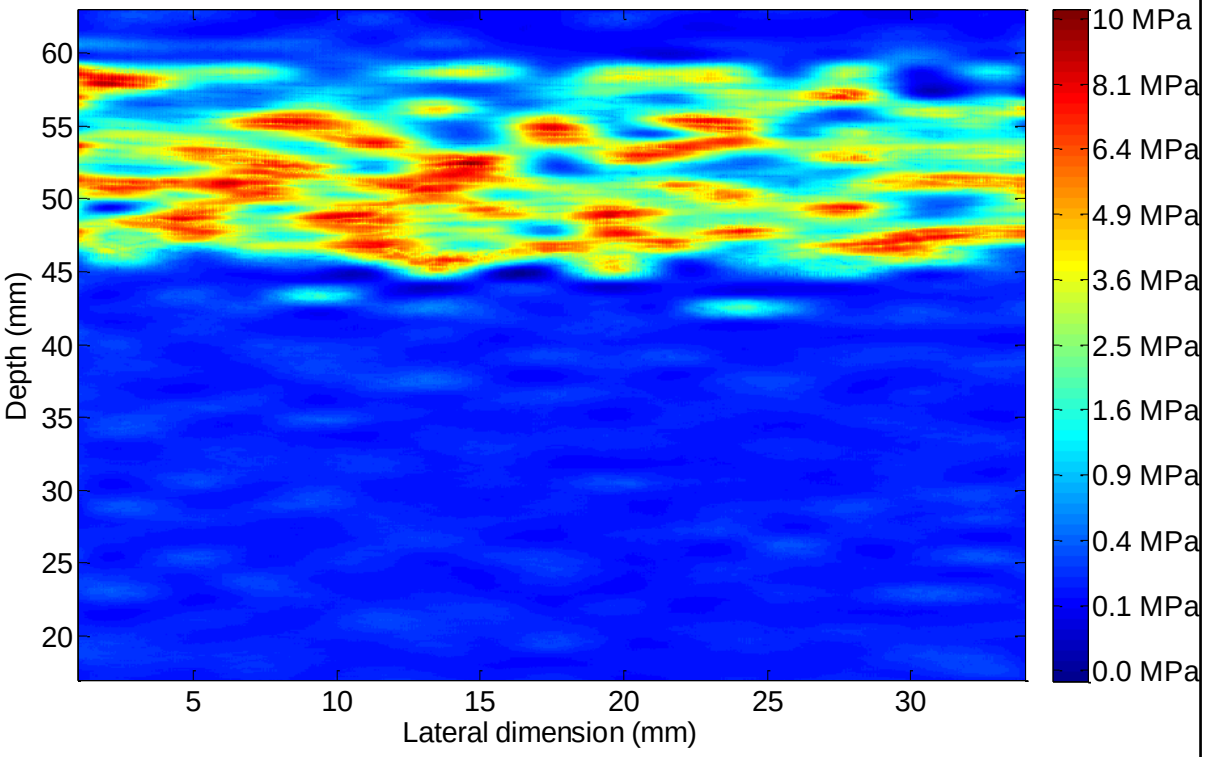

(b)

Figure 33. Shear-modulus mapping image (2-point linear fitting) of bovine tendon phantom ((b)) and the original ultrasound B-mode image ((a)).

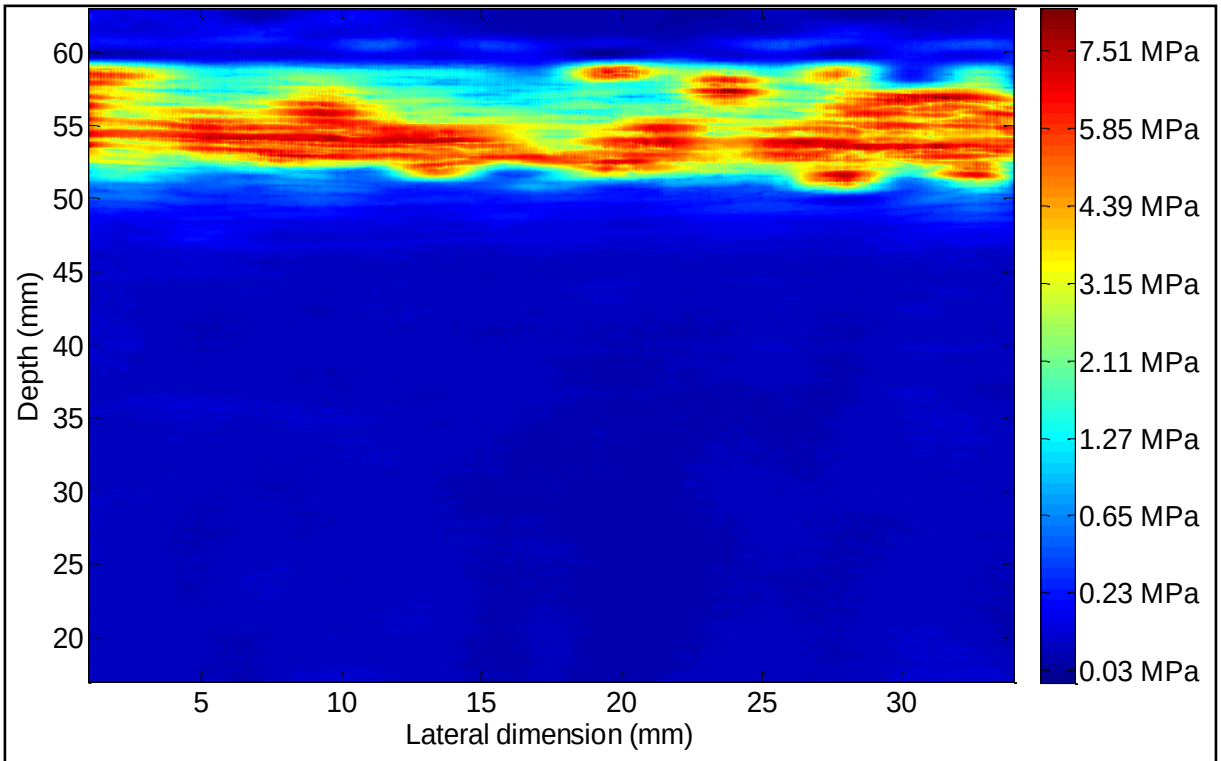

Figure 34. Shear-modulus mapping image of bovine tendon phantom generated by 10-point linear fitting.

Theoretically, the more lateral positions (shear wave A-lines) selected to collect displacement data, the better the lateral resolution of the shear modulus mapping image. However, for each displacement record taken from the shear wave A-line, it takes about 30 minutes for the computer (PC with Intel® Pentium® 4, CPU 3.20 GHz, 3.20 GHz) to finish all the data processing procedures shown in Fig. 17. For the 17 A-lines taken in the above experiment, it took about 9 hours to generate the shear modulus mapping image. Moreover, the overlapping kernels in the axial direction also affects the computational time. An overlap of fifty was consistently used in this project. However, with more computational power, a higher overlapping rate would give rise to better axial resolution of the shear modulus mapping image.

CHAPTER 5: SUMMARY AND SUGGESTED FUTURE WORK

Summary

Detection and diagnosis of early stage tendinopathy symptoms is critical for improving treatment interventions for individuals with tendinopathy. Tendinopathy can lead to tendon mechanical property changes at early stages. Unfortunately, no modern medical imaging systems can accurately image the local elasticity of tissue. Ultrasound transient shear wave elasticity imaging has been shown to be a promising tool of accurately measuring the elastic parameters of soft tissues and quantitatively mapping the elasticity information on diagnosing tissues. To date, however, this technique has not been used on tendinopathy diagnosis. Therefore, developing a clinically useful elasticity imaging platform could not only benefit individuals with tendinopathy with an earlier detection, intervention and better rehabilitation, but also provide a potential medical tool for quantifying musculoskeletal tissue dysfunction in other regions of the body such as the shoulder, elbow and knee.

This thesis has explained two series of experiments to show the procedures of:

- Designing and making an ultrasound transient shear wave elasticity imaging platform with proper supporting systems and accurate translating stages.
- Properly re-creating the ultrasound transient shear wave elasticity imaging methodology with Green's function simulation as the verification.
- Designing protocols of making high-quality tissue-mimicking phantoms (homogeneous phantom, heterogeneous phantom and bovine tendon phantom)

with recommended acoustic properties as soft tissues.

- Verifying the accuracy of the quantitative measurements of the tissue Young's modulus, realizing quantitative elasticity mapping of heterogeneous tissue.
- Implementing the ultrasound transient shear wave elasticity imaging method on bovine Achilles tendon phantoms for feasibility tests.

The results of the experiments demonstrate the feasibility of the usage of the proposed methodology for tendon tissue elasticity imaging, and indicate great potential for tendinopathy diagnosis.

Suggested Future Work

One suggested future direction is to improve the experimental elasticity imaging system constructed here. To better accommodate *in vivo* elasticity imaging, a 1D transient elasticity probe should be made with a single element transducer mounted on the surface of the vibrator, so that the transducer surface could act as the vibration piston with pulse-echo mode on (Sandrin et al., 2002).

Another suggestion would be to alter the elasticity measurement setup so that it can perform polarized measurements. It has been shown that a low frequency polarized shear strain wave can be generated by a rod source, which allows the study of an anisotropic medium such as muscle (Gennisson et al., 2003). Gennisson et al. demonstrated that when the vibration rod is parallel to the muscle fibers, the speed of the generated shear wave with a polarization perpendicular to the fibers is obtained; and when the rod is set perpendicular to the fibers, the speed of the shear wave with a polarization parallel to the fibers is

obtained (Gennisson et al., 2003). Consequently, the shear modulus along the muscle fibers and across the muscle fibers can be accurately measured respectively by setting the rod perpendicular and parallel to the muscle fibers (Gennisson et al., 2003). Tendon tissue has similar structure as muscle, so Gennisson's method may have the same elasticity measurement capability on tendon tissue. By setting the rod perpendicular to the tendon collagen bundles, the shear modulus along the fibers, which is also the modulus related to tendinopathy degeneration, may be estimated and a shear modulus mapping image created.

Meanwhile, steps need to be taken to accelerate the data processing procedures for future *in vivo* elasticity imaging. For example, extracting and processing only the shear wave displacement area from the displacement field could significantly accelerate the data processing speed. Also, optimizing the data processing programs could also help improve the processing speed.

Another recommendation is to design a protocol of making a better tendon-tissue-mimicking phantom with similar human tendinopathy symptoms. A histologically accurate way of locally disorganizing normal bovine Achilles tendon tissue should be developed so that better feasibility experiments could be conducted before experiments are performed on human Achilles tendons. For example, a laser beam could be used to alter tendon tissue, or High Intensity Focused Ultrasound (HIFU) could create a thermal effect on deep tissue without damaging superficial tissues, thus altering the collagen organization inside the tendon (Kulig and Bashford, personal communication, 2010).

REFERENCES

American Institute of ultrasound in Medicine. "Acoustic output measurement and labeling standard for diagnostic ultrasound equipment." Laurel, MD: AIUM, 1992.

Bashford, G. R., Tomsen, N., Arya, S., Burnfield, J. M. and Kulig, K, "Tendinopathy Discrimination by Use of Spatial Frequency Parameters in Ultrasound B-Mode Images", *IEEE Transactions on Medical Imaging*, vol. 27, no. 5, pp. 608 – 615, May 2008.

Bercoff, J., Tanter, M. and Fink, M., "Supersonic shear imaging: A new technique for soft tissue elasticity mapping", *IEEE Transactions on Ultrasonics, Ferroelectrics, and Frequency Control*, vol. 51, no. 4, pp. 396 – 409, Apr. 2004.

Bleakney, R. R., Tallon, C., Wong, J. K., Lim, K. P. and Maffulli, N., "Long-term ultrasonographic features of the Achilles tendon after rupture", *Clinical Journal of Sport Medcine*, vol. 12, no. 5, pp. 273 – 278, 2002.

Bohs, L. N. and Trahey, G. E., "A novel method for angle independent ultrasonic imaging of blood flow and tissue motion", *IEEE Transactions on Biomedical Engineering*, vol. 38, no. 3, 280 – 286, 1991.

Bude, R. O. and Adler, R. S., "An easily made, low-cost, tissue-like ultrasound phantom material", *Journal of Clinical Ultrasound*, 23:271 – 273, May 1995.

Carstensen, E. L., Parker, K. J. and Lerner, R. M., "Elastography in the management of liver disease", *Ultrasound in Medicine and Biology*, vol. 34, no. 10, 1535 – 1546, 2008.

Catheline, S., Thomas, J., Wu, F. and Fink, M. A., "Diffraction field of a low frequency vibrator in soft tissues using transient elastography", *IEEE Transactions on Ultrasonics, Ferroelectrics, and Frequency Control*, vol. 46, no. 4, 1013 – 1019, July 1999a.

Catheline, S., Wu, F. and Fink, M. A., "A solution to diffraction biases in sonoelasticity: The acoustic impulse technique", *The Journal of the Acoustical Society of America*, vol. 105, 2941 – 2950, 1999b.

Centers for Disease Control (CDC) website, "US obesity trends 1985 – 2007", http://www.cdc.gov/nccdphp/dnpa/obesity/trend/maps/index.htm, accessed 4/18/2009.

Dutt, V., Kinnick, R. R. and Greenleaf, J. F., "Acoustic shear wave displacement measurement using ultrasound", *Proceedings of IEEE Ultrasonics Symposium*, vol. 2, pp. 1185 – 1193, 1996.

Farron, J., Varghese, T. and Thelen, D. G., "Measurement of tendon strain during muscle twitch contractions using ultrasound elastography", *IEEE Transactions on Ultrasonics, Ferroelectrics, and Frequency Control*, vol. 56, no. 1, pp. 27 – 35, Jan. 2009.

Gakenheimer, D. C. and Miklowitz, J., "Transient excitation of a half space by a point load traveling on the surface", *Journal of Applied Mechanics*, vol. 36, 505-514, 1969.

Gennisson, J. L., Catheline, S., Chaffai, S. and Fink, M. A., "Transient elastography in anisotropic medium: Application to the measurement of slow and fast shear wave speeds in muscles", *The Journal of the Acoustical Society of America*, vol. 114, 536 – 541, 2003.

Graff, K. F., *Wave Motion in Elastic Solids*. Columbus, OH: Ohio State University Press, 1975.

Greenleaf, J. F., Fatemi, M. and Insana, M., "Selected methods for imaging elastic properties of biological tissues", *Annual Review of Biomedical Engineering*, vol. 5, 57 – 78, 2003.

Ito, M., Kawakami, Y., Ichinose, Y., Fukashiro, S. and Fukunaga, T., "Nonisometric behavior of fascicles during isometric contractions of a human muscle", *Journal of Applied Physiology*, vol. 85, no. 4, pp. 1230 – 1235, 1998.

Kurokawa, S., Fukunaga, T., Nagano, A. and Fukashiro, S., "Interaction between fascicles and tendinous structures during counter movement jumping investigated *in vivo*", *Journal of Applied Physiology*, vol. 95, no. 6, pp. 2306 – 2314, 2003.

Latash, M. L. and Zatsiorsky V. M., "Joint stiffness: Myth or reality?", *Human Movement Science*, vol. 12, pp. 653 – 692, 1993.

Levinson, S. F., Shinagawa, M. and Sato, T., "Sonoelastic determination of human skeletal muscle elasticity", *Journal of Biomechanics*, vol. 28, no. 10, pp. 1145 – 1154, 1995.

Madsen, E. L., Frank, G. R. and Dong, F., "Liquid or solid ultrasonically tissue-mimicking materials with very low scatter", *Ultrasound in Medicine and Biology*, vol. 24, no. 4, 535 – 542, 1998.

Maganaris, C. N. and Paul, J. P., "Load-elongation characteristics of *in vivo* human tendon and aponeurosis", *The Journal of Experimental Biology*, vol. 203, pt. 4, pp. 751 – 756, 2000a.

Maganaris, C. N., "Tensile properties for *in vivo* human tendinous tissue", *Journal of Biomechanics*, vol. 35, no. 8, pp. 1019 – 1027, 2002.

Maganaris, C. N. and Paul, J. P., "*In vivo* human tendinous tissue stretch upon maximum muscle force generation", *Journal of Biomechanics*, vol. 33, no. 11, pp. 1453 – 1459, 2000b.

McQueen, F., Beckley, V., Crabbe, J., Robinson, E., Yeoman, S. and Stewart, N., "Magnetic resonance imaging evidence of tendinopathy in early rheumatoid arthritis predicts tendon rupture at six years", *Arthritis & Rheumatism*, vol. 52, no. 3, pp. 744 – 751, Mar. 2005.

Muller, M., Gennisson, J. L., Deffieux, T., Tanter, M. and Fink, M., "Quantitative viscoelasticity mapping of human liver using supersonic shear imaging: Preliminary *in vivo* feasibility study", *Ultrasound in Medicine and Biology*, vol. 35, no. 2, pp. 219 – 229, 2009.

Oestreicher, H. L., "Field and impedance of an oscillating sphere in a viscoelastic medium with an application to biophysics", *The Journal of the Acoustical Society of America*, vol. 23, 707 – 714, 1951.

Ofer, N., Akselrod, S., Nyska, M., Werner, M., Glaser, E. and Shabat, S., "Motion-based tendon diagnosis using sequence processing of ultrasound images", *Journal of Orthopaedic Research*, vol. 22, no. 6, pp. 1296 – 1302, 2004.

Ophir, J., Cespedes, I., Ponnekanti, H., Yazdi, Y. and Li, X., "Elastography: A quantitative method for imaging the elasticity of biological tissues", *Ultrasound Imaging*, vol. 13, 111 – 134, 1991.

Pollard, H. F., *Sound Wave in Solid*, Pion Limited, London, 1977, pp. 206.

Pomeranz, Y., *Functional Properties of Food Components*, Academic Press, Orlando, pp. 39 – 61, 1985.

Sandrin, L., Tanter, M., Gennisson, J. L., Catheline, S. and Fink, M. A., "Shear elasticity probe for soft tissues with 1-D transient elastography", *IEEE Transactions on Ultrasonics, Ferroelectrics, and Frequency control*, vol. 49, no. 4, 436 – 446, 2002.

Scott, A. and Ashe, M. C., "Common tendinopathies in the upper and lower extremities", *Current Sports Medicine Reports*, vol. 5(5), pp. 233 – 241, 2006.

Scruby, C. B. and Drain, L. E., *Laser Ultrasonics*, New York: Adam Hilger, 223 – 324, 1990.

Selfridge, A. R., "Approximate material properties in isotropic materials", *IEEE Transactions on Sonics and Ultrasonics*, vol. SU-32, no. 3, May 1985.

Silver, F. H., Freeman, J. W. and Seehra, G. P., "Collagen self-assembly and the development of tendon mechanical properties", *Journal of Biomechanics*, vol. 36, pp. 1529 – 1553, 2003.

Song, P., Linstrom, K. R., Boye, A. J., Kulig, K., Burnfield, J. M. and Bashford, G. R., "Tendinopathy Discrimination Using Spatial Frequency Parameters and Artificial Neural Networks", *IEEE International Ultrasonics Symposium Proceedings*, pp. 1902 – 1905, 2009.

Stroshine, R. and Hamann, D., *Physical Properties of Agricultural Materials and Food Products*, Copyright by Richard Stroshine, 1994, pp. 83 – 87.

Tanter, M., Touboul, D., Gennisson, J. L., Bercoff, J. and Fink, M. A., "High-resolution quantitative imaging of cornea elasticity using supersonic shear imaging", *IEEE Transactions on Medical Imaging*, vol. 28, no. 12, 1881 – 1893, 2009.

Telford, I. R. and Bridgman, C. F., "Connective tissue I-cells and fibers," in *Introduction to Functional Histology*, 1st ed. New York: Harper Collins, 1995, pp. 79 – 98.

Viola, F. and Walker, W. F., "A spline-based algorithms for continuous time-delay estimation using samples data", *IEEE Transactions on Ultrasonics, Ferroelectrics, and Frequency control*, vol. 52, no. 1, 80 – 93, 2005

Walker, W. F. and Trahey, G. E., "A fundamental limit on the performance of correlation based phase correlation and flow estimation techniques", *IEEE Transactions on Ultrasonics, Ferroelectrics, and Frequency control*, vol. 41, no. 5, 644 – 654, 1994.

Zimmer, J. E. and Cost, j. R., "Determination of the elastic constants of an unidirectional fiber composite using ultrasonic velocity measurements", *Journal of Acoustical Society of America*, vol. 47, pp. 795 – 803, 1970.

APPENDICES

Appendix A: Green's Function

Catheline et al. (Catheline et al., 1999b) summarized the Green's function calculated by Gakenheimer and Miklovitz (Gakenheimer and Miklovitz, 1969). Here we cite the "Appendix A" and "Appendix B" from Catheline et al., 1999b as below (Catheline et al., 1999b):

The Green's function exactly described the displacement field of a point source traveling on a surface of a semi-infinite elastic isotropic solid. "The solution corresponding to normal displacements induced by a motionless point source with a pulsed time dependence at the epicenter is presented here:

$$G_{ZZ}^{0} = G_{ZZ}^{S} + G_{ZZ}^{P},$$

$$G_{ZZ}^{S} = -\frac{C_P}{\pi\mu z^2}\frac{\partial}{\partial t}\left[Y(t-t_s)t\frac{k_2^S k_3^S}{k_5^S}\right],$$

$$G_{ZZ}^{P} = \frac{C_P}{2\pi\mu z^2}\frac{\partial}{\partial t}\left[Y(t-t_P)t\frac{k_1^P k_3^P}{k_5^P}\right],$$

$$\begin{cases} k_1^S = \gamma^2\left(\frac{2t^2}{t_S^2}-1\right), \\ k_2^S = \gamma^2\left(\frac{t^2}{t_S^2}-1\right), \\ k_3^S = \sqrt{\gamma^2\left(\frac{t^2}{t_S^2}-1\right)+1}, \\ k_4^S = \gamma\frac{t}{t_S}, \\ k_5^S = {k_1^S}^2 - 4k_2^S k_3^S k_4^S, \end{cases}$$

$$\begin{cases} k_1^P = \left(\frac{2t^2}{t_P^2}-1\right)+\gamma^2, \\ k_2^P = \left(\frac{t^2}{t_P^2}-1\right), \\ k_3^P = \frac{t}{t_P}, \\ k_4^P = \sqrt{\frac{t^2}{t_P^2}-1+\gamma^2}, \\ k_5^P = {k_1^P}^2 - 4k_2^P k_3^P k_4^P, \end{cases}$$

where C_P is the compressional wave velocity, z is the depth along the axis of the point source, μ is the Lamé coefficient of shear elasticity, $Y(t\text{-}t_i)$ is the Heaviside function, t_S is the arrival time of the shear wave, t_P is the arrival time of the compressional wave, and $\gamma = C_P/C_S$.

From Green's function obtained at the epicenter of a semi-infinite elastic solid for a

pulsed time excitation, approximations of the normal displacements around the arrival time of the shear and compressional wave are calculated here.

$$For\ t{\sim}t_P:$$

$$G_{ZZ}^{P} \approx \frac{C_P}{2\pi\mu z^2}\left[\frac{\delta(t-t_P)t}{\gamma^2}+\frac{Y(t-t_P)}{\gamma^2}\right].$$

$$For\ t{\sim}t_S:$$

$$G_{ZZ}^{S} \approx -\frac{C_P}{\pi\mu z^2}\left[\frac{2Y(t-t_S)}{\gamma^2}\right].$$

$$For\ t \gg t_S \gg t_P\ (far\ from\ the\ arrival\ time):$$

$$G_{ZZ}^{P} \approx \frac{C_P}{2\pi\mu z^2}\left[\frac{2Y(t-t_P)t}{\gamma^2 t_P}\right],$$

$$G_{ZZ}^{S} \approx -\frac{C_P}{\pi\mu z^2}\left[\frac{Y(t-t_S)t}{\gamma^2 t_P}\right].$$

So the approximate expression is:

$$G_{ZZ} \approx \frac{C_P}{2\pi\mu z^2}\left[\frac{\delta(t-t_P)t}{\gamma^2}+[Y(t-t_P)-Y(t-t_S)]\frac{2t}{\gamma^2 t_P}-4\frac{Y(t-t_S)}{\gamma^2}+\frac{Y(t-t_P)}{\gamma^2}\right].$$

As far as normal velocity of displacement is concerned, we finally obtain:

$$\frac{\partial G_{ZZ}}{\partial t} \approx \frac{C_P}{2\pi\mu z^2}\left\{\delta'(t-t_P)\frac{t}{\gamma^2}+[Y(t-t_P)-Y(t-t_S)]\frac{2t}{\gamma^2 t_P}-4\frac{\delta(t-t_S)}{\gamma^2}+\frac{\delta(t-t_P)}{\gamma^2}+\right.$$

$$\left.[\delta(t-t_P)-\delta(t-t_S)]\frac{2t}{\gamma^2 t_P}\right\}$$

" (Catheline et al., 1999b).

Appendix B: Spline-based Displacement Estimation Algorithms

Here we cite the detailed spline-based displacement estimation algorithms proposed by Viola and Walker (Viola and Walker, 2005):

"Two discretely sampled A-line signals *A* and *B* are denoted as:

$$A[n] = A(n \cdot \partial), \tag{B1}$$

$$B[n] = B(n \cdot \partial), \tag{B2}$$

where $A[n]$ and $B[n]$ are found by taking samples from the continuous time signals $A(t)$ and $B(t)$ at a sampling interval of ∂, and with lengths N and M, respectively, where $M < N$. $A[n]$, the reference signal, is processed to determine an analytical representation of the signal, $\underline{A}[n]$. The cubic splines were used as the analytic representation of $A[n]$ and the piecewise continuous polynomial representation of the signal can be expressed as

$$\underline{A}(t) = \begin{cases} \partial \le t < 2 \cdot \partial & f_1(t) = a_1 t^3 + b_1 t^2 + c_1 t + d_1 \\ i \cdot \partial \le t < (i+1) \cdot \partial & f_i(t) = a_i t^3 + b_i t^2 + c_i t + d_i \\ (N-1) \cdot \partial \le t < N \cdot \partial & f_{N-1}(t) = a_{N-1} t^3 + b_{N-1} t^2 + c_{N-1} t + d_{N-1} \end{cases} \tag{B3}$$

The sum squared error (SSE) method was used to estimate the time delay between the two signals:

$$\varepsilon(t) = \sum_{i=1}^{M} (\underline{A}(i\partial + t) - B[i])^2 = \sum_{i=1}^{M} (f_i(t) - B[i])^2 \tag{B4}$$

The value of *t* that minimizes the SSE, ε(t), can be found analytically by taking the derivative with respect to *t*, setting the result equal to zero, and solving for *t*. Taking the derivative of ε(t) with respect to *t* yields:

$$\frac{d\varepsilon(t)}{dt} = \sum_{i=1}^{M} 2 f_i(t) \frac{df_i(t)}{dt} + 2B[i] \frac{dB[i]}{dt} - 2 f_i(t) \frac{dB[i]}{dt} - 2B[i] \frac{df_i(t)}{dt}. \tag{B5}$$

Because the sample points $B[i]$ have no dependence on *t*, their derivatives with respect to *t* are zero. The expression in Eqn. (B5) thus can be simplified to:

$$\frac{d\varepsilon(t)}{dt} = \sum_{i=1}^{M} \left(2 f_i(t) \frac{df_i(t)}{dt} - 2B[i] \frac{df_i(t)}{dt} \right). \tag{B6}$$

Expanding this expression by substituting in Eqn. (B3) yields:

$$\frac{d\varepsilon(t)}{dt} = t^5 \sum_{i=1}^{M} 6a_i^2 + t^4 \sum_{i=1}^{M} 10 a_i b_i + t^3 \sum_{i=1}^{M} (8 a_i c_i + 4 b_i^2) + t^2 \sum_{i=1}^{M} (6 a_i d_i + 6 b_i c_i - 6 a_i B[i]) + t \sum_{i=1}^{M} (4 b_i d_i + 2 c_i^2 - 4 b_i B[i]) + \sum_{i=1}^{M} (2 c_i d_i - 2 c_i B[i]). \tag{B7}$$

Among the five roots of Eqn. (B7), the real one that minimizes the error (t) is chosen to be the local time delay estimate. And this estimate was shown by the authors to have relatively low bias and variance, even when the true delay lies outside the sample interval examined" (Viola and Walker, 2005).

Appendix C: Tissue-mimicking Phantom Making Procedures

The procedures of making the gelatin-Metamucil phantom used in this project are as below (Chen, personal communication, 2010):

a. Spray PAM® oil (original) evenly onto the interior walls of the container, leave the container in room temperature until all the oil spread out without forming droplets or streaks (Fig. C1).

(a)

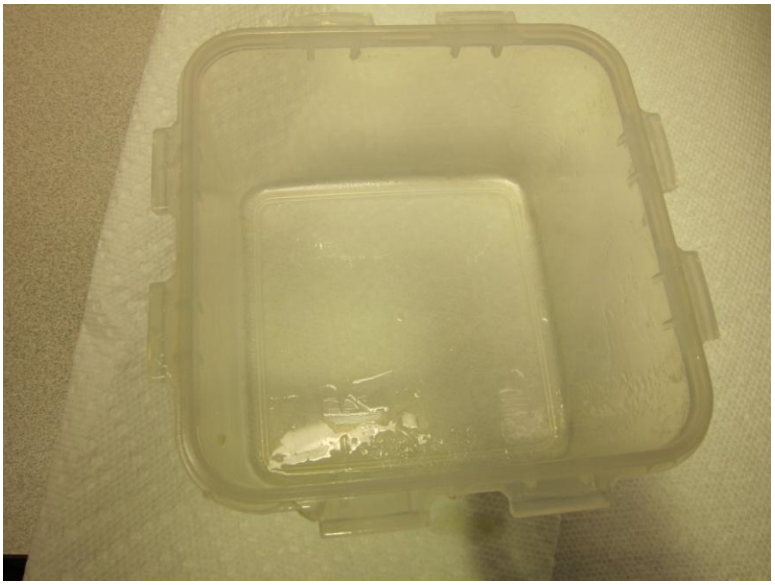

(b)

Figure C1. (a) Spray PAM oil evenly onto the interior walls of the container; (b) Leave the container in room temperature until all the oil spread out.

b. Add 50 ml 1-propanol (preserve the phantom from bacteria) into 700 ml distilled water, and then add 100 ml gelatin powder to the propanol-water mixture in room temperature. Stir well all the time (Fig. C2).

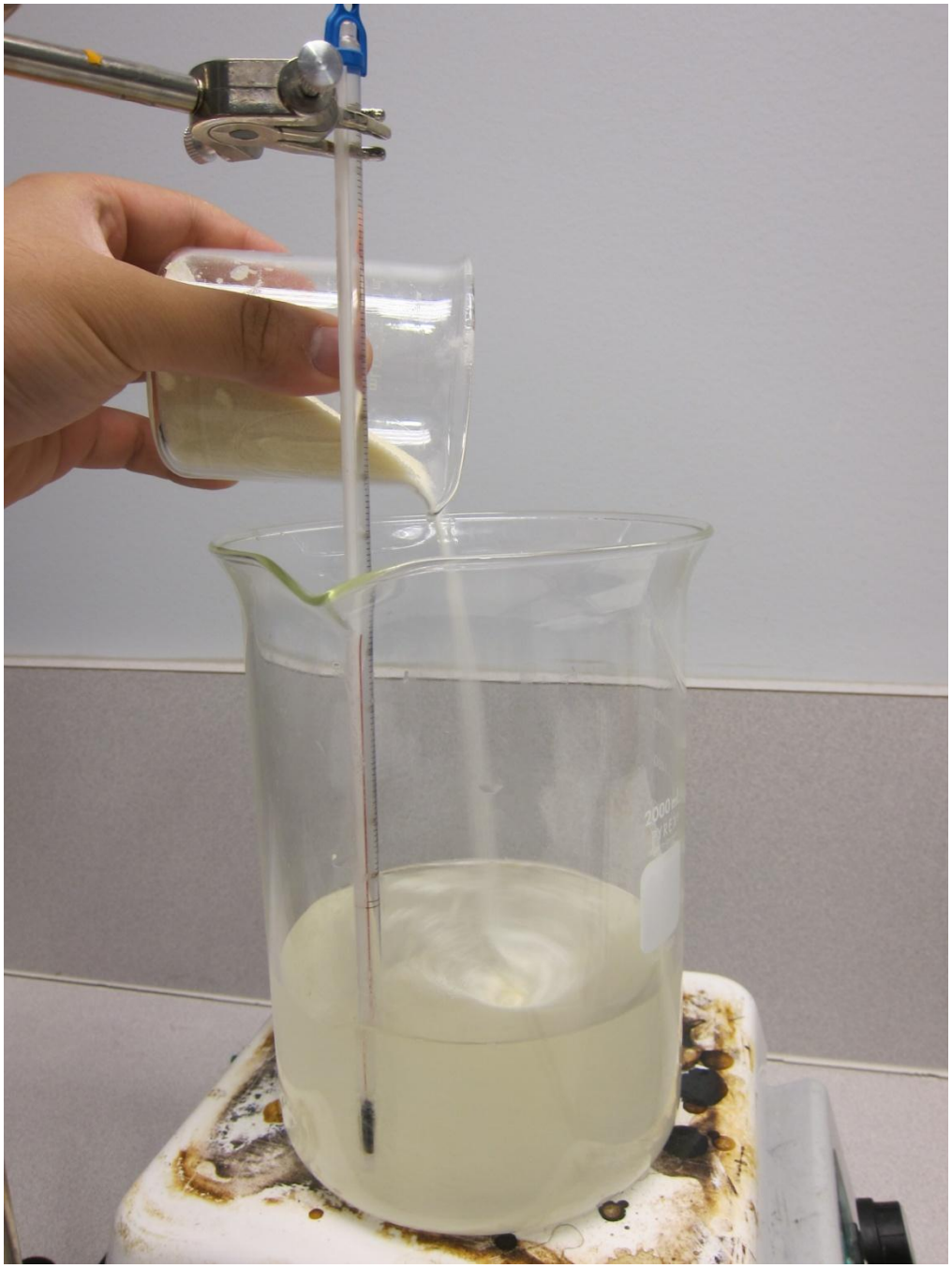

Figure C2. Slowly add the gelatin powder into the propanol-water mixture in room temperature and stir well all the time.

c. Heat the solution from “b” to around 45 Celsius degree with stirring, at this time the gelatin powder should be well dissolved without clotting. Turn off the heating (with stirring still on) and add in 120 ml (about 10% of the total volume) glycerol, which will make the phantom more durable (Fig. C3).

Figure C3. Slowly add in 120 ml glycerol and stir well all the time.

d. Add 25 grams Metamucil powder (sugar-free, smooth texture, unflavored) into 500 ml distilled water in room temperature, and quickly stir the solution for about 1 minute (Fig. C4).

Figure C4. Slowly add 25 grams of Metamucil powder into 500 ml distilled water in room temperature and quickly stir the solution for about 1 minute.

e. Add “d” into “c” through a fine strainer slowly, with stirring on all the same time (Fig. C5).

Figure C5. Add “d” into “c” through a strainer slowly and stir well all the same time.

f. Degas the well mixed solution with a vacuum and remove bubbles on the surface (Fig. C6).

Figure C6. Degas the well mixed solution with a vacuum. Wait (about 15 minutes) until no tiny bubbles can be seen in the solution.

g. Put the oil sprayed container into a water bath with room temperature, and then add the solution from “f” into the container through a glass rod or rubber spatula slowly to avoid making bubbles (Fig. C7). Fill the container until the liquid overflows (Fig. C8).

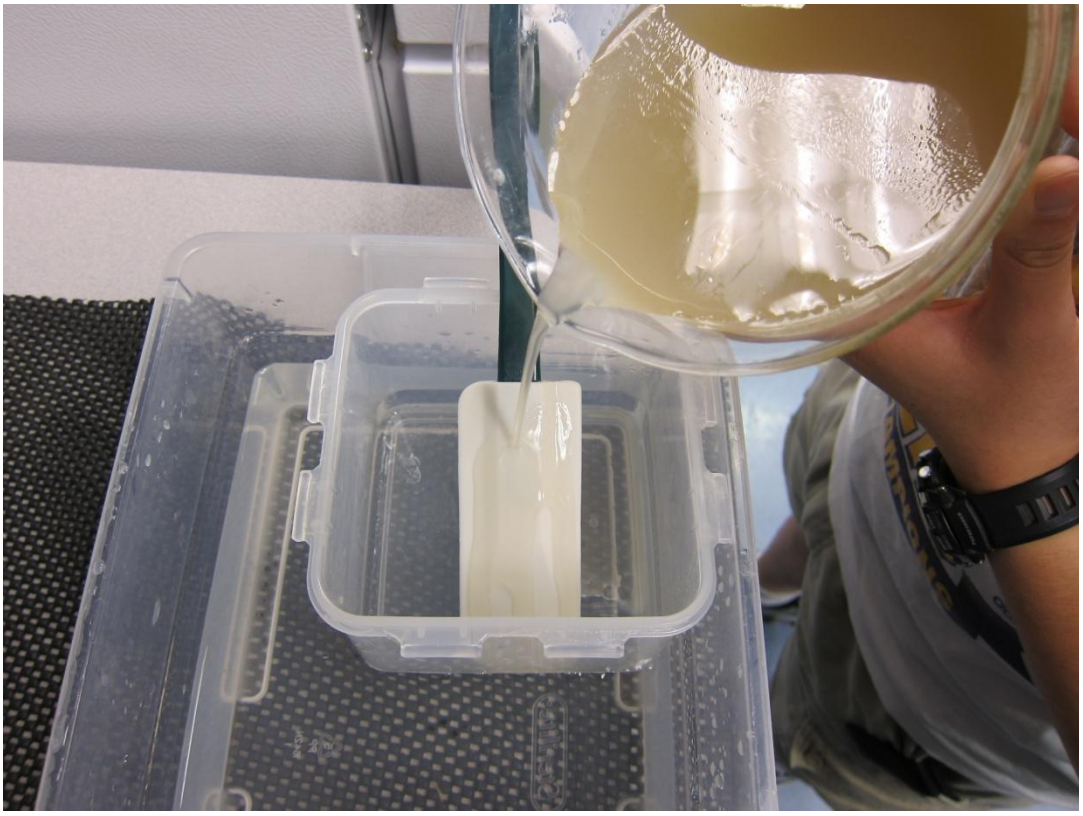

Figure C7. Slowly pour the solution through a rubber spatula into the oil-sprayed container, with the container in a water bath in room temperature.

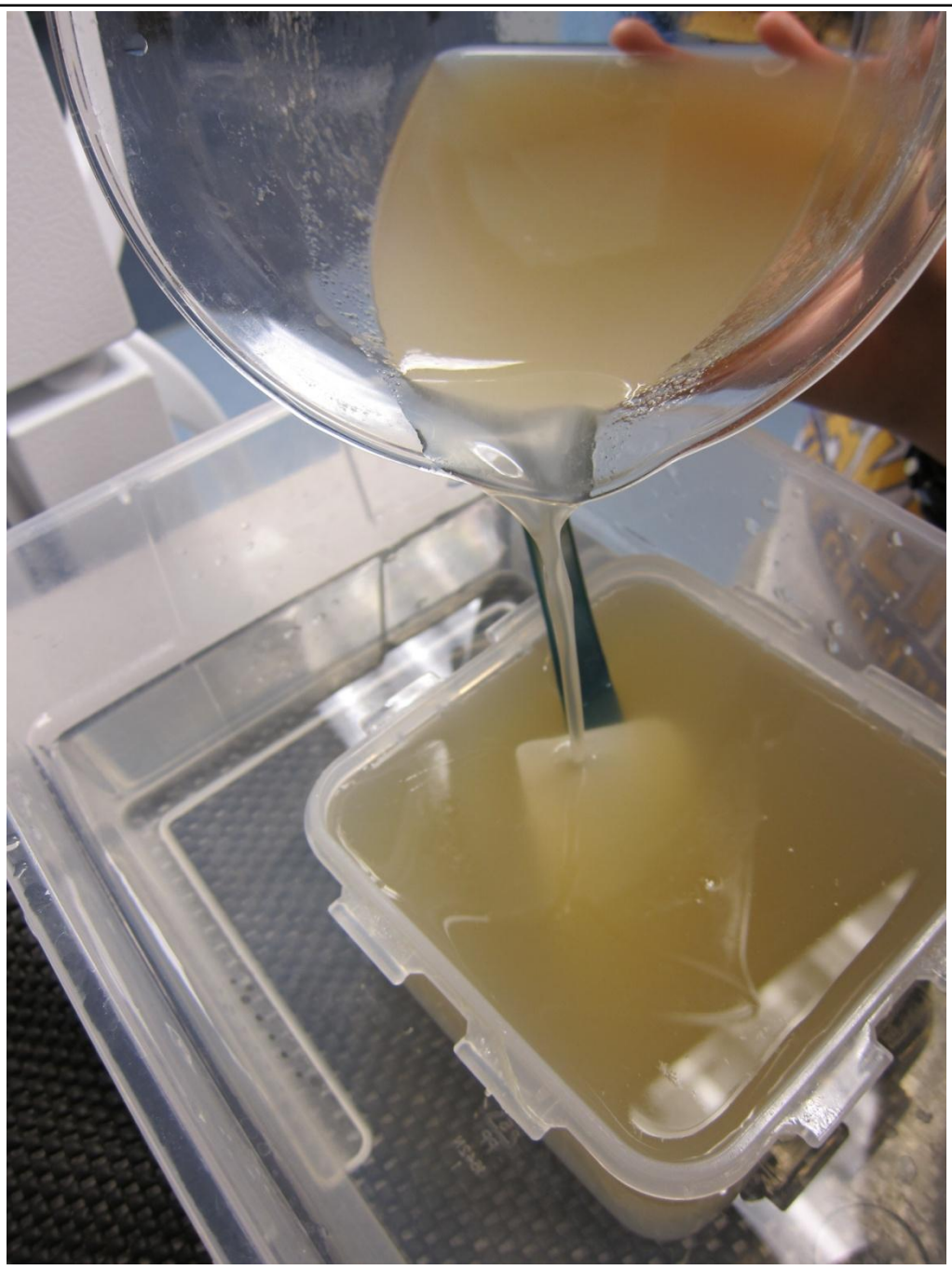

Figure C8. Fill the container until the liquid overflows

h. Put the whole water bath into the refrigerator and wait for at least 6 hours to do the tests; or leave the phantom to congeal in room temperature and wait for at least 12 hours to do the tests (Fig. C9).

Figure C9. Put the whole water bath into the refrigerator.

Appendix D: Matlab Programs

a. Spline-based algorithm for displacement estimation (Viola and Walker, 2005)

spline_tde.m

```
function d = spline_tde(s1,s2,f_samp)
%% Viola, F., Walker, W.F.,
% A spline-based algorithm for continuos time-delay estimation using
% sampled data, IEEE Trans. on Ultras., Ferr., and Freq., Contr., vol. 52,
% no. 1, Jan. 2005
% s1: window signal
% s2: kernel signal
% f_samp: sampling frequency
x = [0:length(s1) - 1];
y = spline(x,s1); % generate cubic spline coefficients
len = length(s1) - length(s2);
for i = 1:len %slide kernel across window
c = y.coefs(i:i+length(s2)-1,:);
[r(i),v(i)] = msse(c,s2);
end
p = find(r>=0&r<1);
[m,j] = min(abs(v(p)));
d = (-round((len+1)/2) + p(j) + r(p(j)))*1/f_samp;
```

msse.m

```
function [x,v] = msse(c,y);
%% Child function of spline_tde.m
%% Viola, F., Walker, W.F.,
% A spline-based algorithm for continuos time-delay estimation using
% sampled data, IEEE Trans. on Ultras., Ferr., and Freq., Contr., vol. 52,
% no. 1, Jan. 2005
[n,m] = size(c);
p = [c(:,1)'*c(:,1) 2*(c(:,1)'*c(:,2)),...
2*(c(:,1)'*c(:,3))+c(:,2)'*c(:,2),...
2*(c(:,1)'*c(:,4))+2*(c(:,2)'*c(:,3))-2*(c(:,1)'*y),...
2*(c(:,2)'*c(:,4))+c(:,3)'*c(:,3)-2*(c(:,2)'*y),...
2*(c(:,3)'*c(:,4))-2*(c(:,3)'*y),...
c(:,4)'*c(:,4)+y'*y-2*(c(:,4)'*y)];
r = roots([6*p(1) 5*p(2) 4*p(3) 3*p(4) 2*p(5) p(6)]);
nr = r(find(imag(r)==0));
for i = 1:length(nr)
for j = 1:7
x_matrix(j,i) = nr(i)^(7-j);
end
end
values = p*x_matrix;
[v,i] = min(values);
x = nr(i); %local delay estimate
```

b. Green's function simulation

green_function_pulsed_time.m

```
%% Simulation for the Green's function, based on Catheline et al., 1999
% Catheline, S., Wu, F. and Fink, M. A., "A solution to diffraction biases
% in sonoelasticity: The acoustic impulse technique", J. Acoust. Soc. Am.
% 105(5), 2941 - 2950, May 1999
% Pengfei Song
% 04/04/2010

%% Start the program
clear all;
close all;

%% Initialize parameters
tt = 0.01:0.01:60; % total simulation time (ms)
rho = 1000; % phantom density (kg/m^3)
mu = 10000; % shear elasticity(Pa)
zs = 8:.5:50; % depth(mm)
Cp = 1500; % compressional wave velocity(mm/ms)
Cs = sqrt(mu/rho); % shear wave velocity(mm/ms)
omega = 150*2*pi/1000; % central frequency of the vibraion (rad/ms)
gamma = Cp/Cs;
tstart = 10; % vibration starting time(ms)
sGzz = zeros(length(zs),length(tt)); % define storing matrix
damp_factor = 5; % Damping factor for the sinusoid input
damp_factor2 = 0.1;

%% Start the loop
for z = 1:length(zs)
ft2 = Cp/(2*pi*mu*(zs(z)/1000)^2*gamma^2); % constant
tp = tstart + zs(z)/Cp; % compressional wave arrival time (ms)
ts = tstart + zs(z)/Cs; % shear wave arrival time (ms)
for t = 1:length(tt)
if(tt(t)<tp)
sGzz(z,t) = 0;
end
if((tp<=tt(t))&&(tt(t)<ts))
sGzz(z,t) = ft2*(omega*tp*cos(omega*(tt(t)-tp))...
*exp(-(tt(t)-tp)/damp_factor2)-2*gamma*cos(omega*(tt(t)-tp))...
*exp(-(tt(t)-tp)/damp_factor2)/(omega*ts));
end
if((tt(t)>=ts))
sGzz(z,t) = ft2*(omega*tp*cos(omega*(tt(t)-tp))...
*exp(-(tt(t)-tp)/damp_factor)-2*gamma*sin(omega*(tt(t)-ts))...
*exp(-(tt(t)-ts)/damp_factor)+2*gamma*(cos(omega*(tt(t)-ts))...
*exp(-(tt(t)-ts)/damp_factor)-cos(omega*(tt(t)-tp))...
*exp(-(tt(t)-tp)/damp_factor))/(omega*ts));
end
end
end

%% Visulize the results
axes('FontSize',16);
mesh(tt,zs,-sGzz,'MeshStyle','row');
xlabel('Time (ms)','FontSize',16);
ylabel('Depth (mm)','FontSize',16);
zlabel('Amplitude (mm)','FontSize',16);

seismic_plot(tt,zs,-sGzz);
```

c. Main program of data processing

disp_tde.m

```
%% Main program of ultrasound transient elastography.
% Pengfei Song
% 03/01/2010

%% Load data
clear all;
clc;
load('test1.dat');
MmodeArray = test1;
clear test1;

%% Initialize parameters
f_digitizer = 100e6; %digitizer sampling frequency (Hz)
prf = 1500; %PRF (Hz)
interp_factor = 5; %Interpolation factor
rec_length = size(MmodeArray,1); %number of samples in depth direction
speed = 1540; %sound speed in phantom (m/s)
f_samp = round(1e-3*2/speed*f_digitizer);%sampling frequency
   (samples/mm)
ksize = f_samp;%kernel size(axial)
xstart = 1;%time diretion start index
ystart = 1;%depth direction start index
yend = ksize;
overlap = 0.5; %overlapping coefficient
stepsize = round(ksize - ksize*overlap);%number of steps
nkernel = round((size(MmodeArray,1)-2*ksize)/stepsize);%number of
   kernels

%% Interpolate the original image in time direction
for i = 1:size(MmodeArray,1)
MmodeArray1(i,:) = interp(MmodeArray(i,:),interp_factor);
end
clear MmodeArray;
display('Interpolation completed');

%% Filter the data in depth direction
[num den] = butter(5,[1 6]/100);
for i = 1:size(MmodeArray1,2)
MmodeArray2(:,i) = filter(num,den,MmodeArray1(:,i));
end
clear MmodeArray1;
MmodeArray = [];
MmodeArray = MmodeArray2;
clear MmodeArray2;
xend = size(MmodeArray,2);
scan = xend-xstart+1;
displacement = zeros(nkernel,scan);

%% Displacement calculation
display('start');
for n = 1:nkernel
ystart = (n+1)*stepsize;
ystartfix = ystart;
yend = ystart+ksize-1;
for i = 1:scan-1
ref = MmodeArray(ystart:yend,xstart+i-1);
window = MmodeArray(ystart-10:yend+10,xstart+i);
```

```
d = spline_tde(double(window),double(ref),f_samp);
if(isempty(d))
if(i==1)
d = 0;
else
d = displacement(n,i-1);
end
end
displacement(n,i) = d;
end
percentdone = n/nkernel
end

%% Filter the displacement data
fs = prf*interp_factor; %actual sampling frequency after interpolation
displacement_filtered = disp_filter(displacement,fs);

%% Visulize the displacement field
end_depth = 67; % surface depth
start_depth = end_depth - size(displacement_filtered,1)*overlap;
seismic_plot((1:size(displacement_filtered,2))/fs*1000,start_depth:ove
rlap:end_depth);
```

d. Displacement data filtering

disp_filter.m

```
1.  % Filter the displacement data
2.  % Pengfei Song
3.  % 04/12/2010

4.  function filtered_disp = disp_filter(data,t_samp)

5.  % input the displacement field results and the time sampling frequency
6.  % (PRF*interpolation factor)

7.  [m n] = size(data);
8.  NFFT = 2^nextpow2(n);
9.  Y = fft(data(1,:),NFFT)/n;
10. f = t_samp/2*linspace(0,1,NFFT/2);
11. figure
12. plot(f,2*abs(Y(1:NFFT/2)));
13. title('Amplitude Spectrum');
14. xlabel('Frequency (Hz)');
15. ylabel('Amplitude');

16. cutoff = input('Cutoff frequency for low pass filter:');

17. [nom dim] = butter(5,cutoff/(t_samp/2),'low');
18. filtered_disp = zeros(m,n);
19. for i = 1:m
20. filtered_disp(i,:) = filter(nom,dim,data(i,:));
21. end

22. seismic_plot(1:size(data,2),1:size(data,1),filtered_disp);
```

e. Seismic plot

seismic_plot.m

```
1.  %% Seismic plot of the displacement field
2.  % Pengfei Song
3.  % 04/05/2010

4.  %% Function
5.  function seismic_plot(t,depth,data)
6.  figure
7.  axes('FontSize',16);
8.  hold on;
9.  for i = 1:length(depth)
10. data(i,:) = data(i,:)*3000 + depth(i);
11. plot(t,data(i,:),'LineWidth',2);
12. end
13. xlabel('Time (ms)','FontSize',16);
14. ylabel('Depth (mm)','FontSize',16);
15. hold off
16. end
```

f. Phase gradient and shear-wave velocity calculation

phase_depth_plot.m

```
1.  %% This is the code to plot the phase - depth result and do linear fitting
2.  % on each selected part

3.  % Pengfei Song
4.  % 05/18/2010

5.  %% load data
6.  clear all;
7.  close all;
8.  load right10.mat;
9.  data = displacement_filtered;
10. seismic_plot(1:1000,1:119,data);

11. %% plot the phase map
12. hdf = hilbert(data');
13. hdf = hdf.';
14. figure
15. imagesc(angle(hdf));

16. %% select the time point to plot the phase
17. time = input('Input the time point:');
18. startdepth = input('start depth:');
19. enddepth = input('end depth:');
20. overlap = 0.5;
21. depth = startdepth:overlap:enddepth;
22. pha = unwrap(angle(hdf(:,time)));
23. plot(depth,pha);

24. %% select region of interests and do linear fitting
25. start1 = input('start1:');
26. end1 = input('end1:');

27. start2 = input('start2:');
28. end2 = input('end2:');

29. % plot the results
30. figure
31. hold on;
32. axes('FontSize',16);
33. plot(start1:overlap:end1,pha((find(depth==start1)):(find(depth==end1)
    )),'bo','LineWidth',2);
34. fit1 =
    polyfit(start1:overlap:end1,pha((find(depth==start1)):(find(depth==en
    d1)))',1);
35. plot(start1-1:overlap:end1+1,fit1(1)*(start1-1:overlap:end1+1)+fit1(2
    ),'b','LineWidth',2);

36. plot(start2:overlap:end2,pha((find(depth==start2)):(find(depth==end2)
    )),'ro','LineWidth',2);
37. fit2 =
    polyfit(start2:overlap:end2,pha((find(depth==start2)):(find(depth==en
    d2)))',1);
38. plot(start2-1:overlap:end2+1,fit2(1)*(start2-1:overlap:end2+1)+fit2(2
    ),'r','LineWidth',2);

39. plot(end2+0.5:overlap:enddepth,pha((find(depth==end2+0.5):(find(depth
    ==enddepth)))),'ko','LineWidth',2);
```

```
grid on;
xlabel('Depth (mm)','FontSize',16);
ylabel('Phase (rad)','FontSize',16);
hold off;

%% Calculate the shear-wave speed and corresponding Young's Modulus
rho = 1040; % phantom density (kg/m^3)
speed = 1/fit1(1)*2*pi*50/1000; % shear-wave speed (m/s)
e = speed^2*rho*3; % Young's modulus (Pa)
```

g. Create a speed image

speed_image.m

```
%% Convert the shear-wave velocity/tissue elasticity to RGB color and create
% a speed image

% Pengfei Song
% 05/10/2010

%% Load data
clear all;
load phase_bt_0510.mat;

%% Create a RGB matrix
RGB=reshape(ones(256,1)*reshape(jet(256),1,768),[256,256,3]);
newcolor = [];
step = 15; %step size of calculating (averaging) the phase velocity
gray_index = [];

%% Convert speed to color
for j = 1:size(pha,2)
phase_velocity = [];
temp = pha(:,j);
dstart = size(temp,1);
dend = step+1;
for k = dstart:-1:dend
fit_data = polyfit(k-step:k,temp(k-step:k)',1); % Linear fitting
phase_velocity(dstart-k+1) = (fit_data(1)*2)^(-1)*2*pi*50;% for 50% overlap
end
temp1 = phase_velocity/max(phase_velocity);
index = round(abs(256*ones(size(phase_velocity,1),1).*temp1));
gray_index(:,j) = phase_velocity/1000;
for i = 1:length(index)
if(index(i)==0)
index(i)=1;
end
if(index(i)>256)
index(i)=256;
end
newcolor(i,j,1) = RGB(1,index(i),1);
newcolor(i,j,2) = RGB(1,index(i),2);
newcolor(i,j,3) = RGB(1,index(i),3);
end
index = [];
end

figure
imagesc(newcolor);
figure
imagesc(gray_index);
figure
imagesc(scale_color);
anew = [];
bnew = [];

%% Interpolation
for i = 1:size(newcolor,3)
for j = 1:size(newcolor,1)
```

```
50. anew(j,:,i) = interp(newcolor(j,:,i),10);
51. end
52. end

53. for i = 1:size(newcolor,3)
54. for j = 1:size(anew,2)
55. bnew(:,j,i) = interp(anew(:,j,i),5);
56. end
57. end
```

h. Create an elasticity image

elasticity_map.m

```
%% Calculate the shear wave velocity at each depth layer using
% time-of-flight algorithm (Muller et al., 2009), and convert the
velocities/elasticity to
% RGB color and map onto the B-mode image if existed.

% Pengfei Song
% 05/10/2010

% P. Song, revision
% 05/28/2010

%% Load the data
clear all;
load phase_bt_0510.mat;

%% Define a color matrix
RGB=reshape(ones(256,1)*reshape(jet(256),1,768),[256,256,3]); % 256
color gradation
ndistant = 5; % the number of distance pairs that

%% Start the program
newcolor = [];
gray_index = [];
for j = 1:size(pha,2)
phase_velocity = [];
temp = pha(:,j);
dstart = size(temp,1);
dend = 1;
for k = dstart:-1:dend
vtemp = 0;
for r = 1:ndistant
if (k+r>dstart)
dtemp = temp(k-r:dstart);
fit_data = polyfit(k-r:dstart,dtemp',1);
if(vtemp<0||vtemp>200000)
vtemp = 200000;
end
vtemp = vtemp + (1/ndistant)*((fit_data(1)*2)^(-1)*2*pi*50);
end
if(k-r<dend)
dtemp = temp(dend:k+r);
fit_data = polyfit(dend:k+r,dtemp',1);
vtemp = vtemp + (1/ndistant)*((fit_data(1)*2)^(-1)*2*pi*50);
if(vtemp<0||vtemp>200000)
vtemp = 200000;
end
end
if (k+r<=dstart&&k-r>=dend)
dtemp = temp(k-r:k+r);
fit_data = polyfit(k-r:k+r,dtemp',1);
vtemp = vtemp + (1/ndistant)*((fit_data(1)*2)^(-1)*2*pi*50);
if(vtemp<0||vtemp>200000)
vtemp = 200000;
end
end
end
phase_velocity(dstart-k+1) = vtemp;% for 50% overlap
```

```
51. end
52. temp1 = phase_velocity/max(phase_velocity);
53. index = round(abs(256*ones(size(phase_velocity,1),1).*temp1));
54. gray_index(:,j) = phase_velocity/1000;
55. scale_color(:,j) = index;
56. for i = 1:length(index)
57. if(index(i)==0)
58. index(i)=1;
59. end
60. if(index(i)>256)
61. index(i)=256;
62. end
63. newcolor(i,j,1) = RGB(1,index(i),1);
64. newcolor(i,j,2) = RGB(1,index(i),2);
65. newcolor(i,j,3) = RGB(1,index(i),3);
66. end
67. index = [];
68. end

69. anew = [];
70. bnew = [];
71. % interpolation
72. newcolor = newcolor(1:88,:,:);
73. for i = 1:size(newcolor,3)
74. for j = 1:size(newcolor,1)
75. anew(j,:,i) = interp(newcolor(j,:,i),34);
76. end
77. end
78.
79. for i = 1:size(newcolor,3)
80. for j = 1:size(anew,2)
81. bnew(:,j,i) = interp(anew(:,j,i),26);
82. end
83. end
84. figure
85. imshow(bnew);
```

Appendix E: LabVIEW ProbeForFlowScopeCounter.m.vi Block Diagram

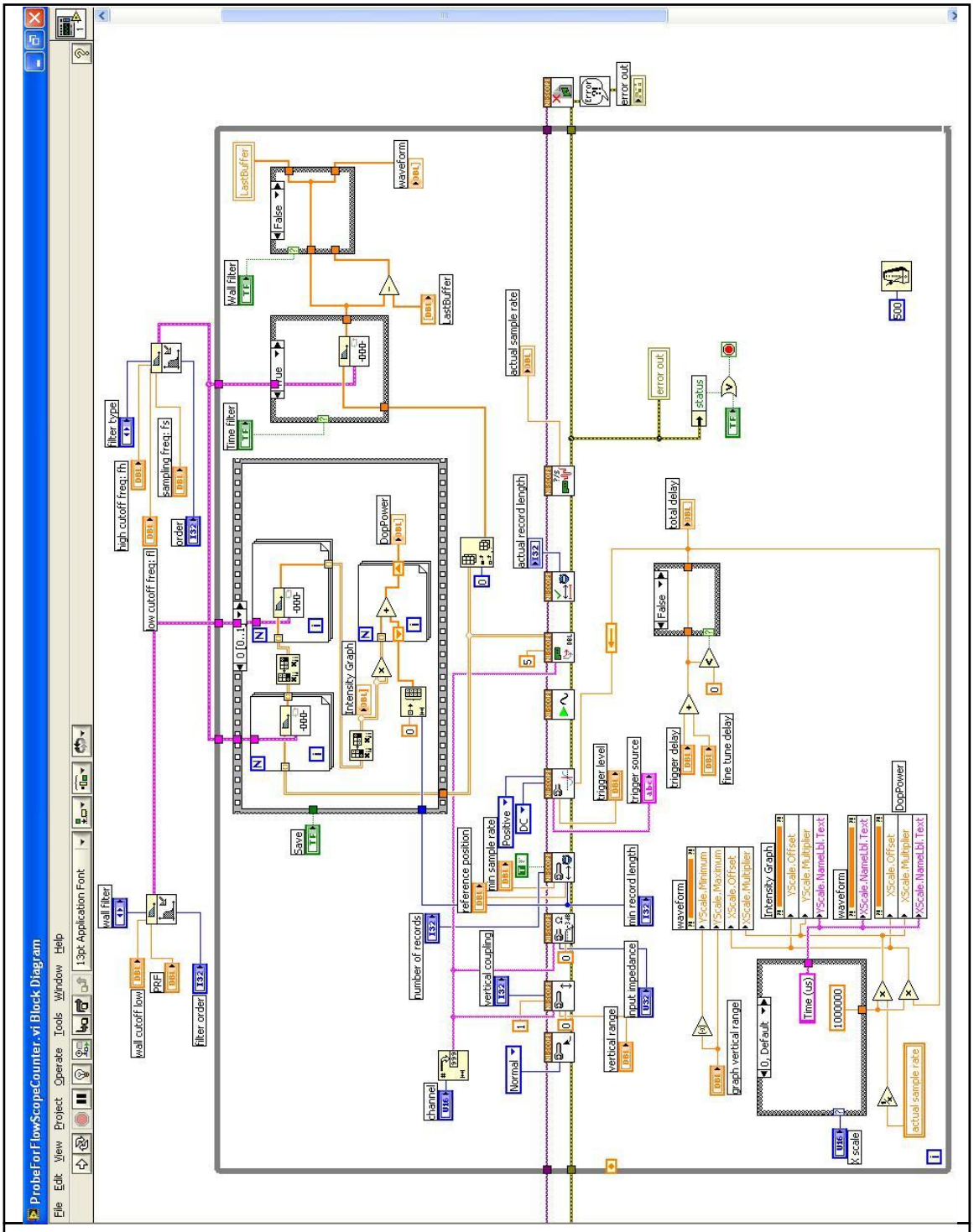

Figure E1. Block diagram of ProbeForFlowScopeCounter.m.vi (Part 1)

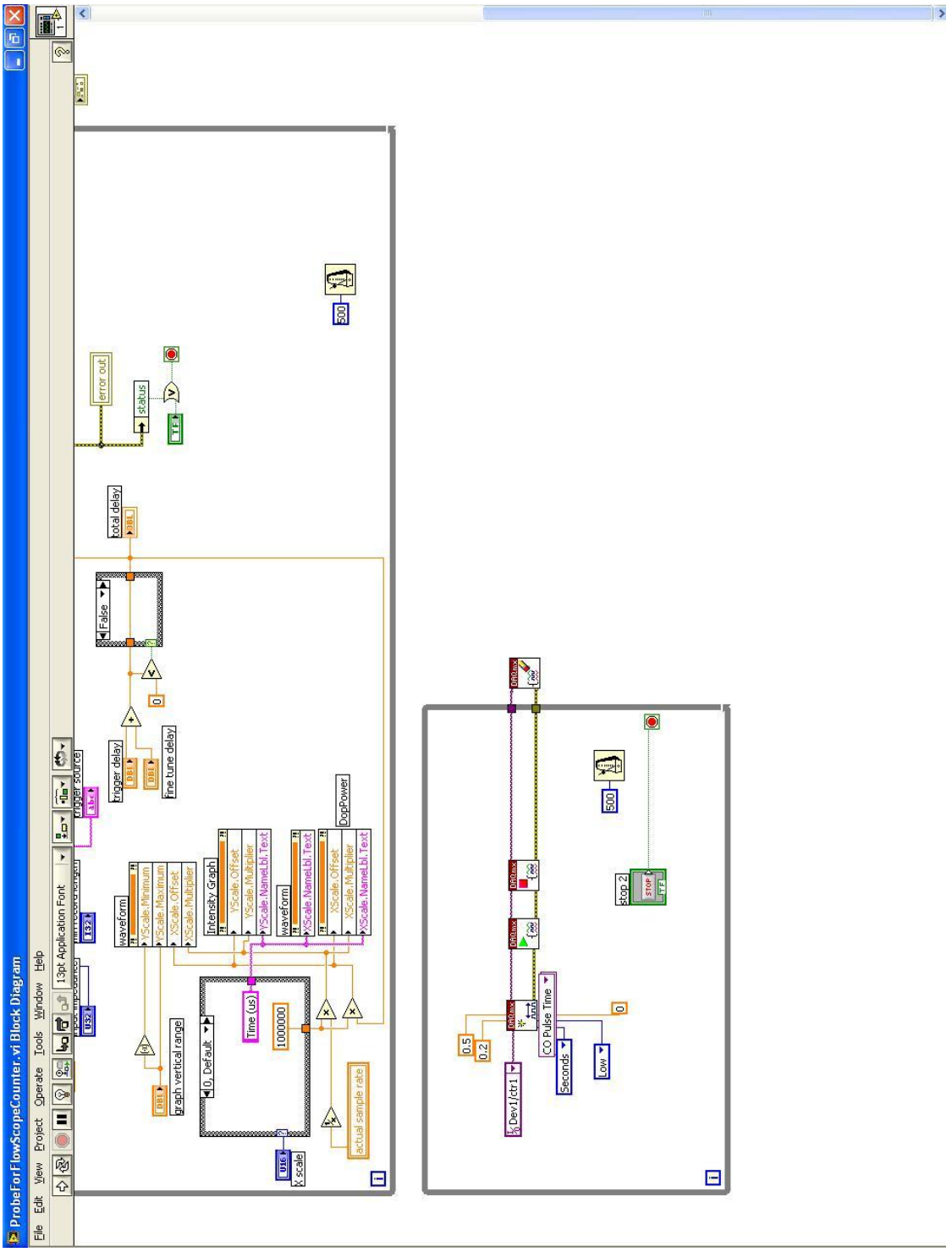

Figure E2. Block diagram of ProbeForFlowScopeCounter.m.vi (Part 2)